

Magnetic jets from accretion disks: field structure and X-ray emission

Dissertation zur Erlangung des akademischen Grades
Doktor der Naturwissenschaften (Dr. rer. nat.)
in der Wissenschaftsdisziplin Astrophysik

eingereicht an der
Mathematisch–Naturwissenschaftlichen Fakultät
der Universität Potsdam

von
Elisabetta Memola

Potsdam, im März 2002

*“There is something fascinating about science.
One gets such wholesale returns of conjecture
out of such a trifling investment of fact.”*

Mark Twain, Life on the Mississippi, Boston 1883

Contents

Introduction	3
1 Astrophysical jets	5
1.1 Observational evidence	5
1.1.1 Young Stellar Objects	5
1.1.2 Microquasars	6
1.1.3 Active Galactic Nuclei	8
1.1.4 The example of M87	9
1.1.5 Gamma-Ray Bursts	10
1.2 The standard model - A magnetic jet	13
1.3 The matter content of jets	13
2 Two-dimensional magnetic field structure of relativistic jets: setup of the theoretical problem	17
2.1 Magnetic jets	17
2.2 Assumptions	19
2.3 Basics of MHD	20
2.4 The Grad-Shafranov equation	21
2.4.1 Regularity condition along the light surface	24
2.4.2 Discussion of the force-free assumption	25
2.5 Boundary conditions	26
2.5.1 The asymptotic jet	26
2.5.2 The disk	27

2.5.3	The collimating jet boundary	27
2.5.4	Inner boundary conditions	28
2.6	The jet-disk connection	28
3	Numerical results	33
3.1	The collimation region	33
3.2	Determination of the light surface	34
3.3	Examples of a non-regular magnetic flux distribution	35
3.4	Global regular solutions in two dimensions	36
3.5	Scaling of the jet-disk system	40
3.6	Magnetic angular momentum loss and disk toroidal field	45
3.7	Comparison with observations	48
4	X-ray emission of MHD jets from stellar mass black holes	51
4.1	The model	51
4.2	The MHD wind solution from a rotating black hole	53
4.3	Thermal emission	55
5	Theoretical thermal X-ray spectra	59
5.1	The rest frame spectrum	59
5.2	The Doppler shifted and Doppler boosted spectra	60
5.3	Total Doppler shifted and boosted spectra	63
5.4	Comparison with observations	66
	Summary	70
	Appendix	74
A.1	Numerical details	75
	Bibliography	78
	Acknowledgment	85

Introduction

Jets are ubiquitous in the universe. They are highly collimated flows of gas and energy produced by a large variety of astrophysical objects. These include young stars, stellar mass black holes, Active Galactic Nuclei and presumably also Gamma Ray Bursts.

Despite the large differences in the sizes of these jets, the physics of the propagation of jet flows and the radiative mechanisms at work in them are similar in many cases. In particular, jets powered by accretion disks in binary stars with a black hole component (microquasars) are probably small-scale versions of the outflows from AGN.

Relativistic jets with bulk Lorentz factors ranging from ~ 2 to ~ 20 are observed close to some AGN (Begelman, Blandford & Rees 1984). The explanation for the knots seen in the jets of microquasars and AGN are shock fronts travelling along the gas flow constituting the jet. These shocks accelerate electrons to very high random velocities. Their relativistic Lorentz factors can reach several 10^5 which implies velocities in excess of 0.9999999995 times the speed of light! As these electrons emit synchrotron radiation which we observe, there are also magnetic fields in jets. How these fast-moving jets are produced remains an open question.

Although various mechanisms have been proposed to explain jets acceleration and collimation, since the famous work of Blandford & Payne (1982) an electromagnetic origin of jets seems to be favoured.

In general, due to the complexity of the magnetohydrodynamic equations describing the field structure and the flow dynamics along the field, stationary relativistic models of magnetic jets have to rely on simplifying assumptions such as self-similarity (Contopoulos 1994, 1995), some other prescription of the field structure (Li 1993) or the restriction to asymptotic regimes (Chiueh, Li & Begelman 1991; Appl & Camenzind 1993b; Nitta 1994, 1995). For highly magnetized jets the force-free limit may be applied. This allows for a truly two-dimensional calculation of the magnetic field structure (Fendt, Camenzind & Appl 1995; Fendt 1997a).

Taking into account the observational evidence of a connection between disks, jets and magnetic fields, the purposes of this work were:

- The numerical calculation of the global two-dimensional structure of the jet mag-

netosphere, including *differential rotation* of the foot points of the field lines (Fendt & Memola 2001a; Memola & Fendt 2001).

- The investigation of the inner jet X-ray emission as a tracer of the jet dynamics (Fendt & Memola 2001b; Memola, Fendt & Brinkmann 2002).

This thesis is organized in 5 chapters with a final part dedicated to summary and discussion of the newly obtained results.

Chapter 1: a brief overview about astrophysical objects with jets is presented and the examples of M87 and HH212 are illustrated. A short introduction to the standard model of a magnetic jet-disk system is given.

Chapter 2: the problem of the magnetic field structure calculation is described. It implies the solution of the special relativistic Grad-Shafranov equation.

Chapter 3: numerical results showing the global two-dimensional jet field distribution are presented and discussed, with particular application to the active galaxy M87.

Chapter 4: a solution of the magnetic wind equation along a given field line is used to obtain X-ray luminosities of jet-tori at different temperatures.

Chapter 5: the total spectra of the inner jet are presented for different inclinations of the line-of-sight to the jet-axis. Doppler shifting and boosting of each volume element along the jet have been taken into account. Results are compared with observational data of the microquasars GRS 1915+105 and XTE J1748–288.

Summary: outline and discussion.

Appendix: details about the Finite Element Code (Camenzind 1987; Fendt, Camenzind & Appl 1995; Fendt & Memola 2001a; Memola & Fendt 2001) used for the solution of the Grad-Shafranov equation are clarified.

Chapter 1

Astrophysical jets

1.1 Observational evidence

Highly collimated and axisymmetric jets are observed in Young Stellar Objects (YSOs), in high energy galactic sources (microquasars) and Active Galactic Nuclei (AGN). Some observational evidence suggests also the presence of jets in Gamma-Ray Bursts (GRBs).

Collimated jets seem to be systematically associated with the presence of an accretion disk around a star or a collapsed object. In all known type of jet sources a disk is believed to be present (Mirabel & Rodríguez 1999). On the other hand, there exist disk systems without jets, like in the case of Cataclysmic Variables (CV) binary systems, but the reason for this physical difference is not yet known.

It has been argued that when relativistic motion of the jet material is observed, the jet must be strongly magnetized (Michel 1969; Fendt & Camenzind 1996). To produce superluminal motion there are two requirements: (i) the blobs must be moving with velocities approaching the speed of light ($u \sim c$), (ii) the blob trajectory must be inclined at a small angle to the line-of-sight.

Jets are radio, infrared, optical, X-ray and γ -ray emitters (e.g. Sikora et al. 1997). In particular, the strongly polarized optical and radio synchrotron radiation (e.g. Burbidge 1956) is the signature of the presence of magnetic fields.

1.1.1 Young Stellar Objects

Observations show that young stellar objects (YSOs) may consist of three main components: a protostar (e.g. a TTauri star) a circumstellar accretion disk and highly col-

limited jets (sometimes being related to Herbig Haro (HH) objects) that can extend from 100 AU till 10^6 AU away from the young star (Biretta 1999) with velocities about 400 km/sec (e.g. Mundt et al. 1990).

The accretion disk channels the gas and dust of a collapsing cloud onto the central protostellar object. The outflowing gas is thought to be collimated and accelerated by magnetic fields, but direct observational evidence for such fields has so far been lacking. The young star dipolar field strength may be of the order of some or several kiloGauss (André et al. 1991; Ray et al. 1997).

Jets can in principle be used to study the accretion and ejection history of the system, hidden from direct view by the dust and dense gas of the parent cloud. On the other hand, jets have often structures too complex to determine which features arise at the source and which are the result of later interactions with the surrounding gas. An example of a protostellar jet is shown in Fig. 1.1 (Zinnecker, McCaughrean & Rayner 1998). The jet is driven by an invisible protostar, at a distance of 400 pc, in the vicinity of the Horsehead nebula in Orion. Fig. 1.1 is a high-resolution near-infrared image of the central knots and bowshocks in HH212, extending for $\sim 3.3 \times 10^4$ AU. HH212 covers a total length of $\sim 10^5$ AU. These observations show a remarkable bipolar symmetry centred on the driving source, and, in particular, a sequence of knotty shock structures occurring at quasi-regular intervals and with near-perfect mirror symmetry either side of the source.

1.1.2 Microquasars

Microquasars (Mirabel & Rodríguez 1999) are X-ray binaries with relativistic jets in our Galaxy. They mimic, on a much smaller scale, many of the phenomena seen in quasars. In these binaries of stellar mass the three basic features of quasars are found: a black hole, an accretion disk and collimated jets. In microquasars (see Fig. 1.2) a black hole of a few solar masses is present instead of a several million solar masses one as in quasars; the disk has mean thermal temperatures of several million degrees instead of several thousands; the matter ejected at relativistic speed can reach distances of a few light years against several million of years as in the case of giant radio galaxies (Mirabel & Rodríguez 1998). Five microquasars (at the moment, but the number is increasing!) are for sure superluminal sources: 1) GRS 1915+105, with a black hole mass of $14 \pm 4 M_{\odot}$ (Greiner, Cuby & McCaughrean 2001) at a distance of 7–12 kpc from the Sun (Fender et al. 1999), 2) GRO J1655–40, with a black hole mass around $7 M_{\odot}$, at a distance of 3.2 kpc (Greiner 2000), 3) XTE J1748–288, with a constraint for the mass of the black hole of $M_{\text{BH}} > 4.5 M_{\odot}$ at a distance $D > 8$ Kpc (Miller et al. 2001), 4) SAX J1819.3–2525 (V4641 Sgr) with a black hole mass around $8.73\text{--}11.70 M_{\odot}$ (90% confidence) at a distance of 7.40–12.31 kpc (90% confidence, Orosz et al. 2001), 5) XTE J1550–564 that is believed to harbor a black hole, but a mass function has still to be measured, at a distance of 2.5 kpc (Corbel et al. 2001). In all cases the intrinsic velocity of the jet components is higher than $0.9 c$. The jet magnetic field strength is not known.

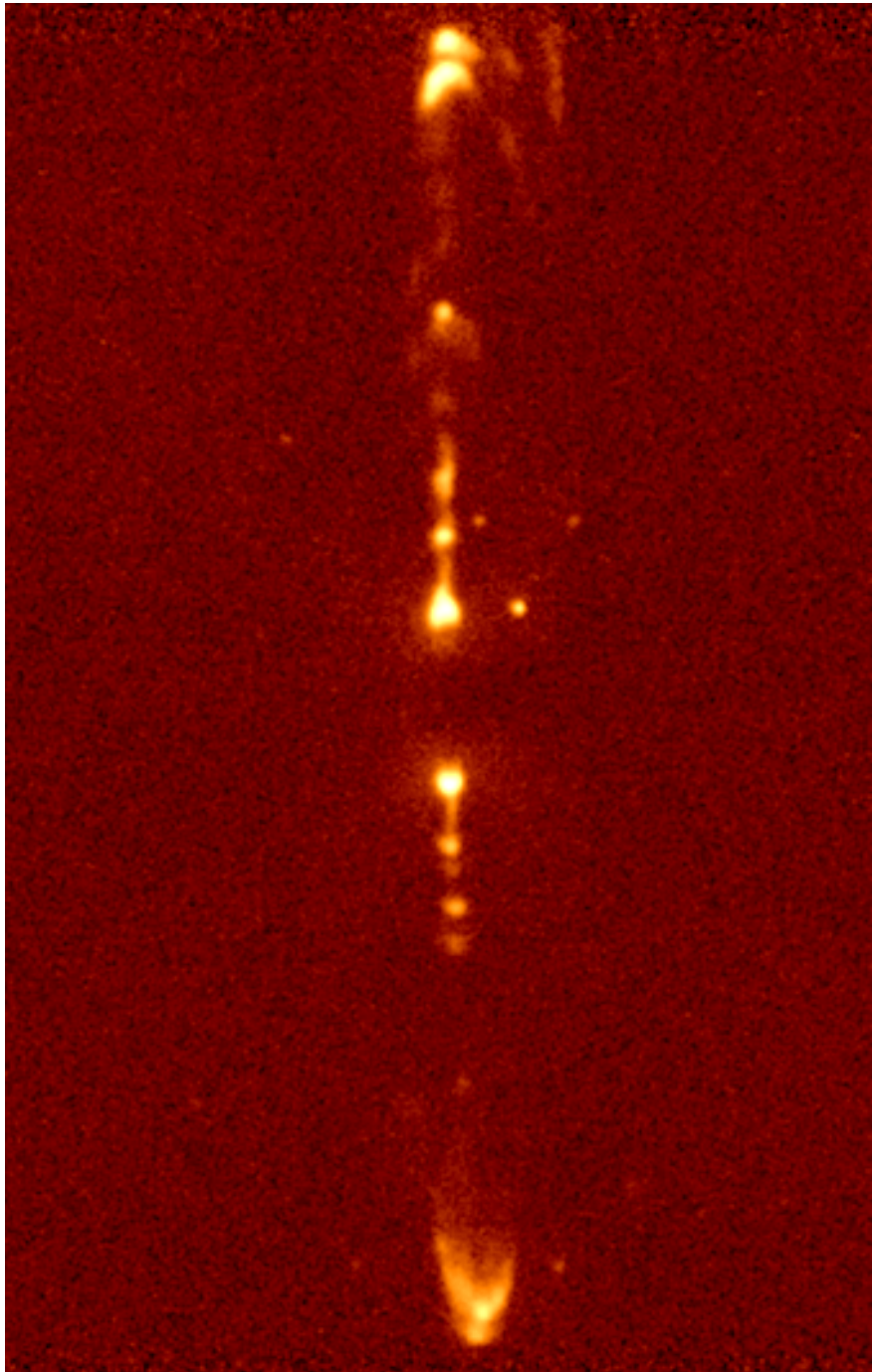


Figure 1.1: High-resolution near-infrared image of the central knots and bowshocks in HH212 (Zinnecker, McCaughrean & Rayner 1998).

Till the recent discovery of jets from other microquasars, Stephenson-Sanduleak 433 (SS433) was the only known example of a mildly relativistic jet in our Galaxy. SS433 is a binary system in the SNR W50, where a neutron star accretes matter from its companion, forming an accretion disk. The detection of large, periodic Doppler shifts in the optical lines of SS433 (Margon et al. 1979), resulted in the proposition of a

kinematic model (Fabian & Rees 1979; Milgrom 1979), consisting of two jets of $0.26 c$ precessing because of tidal forces.

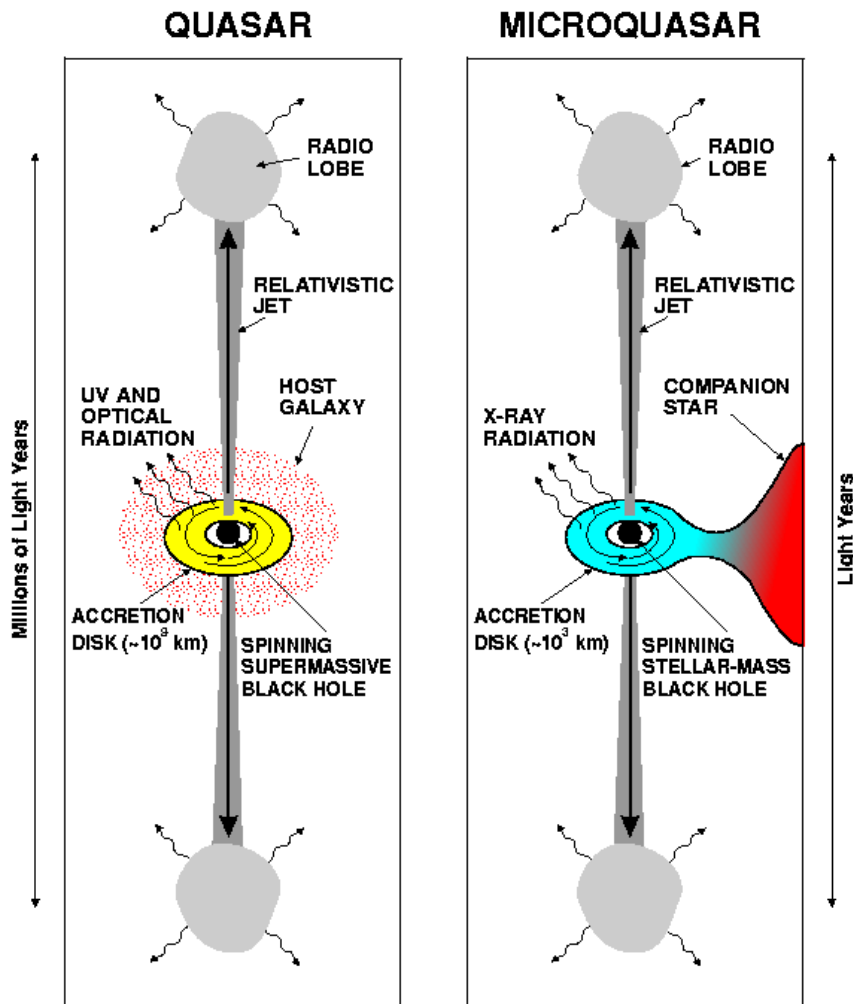


Figure 1.2: Diagram illustrating current ideas about quasars and microquasars (not to scale) by Mirabel and Rodríguez (1998).

1.1.3 Active Galactic Nuclei

The activity in radio quiet and radio loud AGN (Urry & Padovani 1995) is most probably powered by accretion onto a supermassive black hole.

In radio-quiet AGN jets are slow and highly dissipative. In radio-loud AGN jets are highly collimated and relativistic. The plasma jet streams outward, on scale of parsec, at relativistic speed, while on scale of hundreds kiloparsec or even Megaparsec it might be that the jet velocity is a small fraction of the speed of light. Radio jets are in fact detected on scales from 10^{17} cm to several times 10^{24} cm distance from the host galaxy, a factor of 10 larger than the largest galaxies. These jets penetrate their host galaxies and

extend into the intergalactic medium where they end up in bright hot spots. The orientation of the observer respect to the jet is a determining factor in the observed properties of those AGN, but there is a strong tendency in considering these classes as fundamentally identical. At the center is a supermassive black hole ($M_{\text{BH}} \simeq 10^{7-9} M_{\odot}$) whose gravitational potential energy is the ultimate source of the AGN luminosity (varying, from radio waves to gamma-rays, from 10^{41} to 10^{48} erg/sec). Matter pulled towards the black hole loses angular momentum through viscous or turbulent processes in an accretion disk, which glows brightly at ultraviolet and perhaps soft X-ray wavelengths. Hard X-ray emission is also produced very near the black hole, perhaps in connection with a pervasive sea of hot electrons above the disk.

Giving the fact that radio emission from jets is nonthermal and polarized, the phenomenological model assumed is the optically-thin synchrotron source. In the limit of minimum energy requirement corresponding to equipartition between relativistic electrons (and protons) and magnetic field, the field strength in AGN jets on scales $2-10^3$ kpc is of the order of milliGauss (Ferrari et al. 1996). The accretion disk around a supermassive black hole creates a strong magnetosphere with typical field strenghts of the order of a few kiloGauss at the surface of the disk (Camenzind 1990).

1.1.4 The example of M87

The first evidence of jet-like feature emanating from the nuclei of galaxies goes back to the optical jet of the giant elliptical galaxy M87, at a distance from earth of 14.7 Mpc (Junor, Biretta & Livio 1999), in the Virgo cluster. M87 was discovered by the French astronomer Charles Messier in 1781. Its jet was discovered by Heber Curtis in 1918 as “a curious straight ray ... apparently connected with the nucleus by a thin line of matter”, but it remained an astronomical curiosity until the begin of seventies, when radio-jets started to be revealed in a great number of radio-galaxies.

In Fig. 1.3, as a background, is an image of the large scale radio halo taken by the Very Large Array (VLA) at 327 MHz (90 cm) from Owen, Eilek & Kassim (2000). The radio emitting “bubbles” of hot gas are believed to be powered by the black hole at the galaxy center. The full extent of the radio source is about 80 kpc end to end. The inner lobes and the jet can be seen as the red structure in the center and the black hole is located in the center of this inner structure. As detected by the satellites EINSTEIN and ROSAT, M87 and its radio halo sit in a large atmosphere of hot, X-ray loud gas. In the VLA image taken at 20 cm from Owen (see Fig. 1.3) the inner radio lobes are visible. They extend about 5 kpc end to end. There is no visible sign of a counter-jet, but the apparent flows seen in the halo suggest that it exists but is very faint. In the VLA 2 cm image, taken from Biretta & Owen (see Fig. 1.3), the scale from the bright core to the outermost bright spot is about 2 kpc. The 7 mm VLA image from Owen & Biretta (see Fig. 1.3) is a flow-up of the core. In the Very Large Baseline Interferometry (VLBI) image at 18 cm from Biretta & Junor (see Fig. 1.3) the length of the visible jet is about 17 pc, while in the VLBI image at 1.3 cm from Biretta & Junor (see Fig. 1.3), the length of the visible jet is about 2.5 pc. The innermost jet features have a size of

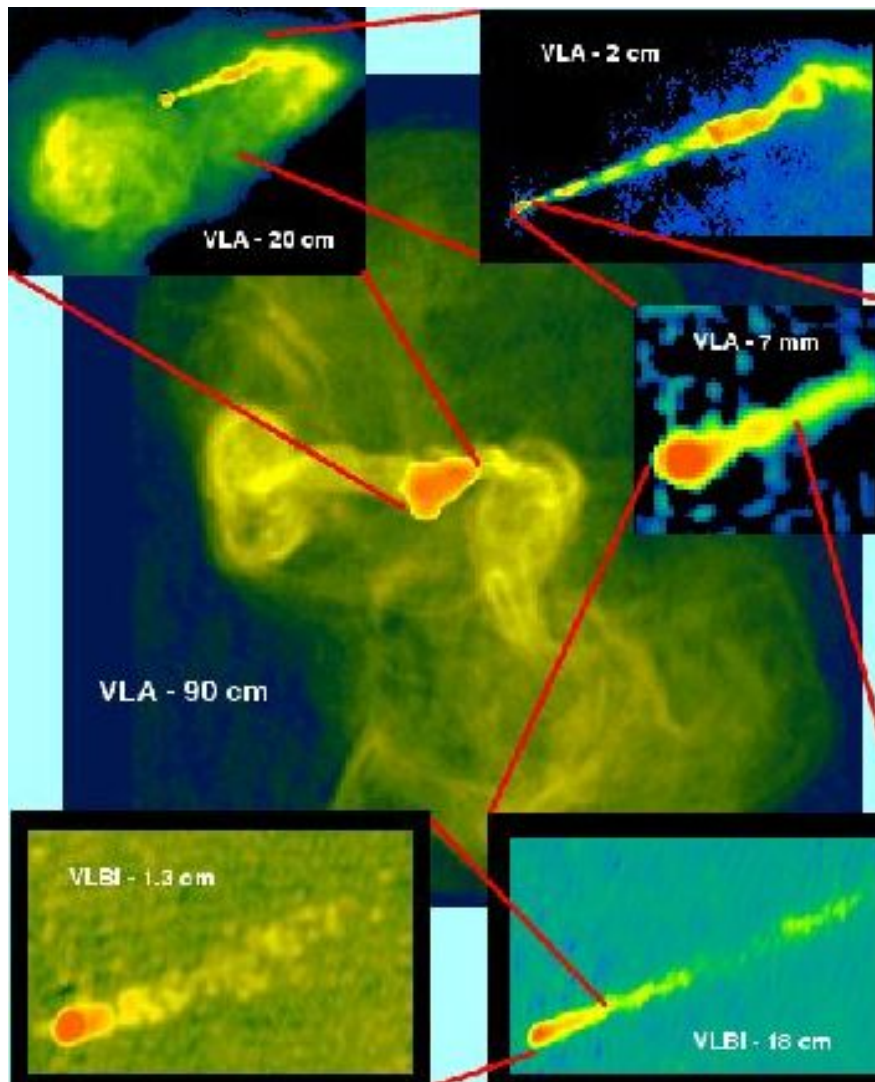


Figure 1.3: M87 – From 200,000 Light Years to 0.2 Light Year. Credit: F. Owen (National Radio Astronomy Observatory), J. Biretta (Space Telescope Science Institute) and colleagues (<http://antwrp.gsfc.nasa.gov/apod/ap990216.html>).

about 0.1 pc, about 100 times the size of the supermassive black hole ($M_{\text{BH}} = 10^9 M_{\odot}$) which drives the system.

1.1.5 Gamma-Ray Bursts

GRBs are sudden, intense flashes of gamma-rays which, for a few blinding seconds, light up in an otherwise fairly dark gamma-ray sky (Mészáros 2001). A major advance occurred in 1991 with the all-sky survey of the Burst and Transient Experiment (BATSE) onboard the Compton Gamma-Ray Observatory (CGRO) measuring about 3000 bursts. The duration range (at MeV energies) was from 10^{-3} sec to about 10^3 sec, with a more or less bimodal distribution of *long* bursts ($t_{\text{burst}} \geq 2$ sec) and *short* bursts

($t_{burst} \leq 2$ sec). Fast progresses have been made in the last five years, in fact, the Italian-Dutch Beppo-SAX satellite, launched in 1996, succeeded in obtaining high resolution X-ray images of GRB events and discovering the X-ray afterglow phenomenon with the burst GRB 970228 (Costa et al. 1997), followed by other GRB detections approximately at the rate of 10 per year. The measurement and localization of fading X-ray afterglows from some GRBs, lasting typically for days, made possible the optical and radio detection of afterglows, that mark the location of the brief GRB event. These afterglows, in turn, allowed the measurement of redshift distances, the identification of host galaxies and the confirmation that GRBs were at cosmological distances of the order of billions of light-years, like the most distant galaxies.

Even at those distances they appear so bright that their energy output has to be of the order 10^{51} – 10^{54} erg/sec, and from causality this must arise in a region of size of the order of kilometers in a time scale of the order of seconds. This implies that an e^\pm , γ fireball must form, which would expand relativistically (e.g. Shemi & Piran 1990), but a smoothly expanding fireball would convert most of its energy into kinetic energy of accelerated barions rather than into luminosity. This problem was solved with the introduction of the fireball shock model (Rees & Mészáros 1992; Rees & Mészáros 1994) based on the fact that shock waves would inevitably occur in the outflow, and these would reconvert the kinetic energy of expansion into nonthermal particles and radiation energy (see Fig. 1.4). Similarly to what is observed by spacecraft in interplanetary shocks, the ones in the fireball outflow are expected to be collisionless, i.e. mediated by chaotic electric and magnetic fields. A turbulent magnetic field could be built up behind the shocks. A beamed jet would reduce the energy requirements and some observational evidence suggests its presence (e.g. Sari, Piran & Halpern 1999; Jensen et al. 2001). Whether a jet is present or not, such energies are in principle achievable for bursts arising from stellar progenitors, but, how this energy is converted into an ultrarelativistic and possibly collimated bulk outflow is still not well understood. Moreover, the progenitors of GRBs are, so far, not well identified. One class of candidates involves massive stars whose core collapses, probably in the course of merging with a companion (e.g. hypernovae, collapsars - for details, see Mészáros 2001). Other possible candidates are neutron star binaries or neutron star - black hole binaries, which loose orbital angular momentum by gravitational wave radiation and undergo a merger. All these progenitors are expected to have as final result the formation of a few solar masses black hole, surrounded by a temporary torus whose accretion can provide a sudden release of gravitational energy sufficient to power a burst. An e^\pm , γ fireball arises from the enormous compressional heating and dissipation associated with the accretion, possibly involving a small fraction of baryons and magnetic fields in excess of 10^{15} Gauss, which can provide the driving stresses leading to the relativistic expansion. This fireball may be substantially collimated, if the progenitor is a massive star, where an extended, fast-rotating envelope can provide a natural escape way or funnel for the fireball along the rotation axis. Other possible alternatives include the formation from a stellar collapse of a fast-rotating ultra-high magnetic field neutron star (e.g. Spruit 1999), or the tidal disruption of a compact star by a 10^5 – $10^6 M_\odot$ black hole.

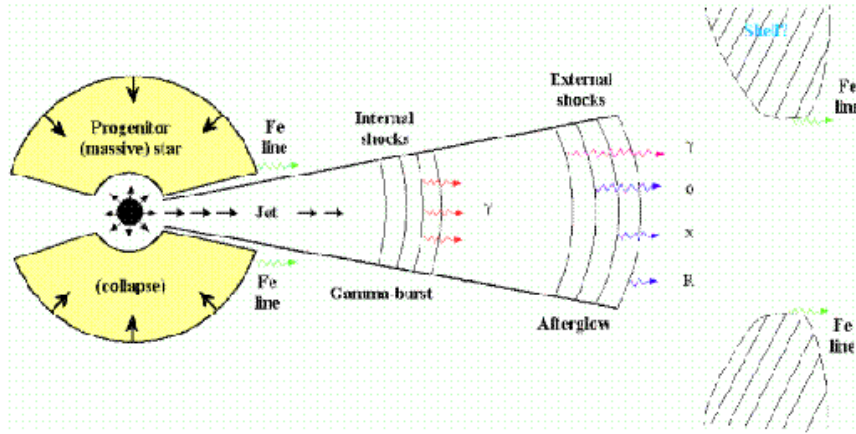


Figure 1.4: Schematic GRB from a massive stellar progenitor, resulting in a relativistic jet which undergoes internal shocks producing a burst of γ -rays and (as it decelerates through interaction with the external medium) an external shock afterglow which leads successively to γ -rays, X-rays, optical and radio. Iron lines may arise from X-ray illumination of a pre-ejected shell (e.g. supernova remnant) or from continued X-ray irradiation of the outer stellar envelope (Mészáros 2001).

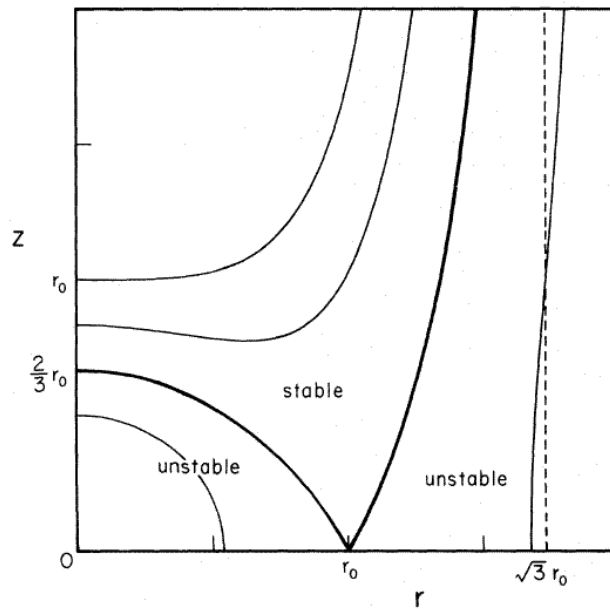


Figure 1.5: Equipotential surfaces for a bead on a wire. The dashed line at $r = \sqrt{3}r_0$ is the asymptote for the surface of marginal stability which reaches infinity in z direction (Blandford & Payne (1982); see also text in § 1.2).

GRBs remain at the moment an enigmatic cosmic phenomenon and one of the most important open questions is whether the burst emission is isotropic or strongly beamed in our direction.

1.2 The standard model - A magnetic jet

The standard model of a jet-disk system has been an original idea of Blandford & Payne (1982). Energy and angular momentum are removed magnetically from the accretion disk by field lines anchored to the disk surface and extending to large distances. The magnetic field lines are taken to be frozen into the disk and the plasma is assumed to follow them like a bead on a wire. The rotational energy of the disk plasma is used to power a magnetized centrifugally driven outflow that might dissipate its energy in the regions of observed radio emission.

Blandford & Payne (1982) show that a centrifugally driven outflow of matter from the disk is possible, if the poloidal component (through the meridional plane) of the magnetic field is lower than a certain angle. This can be shown by comparing equipotential surfaces for a bead on a wire, corotating with the Keplerian angular velocity $(GM/r_0^3)^{1/2}$ at a radius r_0 . The equation of the surfaces, in cylindrical coordinates, is

$$\Phi(r, z) = -\frac{GM}{r_0} \left[\frac{1}{2} \left(\frac{r}{r_0} \right)^2 + \frac{r_0}{((r^2 + z^2)^{1/2})} \right] = \text{constant} \quad (1.1)$$

(see Fig. 1.5).

If the projection of the wire on the meridional plane makes an angle of less than 60° with the equatorial plane, the equilibrium at $r = r_0$ is unstable. This means there is no potential barrier to the flow, that can freely leave the disk and be accelerated outwards by the strong centrifugal force. If the angle is greater than 60° , the equilibrium is stable, therefore there is a potential barrier (above the disk) to the flow and the mass flux rapidly decreases.

The disk wind, being first accelerated centrifugally, reaches the Alfvén point at large distances from the disk. Then, the toroidal component (azimuthal direction) of the magnetic field becomes important, pinching the poloidal outflow (self-collimation) into a pair of anti-parallel jets moving perpendicular to the disk (see also Fig. 1.6).

1.3 The matter content of jets

Whereas jets from forming stars are believed to be molecular material entrained by faster outflow of atomic material, the basic nature of AGN and microquasars jets has not been unambiguously determined. Possibilities include an electron-proton *heavy* plasma (i.e. normal material) and an electron-positron *light* plasma (i.e. a pair plasma).

For microquasars we do not really know whether the jet consists of a e^-p^+ or a e^-e^+ plasma (see e.g. Fender et al. 2000). It could be possible that these jets are *light* jets (made of a pair plasma only) and we would not expect to observe an iron line emission from such jets. Instead, the iron line emission would then arise from processes

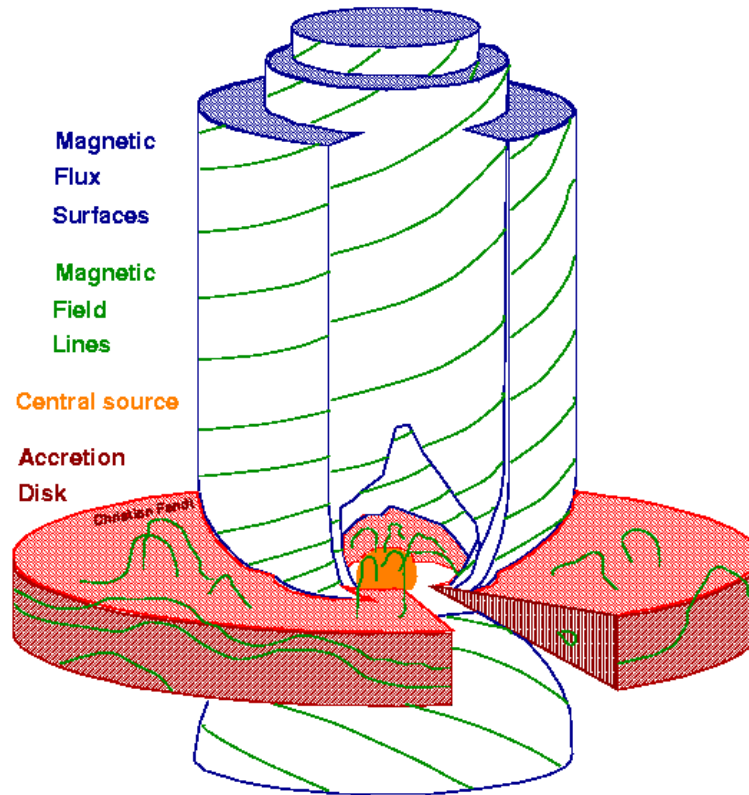


Figure 1.6: The model of jet formation from accretion disks. The three component system – central object, accretion disk, jet – is coupled by magnetic field. An accretion disk surrounding the central object is essential for jet formation. An important difference between stellar jets and black hole jets is that the magnetic field of jets from black holes must be generated by the surrounding accretion disk, in fact, it can not be provided by the central collapsed object. The accreting material is partially redirected into the jet, clearly no mass outflow is possible from a black hole in contrary to a stellar wind. Credit: Ch. Fendt.

connected to the accretion disk or an accretion column. Such models were discussed for example in the case of XTE J1748–288 (Kotani et al. 2000; Miller et al. 2001). Nevertheless, observations in the radio and shorter wavelengths give clear indication for synchrotron emission from highly relativistic electrons. Whether this non thermal particle population contributes to all of the observed emission is not clear, a hot thermal plasma may also exist besides the non thermal electrons.

For AGN relativistic jets theoretical and observational arguments concerning the hypothesis of *heavy* plasma jets and *light* plasma jets have been discussed almost 20 years ago from Begelman, Blandford & Rees (1984), but no definite conclusion could be drawn. Celotti & Fabian (1993) have addressed the issue of the matter content of jets

in a sample of radio-loud quasars and radio galaxies. Combining the synchrotron self-Compton constraints with indications of the kinetic luminosity, they suggest that, *for the sample as a whole*, the jets are heavy. Two main issues remain unsolved: the source of the soft photons that are inverse Compton scattered, and the structure of the inner jet, which cannot be imaged directly. The soft photons can originate as synchrotron emission either within the jet (see e.g. Bloom & Marscher 1996) or nearby the accretion disk, or they can be disk radiation reprocessed in broad emission line clouds (see e.g. Ghisellini & Madau 1996). Results of Reynolds et al. (1996) indicate the M87 jet to be dominated by electron-positron (pair) plasma, although an electron-proton plasma can not be conclusively dismissed. In contrast to these leptonic jet models, the proton-initiated cascade model (see e.g. Mannheim & Biermann 1989) predicts that the high-energy emission comes from knots in jets as a consequence of diffusive shock acceleration of protons to energies so high that the threshold of secondary particle production is exceeded.

Heavy jets fit with relativistic magnetohydrodynamic (MHD) models for the formation, acceleration and collimation of jets, which predict asymptotic solutions with a slow but efficient conversion from magnetic to kinetic powers (Li, Chiueh & Begelman 1992).

Chapter 2

Two-dimensional magnetic field structure of relativistic jets: setup of the theoretical problem

2.1 Magnetic jets

Beside observations of astrophysical jet sources, also theoretical considerations have shown that magnetic fields play an important role in jet formation and propagation (Blandford & Payne 1982; Pudritz & Norman 1983; Sakurai 1985; Camenzind 1987; Lovelace, Berk & Contopoulos 1991). However, the jet formation process itself is still theoretically not fully understood.

Magnetic jets are claimed to originate very close to the central object in the interaction region with the accretion disk. If the central object is a black hole, like in AGN and in some microquasars, the surrounding accretion disk is the only possible location for a field generation. The magnetic field is believed to be generated and enhanced by dynamo action within the accretion disk (Camenzind 1990; Rüdiger, Elstner & Stepinski 1995). A stellar central object (protostar, white dwarf, neutron star) probably carries a magnetosphere built up by a strong stellar dynamo and is surrounded by an accretion disk, therefore it is not yet clear whether the jet magnetosphere originates in the disk or in the star.

A complete theoretical description of the jet formation process requires a solution of the time-dependent MHD equations in three dimensions. The general solution of the problem is not yet possible either analytically and numerically, therefore, the only way to approach the problem is the use of simplifying assumptions.

The structure and dynamics of the collimation region of a magnetized jet can be in-

investigated under the assumptions of stationarity and axisymmetry. In this case, the problem can be decoupled: the magnetic field structure follows from the force-balance perpendicular to the magnetic field, which is described by the Grad-Shafranov equation (2.18), the plasma dynamics along the field lines is given by the wind-equation (4.1). In the very general case, these two equations are not independent, in fact, the dynamical parameters of the plasma are needed in the Grad-Shafranov equation and the magnetic structure is needed in the wind-equation. Anyway, dealing with both equations simultaneously is always so complicated that, so far, no self-consistent solution of the problem has been found.

The magnetic flux distribution is determined by the solution of the Grad-Shafranov equation (2.18) for the cross-field force-balance. Appl & Camenzind (1993a,b) investigated the asymptotic Grad-Shafranov equation in the case of constant field rotation. For the first time they found a nonlinear analytical solution for a cylindrically collimated asymptotic field distribution and derived relations between jet radius, current strength, field and current distribution. These results were used as boundary condition for the calculation of global two-dimensional force-free jet magnetospheres (Fendt, Camenzind & Appl 1995; Fendt 1997a). However, since the jet motion is connected to an accretion disk that rotates differentially, the jet magnetosphere, if anchored into the disk, essentially obeys *differential rotation*, that should therefore be taken into account in the calculation of the jet magnetic structure. Ferreira (1997) showed that *differential rotation* plays a major role in recollimation of jets and their asymptotic behaviour. The results of Appl & Camenzind (1993a,b) were further generalized by Fendt (1997b) for the asymptotic trans-field force-balance including *differential rotation*. Such an asymptotic field distribution is of particular interest for jets emerging from differentially rotating accretion disks.

In the following two chapters we describe how we determine the global two-dimensional field structure of stationary, axisymmetric, relativistic, strongly magnetized (force-free) jets collimating into an asymptotically cylindrical jet (taken as boundary condition) anchored in a *differentially rotating* accretion disk. This approach allows for a direct connection between the accretion disk and the asymptotic collimated jet. The essential problem for differentially rotating relativistic jet magnetospheres is that position and shape of the singular light surface are not known *a priori*, but have to be calculated in an iterative way together with the magnetic flux distribution (see §2.4.1).

The physical dimensions of the collimation region we investigate are tiny. Imagine the size of the arcmin scale in Fig. 2.1 (Döbereiner et al. 1996) divided by a factor of 10^6 in the case of a *close* AGN as M87 (see also § 3.7) and by a factor of 10^9 in case of a quasar like 3C 273. In the latter case, a resolution of about 10^{-6} arcsec is necessary to observe the collimation region, and even radio telescopes would not provide it. Therefore, for most of the extragalactic jet sources theoretical models are the only possibility to get information about the physical processes in the innermost jet region.

2.2 Assumptions

Here we discuss the model assumptions behind our numerical calculation:

- **Ideal MHD**

Ideal MHD is characterized by an infinite electrical conductivity ($\sigma \rightarrow \infty$), which implies that the magnetic field lines are frozen into the plasma (see § 2.3). As a consequence of ideal MHD, Ferraro's law of iso-rotation is satisfied (Ferraro 1937). The use of ideal MHD is justified by jets being fully ionized plasma objects.

- **Stationarity**

For the question of jet collimation, we can assume that the collimation time scale is much shorter than the kinetic life time of the jet itself. This means we can assume stationarity in the very innermost jet region, that implies $\partial/\partial t = 0$. Both assumptions of stationarity and axisymmetry are limited by the observations of jet-knots showing asymmetries and time-variability, but, concerning the description of jets generation, stationarity and axisymmetry are for sure no limitation.

- **Axisymmetry**

Observations show that extragalactic jets (see Fig. 2.1) as well as Galactic superluminal jets and protostellar jets are collimated almost to a cylindrical shape (Zensus, Cohen & Unwin 1995; Ray et al. 1996; Mirabel & Rodríguez 1995). Theoretically, it has been shown that current carrying relativistic jets must collimate to a cylinder (Chiueh, Li & Begelman 1991).

In our theoretical model we assume that jets are axisymmetric objects and we use cylindrical coordinates (R, ϕ, Z), which properly describe the observed geometry. Axisymmetry means $\partial/\partial\phi = 0$.

- **Force-freeness**

We assume that the inertial and gravitational forces acting on the plasma are small compared to the electromagnetic forces (see §2.4.2). It is reasonable for relativistic jets, that reveal the presence of strong magnetic fields. This is the *force-free* limit and the equation of motion, considering the relativistic Lorentz force, reduces to:

$$0 = c\rho_c \mathbf{E} + \mathbf{j} \times \mathbf{B}, \quad (2.1)$$

where \mathbf{E} is the electric field, \mathbf{B} the magnetic field, \mathbf{j} the current density and ρ_c the charge density.

Starting points for our calculations are the basic assumptions of ideal MHD, stationarity and axisymmetry. As known, in physical contexts, every symmetry leads to a conserved quantity. Out of stationarity follows the conservation of energy, the axisymmetry leads to the conservation of angular momentum. A non-axisymmetric problem would imply that time-dependency has to be taken into account.

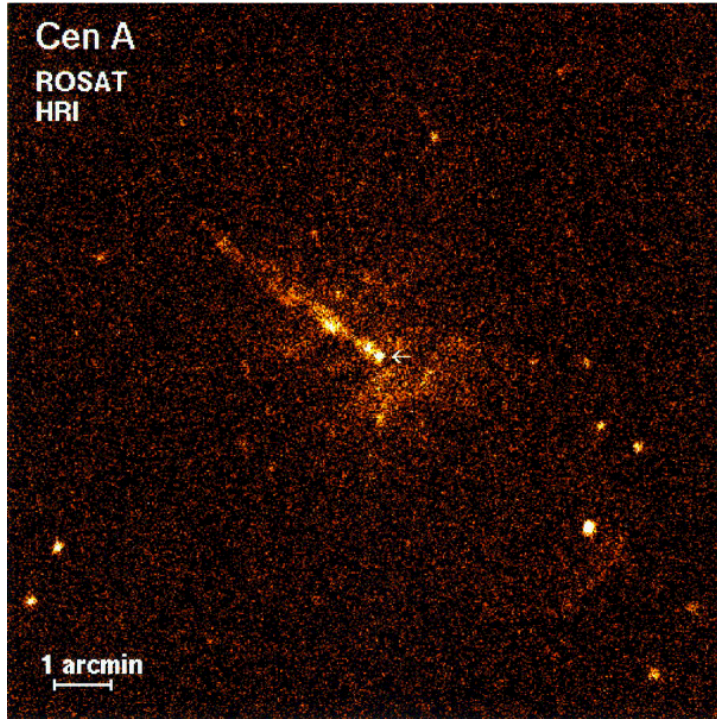


Figure 2.1: ROSAT HRI image of Centaurus A (sum of HRI observations in 1990 and 1994). The field size is 12.8×12.8 ; north is up, and east is to the left. The nucleus is marked with an arrow (Döbereiner et al. 1996).

2.3 Basics of MHD

The theory of magnetohydrodynamics describes the subject main concern: the dynamics of electrically conducting fluids in the presence of magnetic fields. Under the assumption of stationarity mentioned above (see §2.2), Maxwell's equations, in the **cgs** units system, have the following form:

$$\nabla \times \mathbf{E} = 0 \quad (2.2)$$

$$\nabla \times \mathbf{B} = \frac{4\pi}{c} \mathbf{j} \quad (2.3)$$

$$\nabla \cdot \mathbf{E} = 4\pi \rho_c \quad (2.4)$$

$$\nabla \cdot \mathbf{B} = 0. \quad (2.5)$$

Ohm's law is $\mathbf{j} = \sigma \left(\mathbf{E} + \frac{\tilde{\mathbf{u}}}{c} \times \mathbf{B} \right)$, where σ is the electric conductivity and $\tilde{\mathbf{u}}$ the Newtonian velocity of the plasma. In ideal MHD Ohm's law transforms into:

$$\mathbf{E} = -\frac{\tilde{\mathbf{u}}}{c} \times \mathbf{B}. \quad (2.6)$$

From the stationary Faraday's law (2.2) it follows that the electric field must be a gradient of a potential $\mathbf{E} = \nabla U$. As a consequence of axisymmetry ($\partial/\partial\phi = 0$) it is $E_\phi = 0$, therefore $\mathbf{E}_P = -\frac{\tilde{\mathbf{u}}}{c} \times \mathbf{B}$ (note that the index P marks the poloidal component and the index ϕ the toroidal one). This brings to:

$$\tilde{\mathbf{u}}_P \times \mathbf{B}_P = 0 \quad \implies \quad \tilde{\mathbf{u}}_P \parallel \mathbf{B}_P, \quad (2.7)$$

that means the plasma moves along the field line, but not parallel to the field line.

2.4 The Grad-Shafranov equation

Under the assumptions discussed above (§ 2.2), a magnetic flux function Ψ can be defined,

$$\Psi(R, Z) = \frac{1}{2\pi} \int \mathbf{B}_P \cdot d\mathbf{A}, \quad R\mathbf{B}_P = \nabla\Psi \times \mathbf{e}_\phi. \quad (2.8)$$

Therefore, $B_R = \frac{1}{R}\partial_Z\Psi$ and $B_Z = -\frac{1}{R}\partial_R\Psi$. The Ψ function measures the magnetic flux through a circular area around the symmetry axis with radius R . The condition $\mathbf{B}_P \cdot \nabla\Psi = 0$ is fulfilled, therefore the Ψ function defines the poloidal field lines. Each field line will connect points with the same Ψ value. Similarly to Eq. (2.8), the total poloidal electric current I through the same area is defined:

$$I(R, Z) = \int \mathbf{j}_P \cdot d\mathbf{A} = -\frac{c}{2} RB_\phi(R, Z), \quad (2.9)$$

where $\mathbf{j}_P = \frac{c}{4\pi R}\nabla(RB_\phi) \times \mathbf{e}_\phi$ is the poloidal electric current density, derived from the poloidal component of Ampère's law (2.3), and B_ϕ is the toroidal magnetic field.

From Eqs. (2.7) and (2.8) it follows that:

$$\begin{aligned} \tilde{\mathbf{u}} \times \mathbf{B} &= \tilde{\mathbf{u}}_\phi \times \mathbf{B}_P + \tilde{\mathbf{u}}_P \times \mathbf{B}_\phi \\ &= (\tilde{\mathbf{u}}_\phi \cdot \nabla\phi)\nabla\Psi - \frac{\eta}{n}(\mathbf{B}_\Phi \cdot \nabla\phi)\nabla\Psi \\ &= \frac{1}{R}(\tilde{u}_\phi - \frac{\eta}{n}B_\phi)\nabla\Psi, \end{aligned} \quad (2.10)$$

where $\eta = \eta(\Psi)$ is the particle flow rate per field line and n is the particle density in the lab frame.

From Eq. (2.10) we learn that the expression before the $\nabla\Psi$ is a conserved quantity. We define this as $\Omega_F(\Psi)$ (Eq. 2.11). We call $\Omega_F = \Omega_F(\Psi)$ the *iso-rotation* parameter,

which is a conserved quantity along each field line and the corresponding flux surface (Ferraro's law of iso-rotation, Ferraro 1937) and can be understood as the angular velocity of the foot points of the field lines anchored into the disk:

$$\Omega_{\text{F}}(\Psi) = \frac{1}{R} \left(\tilde{u}_{\phi} - \frac{\eta}{n} B_{\phi} \right). \quad (2.11)$$

In particular, the Newtonian velocity is:

$$\tilde{\mathbf{u}} = \frac{\eta}{n} \mathbf{B} + \Omega_{\text{F}} R \mathbf{e}_{\phi}, \quad (2.12)$$

where

$$n = \gamma n' \quad \text{and} \quad u = \gamma \tilde{u}/c$$

n' is the proper particle density (in the rest frame of the plasma). Therefore, Eq. 2.12 can be immediately extended to the space components of the relativistic 4-velocity as follows:

$$\mathbf{u}_{\text{P}} = \frac{\eta}{cn'} \mathbf{B}_{\text{P}} \quad (2.13)$$

$$\mathbf{u}_{\phi} = \frac{\eta}{cn'} \mathbf{B}_{\phi} + \frac{\gamma}{c} \Omega_{\text{F}} R \mathbf{e}_{\phi}. \quad (2.14)$$

Equations (2.13) and (2.14) show that the plasma is always moving along the field lines, as already found in the ideal MHD section (see §2.3, Eq. (2.7)).

Relativistic magnetohydrodynamics implies that electric fields, which are negligible in Newtonian MHD, cannot be neglected anymore. From Eqs. (2.6), (2.10) and (2.11) it follows that:

$$\mathbf{E} = -\frac{1}{c} \Omega_{\text{F}} \nabla \Psi. \quad (2.15)$$

In the high conductivity limit, plasma is forced to flow along the magnetic flux surfaces and these surfaces are also electric potential surfaces, i.e. the electric field \mathbf{E} is orthogonal to the magnetic surface (Camenzind 1990).

From Eqs. (2.4), (2.8), (2.11), the charge density ρ_c is:

$$\begin{aligned} \rho_c &= \frac{1}{4\pi} \nabla \cdot \mathbf{E} \\ &= -\frac{1}{4\pi c} \nabla \cdot (\Omega_{\text{F}} \nabla \Psi) \end{aligned}$$

$$\begin{aligned}
 &= -\frac{1}{4\pi c}(\Omega_F \nabla \cdot (R\mathbf{e}_\phi \times \mathbf{B}_P) + \nabla \Psi \cdot \nabla \Omega_F) \\
 &= -\frac{R\Omega_F}{c^2} j_\phi - \frac{1}{4\pi c} \frac{\Omega_F}{R^2} (\nabla \Psi \times R\mathbf{e}_\phi) \cdot (\nabla \times R\mathbf{e}_\phi) - \frac{1}{4\pi c} \nabla \Psi \cdot \nabla \Omega_F \\
 &= -\frac{R\Omega_F}{c^2} j_\phi - \frac{1}{4\pi c R^2} (\nabla \Psi \cdot \nabla) (R^2 \Omega_F), \tag{2.16}
 \end{aligned}$$

j_ϕ is the toroidal electric current density.

The structure of the magnetic field can be derived by the toroidal component of Ampère's law,

$$\nabla \times \mathbf{B}_P = \frac{4\pi}{c} \mathbf{j}_\phi. \tag{2.17}$$

From Eq. (2.8) we express \mathbf{B}_P in terms of Ψ , then, from Eq. (2.17), we obtain the Grad-Shafranov equation, that is Ampère's law rewritten for the Ψ function:

$$R \nabla \cdot \left\{ \frac{1}{R^2} \nabla \Psi \right\} = -\frac{4\pi}{c} j_\phi. \tag{2.18}$$

The toroidal electric current density j_ϕ has to be calculated from the equation of motion projected perpendicular to the flux surfaces (a derivation is given in Camenzind 1987; Fendt, Camenzind & Appl 1995), note that it is always $\Omega_F = \Omega_F(\Psi)$,

$$j_\phi = \frac{c}{4\pi} \frac{1}{(1 - (R\Omega_F/c)^2)} \left(\frac{4}{c^2} \frac{1}{R} I(\Psi) \partial_\Psi I(\Psi) - \frac{\Omega_F}{c^2} \frac{1}{R} (\nabla \Psi \cdot \nabla) (R^2 \Omega_F) \right). \tag{2.19}$$

Combining Ampère's law, Eq. (2.17), and the force-free equation of motion, Eq. (2.1), using also Eqs. (2.16) and (2.19), the cross-field force-balance can be written as the *modified* relativistic Grad-Shafranov (hereafter GS) equation. Here, the term $(1 - (R\Omega_F(\Psi)/c)^2)$ has been absorbed in the divergence term on the left hand side of the Grad-Shafranov equation (2.18),

$$R \nabla \cdot \left(\frac{1 - (R\Omega_F(\Psi)/c)^2}{R^2} \nabla \Psi \right) = -\frac{4}{c^2} \frac{1}{R} \frac{1}{2} \left(I^2(\Psi) \right)' - R |\nabla \Psi|^2 \frac{1}{2} \left(\Omega_F^2(\Psi) \right)', \tag{2.20}$$

where the primes denote the derivative $\frac{d}{d\Psi}$ (see Camenzind 1987; Okamoto 1992; Fendt & Memola 2001a). In the force-free MHD case, the poloidal current $I(R, Z)$ (see Eq. (2.9)) is a conserved quantity along the field line, that means $I = I(\Psi(R, Z))$. The light cylinder of a flux surface Ψ is defined as a cylinder with radius $R = R_L(\Psi) = c/\Omega_F(\Psi)$ (see also §2.4.1). At a certain radius $R_L(\Psi)$, for each flux surface it is $1 - (R\Omega_F(\Psi)/c)^2 = 0$, that means every flux surface (magnetic field line) has its own light cylinder, whose radius we denote as R_L . Projecting the flux surfaces on a meridional

plane, the light points, where the field lines intersect their light cylinder, define the light cylinder radii. The light points have coordinates $(R_L(\Psi), Z_L(\Psi))$ and lay on a surface called light surface, which shows the relativistic character of the GS equation (2.20). In particular, R_0 is the radius of the asymptotic branch of the light surface, the asymptotic light cylinder radius, therefore it is also $R_0\Omega_F(\Psi)/c = 1$ (see § 2.4.1). The term *asymptotic* denotes the limit of $Z \gg R$. We consider jets with a *finite* radius, $R < \infty$ for $Z \rightarrow \infty$. Beyond the light surface, that is the Alfvén surface in the force-free limit, the Alfvén velocity is not defined, that means Alfvén’s waves can not propagate.

Both, the current distribution $I(\Psi)$ and the rotation law $\Omega_F(\Psi)$ determine the source term (right hand side) of the GS equation and govern the structure of the magnetosphere. We apply the following normalizations,

$$\begin{aligned} R, Z &\Leftrightarrow x R_0, z R_0, \\ \Omega_F &\Leftrightarrow \Omega_F (c/R_0), \\ \Psi &\Leftrightarrow \Psi \Psi_{\max}, \\ I &\Leftrightarrow I I_{\max}. \end{aligned}$$

As the length scale for the GS equation, Eq. (2.20), the asymptotic radius of the light surface, R_0 , is selected. In order to allow for a direct comparison to rigidly rotating magnetospheres, the normalization was chosen such that $\Omega_F = 1$ at $x = 1$. With the chosen normalization, Eq. (2.20) can be written dimensionless,

$$x \nabla \cdot \left(\frac{1 - x^2 \Omega_F^2(\Psi)}{x^2} \nabla \Psi \right) = -\frac{1}{x} \frac{g}{2} \left(I^2(\Psi) \right)' - x |\nabla \Psi|^2 \frac{1}{2} \left(\Omega_F^2(\Psi) \right)'. \quad (2.21)$$

The coupling constant g describes the strength of the current term in the GS equation,

$$g = \frac{4 I_{\max}^2 R_0^2}{c^2 \Psi_{\max}^2} = 4 \left(\frac{I_{\max}}{10^{18} \text{ A}} \right)^2 \left(\frac{R_0}{10^{16} \text{ cm}} \right)^2 \left(\frac{\Psi_{\max}}{10^{33} \text{ G cm}^2} \right)^{-2},$$

where here the parameters are chosen for extragalactic jets (Camenzind 1987; Blandford, Netzer & Woltjer 1990). We obtain the numerical solution of the GS equation using the Finite Element Code (see also Appendix and Chapter 3), as developed by Camenzind (1987); Fendt, Camenzind & Appl (1995); Fendt & Memola (2001a); Memola & Fendt (2001).

2.4.1 Regularity condition along the light surface

The light cylinder and more generally the light surface appear as a characteristic quantity of the relativistic MHD compared to the Newtonian description. For constant Ω_F the light surface is of cylindrical shape.

If the light cylinder radius is smaller than the jet radius, a relativistic treatment is required (Camenzind 1987).

Along the light surface the term $1 - x^2\Omega_F^2(\Psi)$ vanishes ($D \equiv 1 - x^2\Omega_F^2(\Psi) = 0$). As a consequence, the GS equation reduces to the regularity condition:

$$\nabla\Psi \cdot \nabla D = -g\frac{1}{2} \left(I(\Psi)^2 \right)' - \frac{1}{2} |\nabla\Psi|^2 \left(\ln \left(\Omega_F(\Psi)^2 \right) \right)', \quad (2.22)$$

that is equivalent to a Neumann boundary condition along the light surface. However, for differentially rotating magnetospheres with $\Omega_F = \Omega_F(\Psi)$ the shape of this surface is not known a priori and has to be calculated in an iterative way together with the two-dimensional solution of the GS equation.

The search for the exact position of the light surface and for regular solutions across that light surface was one of the main goals of the thesis. At the light surface the Grad-Shafranov equation (2.18) becomes singular (note that we solve the dimensionless force-free *modified* GS equation (2.21) with the Finite Element Code, where that singularity has been removed).

We already defined the light cylinder of a flux surface Ψ as a cylinder with radius $R = R_L(\Psi) \equiv c/\Omega_F(\Psi)$. The light cylinder is important for a projected poloidal field line only *if* the field line actually intersects it as for Ψ_{out} in Fig. 2.2. Then, relativistic effects become dominant. For example, the poloidal electric field scales with the radius in units of the light cylinder radius, $E_{\perp} = (R/R_L)B_P$. On the other hand, in the case of Ψ_{in} in Fig. 2.2, the asymptotic radius of the flux surface is smaller than its light cylinder radius $R_L(\Psi_{\text{in}})$ (located between Ψ_{in} and Ψ_0). For jet solutions with rigid rotation Ω_F all flux surfaces have the same light cylinder radius. Thus, the singular light surface of the magnetosphere is a cylinder. For jet solutions with *differential rotation* Ω_F the flux surfaces have different light cylinder radii. The singular surface of the magnetosphere is not a cylinder anymore.

A relativistic description for the jet magnetosphere is always required if the jet contains a flux surface for which the light radius is smaller than the asymptotic radius.

The numerical determination of the true light surface was a quite difficult task (see also § 3.2).

2.4.2 Discussion of the force-free assumption

The force-free assumption simplifies considerably the problem of solving the *modified* GS equation (2.21).

It is clear that relativistic jets must be highly magnetized. Only a high plasma magnetization (a large magnetic flux compared to the mass flow rate) gives jet velocities close to the speed of light (Michel 1969; Begelman & Li 1994; Fendt & Camenzind 1996). Conversely, if particles are being accelerated to relativistic energies, pressure and gravitational effects should be small. Therefore, for the calculation of the field structure the force-free limit seems to be reasonable.

In general, the non force-free relativistic GS equation shows three inertial contributions: the gas pressure, the centrifugal force and the poloidal field curvature (see Chiueh, Li & Begelman 1991). It can be shown that in the asymptotic, cylindrical jet the contribution of inertial terms in the force-balance across the field is weak. The contribution of gas pressure is usually negligible in astrophysical jets. Also, the centrifugal force does not play a major role outside the Alfvén surface (which is the light surface for low plasma density) since the plasma moves with constant angular momentum. The curvature term vanishes in cylindrical geometry. Therefore, since for cylindrical jets and high magnetization the contribution from inertial terms is weak, the configuration is comparable to the force-free case.

The main motivation of the force-free assumption is clearly the reason of simplification, however, there is yet no other way to calculate a truly two-dimensional field distribution for relativistic jets. With a force-free solution nothing can be said about the flow acceleration itself, no matter/particle dynamics is involved!

2.5 Boundary conditions

The GS equation is a non linear, elliptic, partial differential equation of second order and it is numerically solved as boundary value problem applying the Finite Element Code.

The choice of astrophysical boundary conditions, that will be discussed in the following paragraphs, determine the two-dimensional flux distribution (Fig. 2.2).

2.5.1 The asymptotic jet

A first boundary condition is in the asymptotic region. Here we assume a cylindrically collimated jet. We apply the magnetic flux distribution derived by Fendt (1997b), where the rigidly rotating jet model of Appl & Camenzind (1993b) has been extended for *differential rotation* $\Omega_{\text{F}}(\Psi)$. In particular, the asymptotic jet shows the typical jet core-envelope structure of magnetic flux and electric current, a configuration where most of the magnetic flux and poloidal electric current is concentrated within a *core* radius, a . The asymptotic solution of the GS equation provides not only the asymptotic magnetic flux boundary condition but also the $\Omega_{\text{F}}(\Psi)$ and $I(\Psi)$ distribution for the whole two-dimensional jet magnetosphere, for the reason that these are conserved quantities along the field lines. These functions follow from the numerical solution $\Psi(x)$ of the one-dimensional (asymptotic) GS equation across the cylindrical jet. This solution corresponds to a core radius of the electric current distribution of unity.

$$\begin{cases} I^2(\Psi) &= \left(\frac{x^2}{(1+x^2)} \right)^2, \\ \Omega_{\text{F}}^2(\Psi) &= e^h - hx \end{cases}$$

note that $I(x) = \left(\frac{x^2}{(1+x^2)} \right) = I(x(\Psi)) = I(\Psi)$.¹ The parameter h governs the steepness of the Ω_{F} -profile.

2.5.2 The disk

A second boundary condition is the magnetic flux distribution along the disk. This distribution is in general not known as a solution of the full MHD disk equations. Typical models rely on various simplifying assumptions, as stationarity, distribution of magnetic resistivity or disk turbulence governing a dynamo process. We apply an analytical magnetic flux distribution whose typical behaviour is: 1) a slight increase of magnetic flux along the innermost disk, 2) a small or vanishing flux at the inner disk radius, 3) a strong increase of magnetic flux at intermediate radius (the core radius) and 4) a saturating behavior for large radii. A similar flux distribution was used by Khanna & Camenzind (1992), who calculated the stationary accretion disk magnetic field structure around a super massive black hole.

Using the normalization introduced above, we choose the following disk boundary magnetic flux distribution,

$$\Psi_{\text{disk}}(x) = \frac{1}{b} \ln \left(1 + \left(\frac{x}{a} \right)^2 \right) \quad (2.23)$$

with $b = \ln(1 + (x_{\text{disk}}/a)^2)$ (see Fig. 2.3), where x_{disk} is the disk outer radius and $a = \frac{x_{\text{disk}}}{2}$ the core radius of the Ψ distribution, that means most of the magnetic flux is concentrated within a .

2.5.3 The collimating jet boundary

A third boundary condition is the collimating jet boundary $x_{\text{jet}}(z)$. Along this boundary the flux distribution is $\Psi = 1$ by definition. However, the shape of this boundary is not known *a priori*. It must be determined by the regularity of the solution across the light surface (see also Fendt, Camenzind & Appl 1995). A regular global solution can be obtained only for a certain choice of $z(x)$, $I(\Psi)$ and $\Omega_{\text{F}}(\Psi)$. The main features of the solution as opening angle or location of the collimation are fixed by the internal equilibrium. Therefore, the regularity condition governs the shape of the jet boundary. For a given $I(\Psi)$, $\Omega_{\text{F}}(\Psi)$, disk and jet boundary condition, the jet radius $x_{\text{jet}}(z)$ is uniquely determined.

¹For figures of these functions and the related $\Psi(x)$, $\Omega_{\text{F}}(\Psi)$ and $I(\Psi)$ distribution, please refer to Fendt (1997b).

2.5.4 Inner boundary conditions

Along the jet-axis the magnetic flux is *zero* by definition ($\Psi(x, z) = 0$). Including the jet-axis in our calculations is an important difference respect to a self-similar approach. Self-similarity assumes a set of one-dimensional functions following a power or exponential law and implies a singularity along the jet-axis. Our truly 2D solution is not self-similar.

The inner spherical grid boundary with radius x_* close to the origin indicates the regime of the central source. The boundary condition is an homogeneous Neumann condition, that means the field lines cross the boundary perpendicular. For simplicity we assume that the magnetic flux increases monotonously from the axis to the disk edge.

2.6 The jet-disk connection

An important point was to relate the jet parameters to the disk properties. So far (see below), no connection has been made to the type of central object. In this section we ask where the asymptotic light cylinder is located in physical units.

For relativistic jets the central source is a black hole. The Schwarzschild radius is defined as $R_S = 2GM_{\text{BH}}/c^2$. In case of rigid rotation, that implies the light surface being a cylinder ($R_0 = R_L$), the light cylinder radius is usually estimated by choosing a distinct radial distance from the central object and defining Ω_F under the assumption that the jet magnetosphere is anchored in that point. For a black hole central object, the marginally stable orbit implies an upper limit for Ω_F . For AGN jets this estimate leads to the common conclusion that the light cylinder radius is at about $\geq 10R_S$ and the typical jet radius at about $100 R_L$. Clearly, such an argumentation relies on the *assumption* that the field line emerging at this very special radius, which, at the same time, also defines the iso-rotation parameter Ω_F , does actually extend to the light cylinder radius R_L .

If *differential rotation* $\Omega_F(\Psi)$ is considered, the asymptotic light cylinder radius, R_0 , is related to the iso-rotation parameter $\Omega_F(\Psi)$, which itself is connected to the angular rotation of the foot points of the field lines (see also § 2.4). Concerning the GS equation, the size of R_0 follows purely from electro-magnetic quantities, if the coupling constant g is chosen. The GS solution can be scaled to any central object from stars to galactic nuclei as long as the interrelation of the parameters Ψ_{max} , I_{max} and R_0 provides the same g . Different flux surfaces anchor at different foot point radii and, thus, have different light radii (see Fig. 2.2). Assuming a Keplerian rotation, the light surface radius $R_L(\Psi)$, for each single flux surface, is located at:

$$R_L(\Psi) = 4 \times 10^{15} \text{cm} \left(\frac{R_D(\Psi)}{R_S} \right)^{3/2} \left(\frac{M}{10^{10} M_\odot} \right), \quad (2.24)$$

where R_S is the Schwarzschild radius of a point mass and $R_D(\Psi)$ the foot point of the flux surface Ψ on a Keplerian disk. A more general equation is

$$\frac{R_L(\Psi)}{R_S} = \sqrt{2} \left(\frac{R_D(\Psi)}{R_S} \right)^{3/2}. \quad (2.25)$$

$R_D(\Psi)$ is determined from the magnetic flux distribution along the disk and is defined by a certain disk model. Fig. 2.4 shows the location of the light radius R_L for a field line anchored at a foot point radius R_D in a Keplerian disk around a central object of mass M (see Eq. (2.24)). Note that the field line footpoint radius in Eq. (2.25) and Fig. 2.4 is normalized to the Schwarzschild radius. Therefore, Fig. 2.4 is appropriate only for relativistic jets. The footpoint radii for protostellar jets are several *stellar* radii, corresponding to about 10^6 Schwarzschild radii (which would be located far above the box in Fig. 2.4).

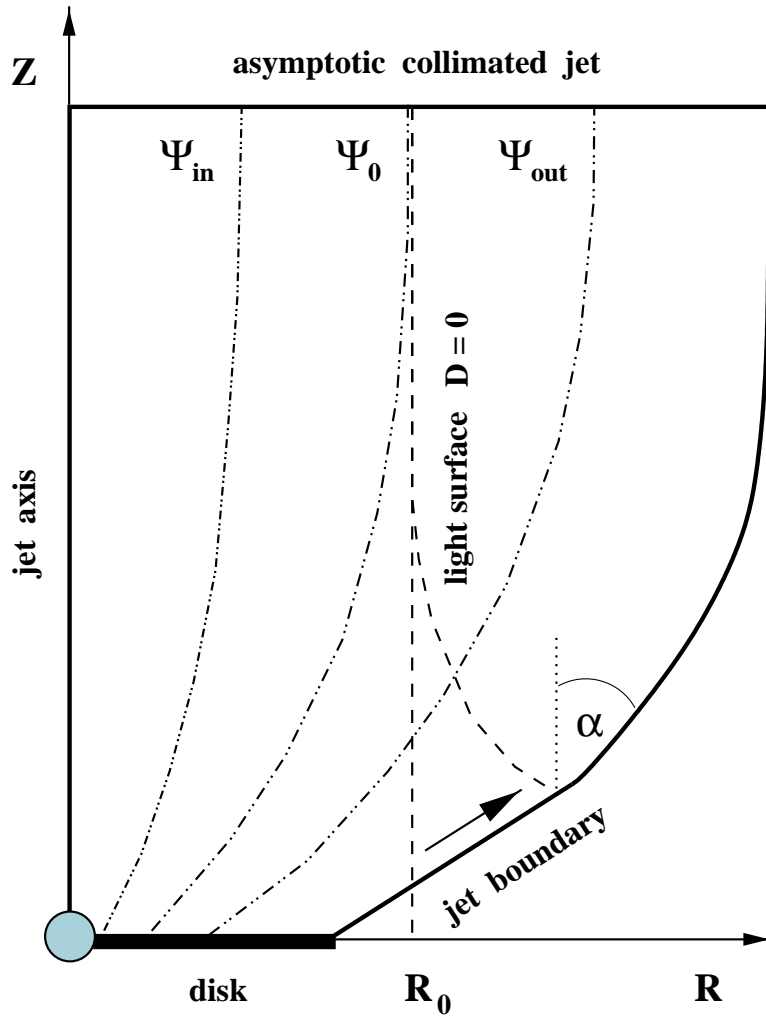


Figure 2.2: Sketch of our jet model. Shown are axisymmetric jet magnetic flux surfaces Ψ projected on the meridional plane. The central object, located within the inner boundary (solid disk), is surrounded by an accretion disk. Helical magnetic field lines are anchored in the differentially rotating disk at foot points $R_D(\Psi)$. The disk radius is a parameter. The shape of the jet boundary $\Psi = \Psi_{\max} = 1$ is constrained by the regularity condition along the light surface. The upper boundary condition is a cylindrically collimated jet solution (Fendt 1997b). The arrow indicates the numerical deformation of the initially vertical boundary of the inner solution (at $x = 1$) into the curved light surface. The flux surfaces Ψ_{in} (Ψ_{out}) have an asymptotic radius smaller (larger) than the asymptotic light cylinder R_0 , which is the asymptotic branch of the light surface $R_L(\Psi)$ for large z -values. The flux surface Ψ_0 coincides with the light surface asymptotically. The initial jet half opening angle is α .

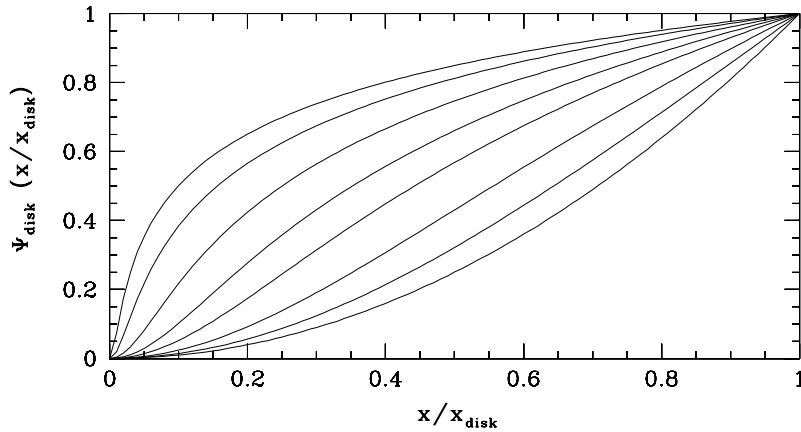


Figure 2.3: Magnetic flux distribution along the disk $\Psi_{\text{disk}}(x)$ as defined in Eq. (2.23). Parameters (from top to bottom, for different a values): $x_{\text{disk}}/a = 100, 40, 15, 7, 4, 2, 1, 0.01$. In our calculation $x_{\text{disk}}/a = 2$.

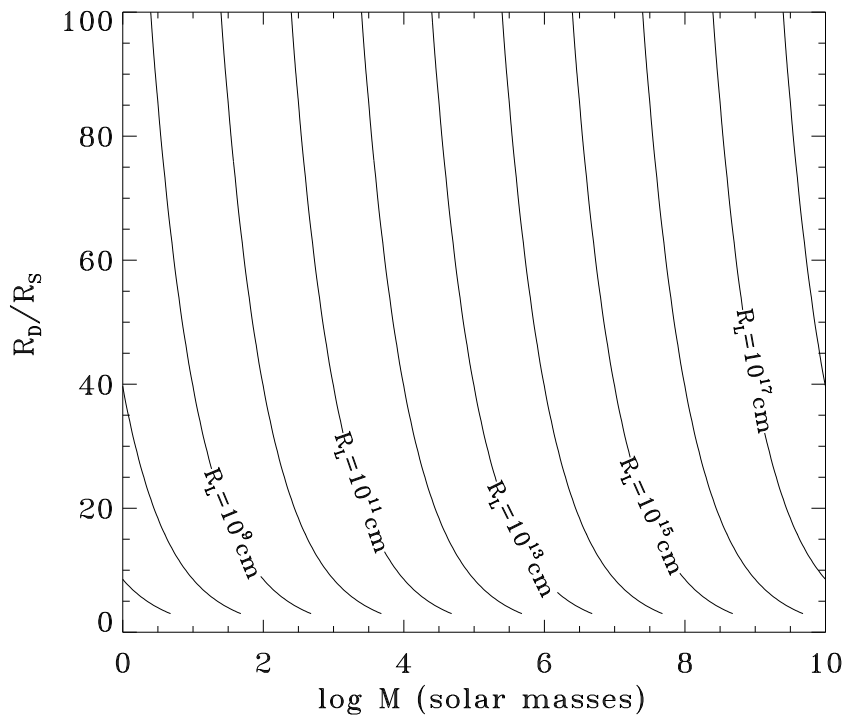


Figure 2.4: Location of the light cylinder radius of a flux surface, $R_L(\Psi)$, anchored at a certain foot point radius $R_D(\Psi)$ in units of the Schwarzschild radius R_S in a Keplerian disk around a point mass M (see § 2.6). Note that for non collapsed stellar objects the footpoint radii of the jet field lines are located at about $10^6 R_S$.

Chapter 3

Numerical results

3.1 The collimation region

The numerical results, concerning the solution of the GS equation (2.21), presented and discussed in the following chapter, have been obtained by running the Finite Element Code as developed by Camenzind (1987); Fendt, Camenzind & Appl (1995); Fendt & Memola (2001a); Memola & Fendt (2001).

In general, for a choice of the free functions $I(\Psi)$ and $\Omega_{\mathbb{F}}(\Psi)$, here taken from the asymptotic cylindrical jet solution, the field structure is determined by the boundary conditions and the regularity condition along the light surface. It is shown the two-dimensional structure of the magnetic flux surfaces $\Psi(x, z)$ as projection of the helical field lines into the meridional plane. We deal with two computational regions: the inner solution is numerically calculated from the jet-axis till the light surface (outer boundary for the inner solution); the outer solution starts from the light surface (inner boundary for the outer solution) and reaches the jet boundary. Inner and outer solutions are then attached in order to obtain the global two-dimensional solution from the jet-axis till the jet boundary. The light surface decouples inner and outer solutions. This implies that it is not always possible to fit each inner solution with an outer solution in order to provide a smooth transition of the field lines across the light surface.

We had two different approaches to the outer solution calculation. First we used the regularity condition for the inner boundary of the outer solution, but we got the result that inner and outer solution did not coincide along the light surface. Then, we used a Dirichlet boundary condition for the inner boundary of the outer solution, this brought initially to non-regular global solutions (see §3.3). Such solutions are mathematically correct for the inner and outer part, however, they are physically not correct, since they do not satisfy the regularity condition along the light surface. We have run different parameters set, with different rotation laws, till we found the *proper* Dirichlet boundary

condition (obviously depending from the inner solution) that provided a consistent regular global solution (see §3.4), being characterized by a smooth transition of the field lines across the light surface. Such solution is unique for a certain choice of the rotation law $\Omega_F(\Psi)$.

Although in our computations the jet boundary $x_{\text{jet}}(z)$ is determined by the force-balance within the jet, and therefore subject to the regularity condition, with our results we do not prove the magnetohydrodynamic self-collimation process of the jet flow. The calculated jet magnetosphere is self-collimated in the sense that its structure has been determined only by the internal properties. To our understanding one may claim a self-collimation only, if the jet flow collimates *independently* from external forces. We do not treat internal forces that would provide the degree of collimation and in our force-free treatment we do not consider the interrelation with the medium outside the jet, therefore we cannot decide whether the flow is self-collimated or pressure collimated. However, the actual collimation process of the jet flow from an uncollimated conical outflow into a cylinder could only be investigated by time-dependent simulations taking into account the interaction with the ambient medium. Ouyed & Pudritz (1997) presented time-dependent simulations of the evolution of non-relativistic outflows from Keplerian accretion disks. Their results indeed prove the self-collimating property of axisymmetric MHD flows. They found that the gas collimates into cylinders parallel to the disk axis. The collimation of the outflow is due to the pinch force exerted by the dominant toroidal magnetic field generated by the outflow itself. The acceleration of the flow from the disk occurs by a centrifugal effect whereby, at some points along sufficiently inclined field lines, the centrifugal force dominates gravity and gas is flung away like *beads on a wire*. Therefore, a toroidal field component is created because the field lines foot points corotate with the disk. For a certain, already collimating, initial current-free ($\mathbf{J} = 0$) magnetic field distribution, a stationary state of the jet flow was obtained after about 400 Keplerian periods of the inner disk, with an increased degree of collimation. They assumed axisymmetry, a polytropic equation of state and ideal MHD.

It is well known that field lines must be closed. We like to underline that the jet model presented here implies field lines closing via jet bow-shocks, where the jet internal pressure equals the external interstellar/intergalactic medium pressure often showing radio lobes. The jet magnetic structure itself and the interstellar/intergalactic medium act as wires, the central source-disk system like a battery and radio lobes, which might also present hot spots, like a resistance.

3.2 Determination of the light surface

The numerical determination of the exact location of the light surface was the essential problem. Several months of computations were needed in order to solve it. Without knowing the exact location of the light surface no global solution can be obtained. In the following we discuss our approach in order to find the correct solution to such a

problem.

We use an iteration procedure to determine the location of the light surface. Since the rotation law $\Omega_{\text{F}}(\Psi)$ is prescribed, the (normalized) radius, x_{L} (see also § 2.4 for the normalizations), where the light surface, $D = 0$, intersects the jet boundary, $\Psi = 1$, is known,

$$x_{\text{L}}(\Psi = 1) = 1/\Omega_{\text{F}}(\Psi = 1). \quad (3.1)$$

However, the corresponding position in z -direction is not known.

The iteration procedure starts with the calculation of the inner solution with an outer grid boundary at $x = 1$ (for comparison, see Fig. 2.2). This choice is equivalent to the light cylinder in the case of rigid rotation. For *differential rotation* the radius $x = 1$ is defined as asymptotic light cylinder (for large z -values). For low z -values the boundary $x = 1$ is located inside the light surface $x_{\text{L}}(\Psi) = 1/\Omega_{\text{F}}(\Psi)$. Along this outer boundary (of the inner solution), we apply an homogeneous Neumann boundary condition. Usually, this implies that the field lines will cross that boundary perpendicular. However, in our case, if the boundary moves closer to the light surface, the homogeneous Neumann boundary condition transforms into the regularity condition (see § 2.4.1). The code takes implicitly into account the regularity condition. There are two reasons: 1) the Finite Element Code solves the *modified* GS equation and 2) the boundary integral, which is proportional to $D = 1 - x^2\Omega_{\text{F}}^2$, vanishes along the light surface. As a major result of this thesis, we have shown that the procedure of Fendt, Camenzind & Appl (1995) can be successfully extended for *differential rotation* $\Omega_{\text{F}}(\Psi)$ (Fendt & Memola 2001a).

With the GS solution of the first iteration step we estimate the deviation of the chosen outer boundary from the true light surface by calculating $D = 1 - x^2\Omega_{\text{F}}^2(\Psi)$. For the lowest z -value prescribed, we know that $D_{\text{max}} = 1 - x^2\Omega_{\text{F}}^2(\Psi = 1)$. Then, the outer grid boundary (x, z) is slowly moved to a larger radius with $\Delta x \sim D(x, z)^2$. The power of $D(x, z)$ is our choice. As a consequence of the different numerical grid, the field distribution will change. The value of D will, however, decrease. This procedure is repeated until D is below a certain limit, e.g. $D \leq 10^{-15}$. Having obtained the solution inside the light surface, this surface is the outer boundary for the inner solution and is taken as inner boundary for the outer solution.

3.3 Examples of a non-regular magnetic flux distribution

In this section we present two examples of field distributions that show kinks across the light surface (Figs. 3.2 and 3.3). The calculation was performed for two choices of the steepness parameter h of the iso-rotation Ω_{F} and for $g = 1$ (strength of the current term in the GS equation (2.21)): 1) $h = 0.2$, $g = 1$ and 2) $h = 0.5$, $g = 1$. The outer and inner solution illustrated in Fig. 3.1 for the $h = 0.2$ case, both satisfy the boundary conditions (the numerical Finite Element Code is converging). However, attaching

them in order to obtain a global (inner+outer) solution, such a field distribution shows kinks across the light surface (Fig. 3.2). In the same way, for the solution obtained with $h = 0.5$, as visible in Fig. 3.3. Therefore, such inner and outer solutions do not satisfy the boundary conditions for the other part, that means e.g. the outer solution as obtained does not satisfy the disk boundary of the inner solution. No outer solution was found for those inner solutions that could provide a regular transition of the field lines across the light surface. We learn that, if the strength of the current term in the GS equation (2.21) is only unity ($g = 1$), the regularity condition can not be satisfied.

We see that, for both solutions ($h = 0.2$ and $h = 0.5$) the asymptotic regime of a cylindrically collimated jet is not even reached for $Z/R_0 = 5$, since the field lines do not cross the upper boundary perpendicular. The parameters involved in the calculation are listed in Table 3.1. The outer disk (normalized) radius is $x_{\text{disk}} = 0.2$, the maximum light surface (normalized) radius is x_{max} and its height is $z(x_{\text{max}}) = 0.9$ in both cases. In particular, if $h = 0.2$ (solution NR1), $x_{\text{max}} = 1.29$ and the asymptotic jet (normalized) radius is $x_{\text{jet}} = 3.53$; if $h = 0.5$ (solution NR2) we calculate $x_{\text{max}} = 1.68$ and $x_{\text{jet}} = 3.08$. In the examples presented the electric current is definitely too low, therefore the collimation is too weak. A larger value of the maximum z might help if the code would not be influenced by that in its delicate convergency process.

<i>NRS</i>	h	g	x_{disk}	x_{max}	$z(x_{\text{max}})$	x_{jet}
NR1	0.2	1.0	0.2	1.29	0.9	3.53
NR2	0.5	1.0	0.2	1.68	0.9	3.08

Table 3.1: Parameters used for the calculation of the non-regular global solutions (NRS): NR1 (see Fig. 3.2) and NR2 (see Fig. 3.3). Note that h is the steepness parameter of the iso-rotation Ω_{F} ; g is the coupling constant, that describes the strength of the current term in the GS equation (2.21); x_{disk} is the outer disk (normalized) radius; x_{max} is the maximum light surface (normalized) radius; $z(x_{\text{max}})$ is the height of x_{max} ; x_{jet} is the asymptotic jet (normalized) radius.

3.4 Global regular solutions in two dimensions

Now we present global regular solutions. We performed calculations for different opening angles, different strength of the poloidal electric current g , and different steep-

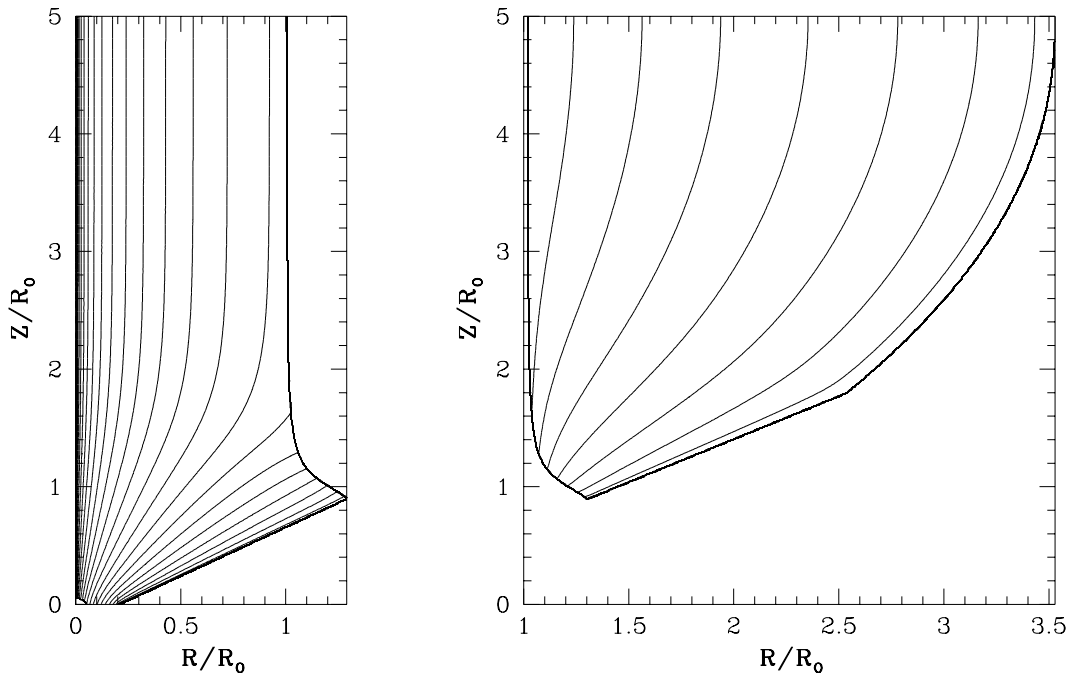


Figure 3.1: Two-dimensional magnetic flux distribution $\Psi(x, z)$: for $h = 0.2$, $g = 1.0$. *Left*: inner solution. *Right*: outer solution. Attaching these inner and outer solutions along the light surface we obtain Fig. 3.2. The iso-contours of $\Psi(x, z)$, equivalent to poloidal field lines, have contour levels $\Psi_n = 10^{-(0.1n)^2}$, $n = 0, \dots, 25$. Note that due to the choice of contour levels the iso-contour density does not mirror the field strength.

ness parameters h , in order to find the unique two-dimensional solution that, for a certain rotation law, provides a smooth transition of the field lines across the light surface. We found global regular solutions for two values of the steepness parameter and current strength, $h = 0.2$, $g = 2.5$ (see Fig. 3.4 and Fig. 3.5), and $h = 0.5$, $g = 2.0$ (see Fig. 3.7 and Fig. 3.8). The main difference to the previous non-regular solutions is that we increase the strength of the electric current, that is equivalent to the toroidal magnetic field (see Eqs. 2.9 and 2.21). An increase of the electric current basically increases the degree of collimation of the jet.

The asymptotic regime is reached already for $Z/R_0 = 3$. This is the region where the field lines are already collimated to a cylinder. The parameters involved in the calculation are listed in Table 3.2. The outer disk (normalized) radius is $x_{\text{disk}} = 0.2$, as for the non-regular solutions (NR1 and NR2). For the R1 solution we have $h = 0.2$, $g = 2.5$, $x_{\text{max}} = 1.12$, $z(x_{\text{max}}) = 0.4$, and $x_{\text{jet}} = 2.14$. For the R2 solution the parameters are $h = 0.5$, $g = 2.0$, $x_{\text{max}} = 1.36$, $z(x_{\text{max}}) = 0.55$, and $x_{\text{jet}} = 2.23$.

Again we remark that the key parameter for the regular solutions is the strength of the current term, g . The steeper profile for the rotation law implies a smaller asymptotic jet radius (Fendt 1997b), however a larger poloidal electric current can balance the effect of *differential rotation*. Therefore, the $h = 0.2$ solution (with $g = 2.5$) collimates to a smaller asymptotic jet radius than the $h = 0.5$ solution (with $g = 2.0$), as can be

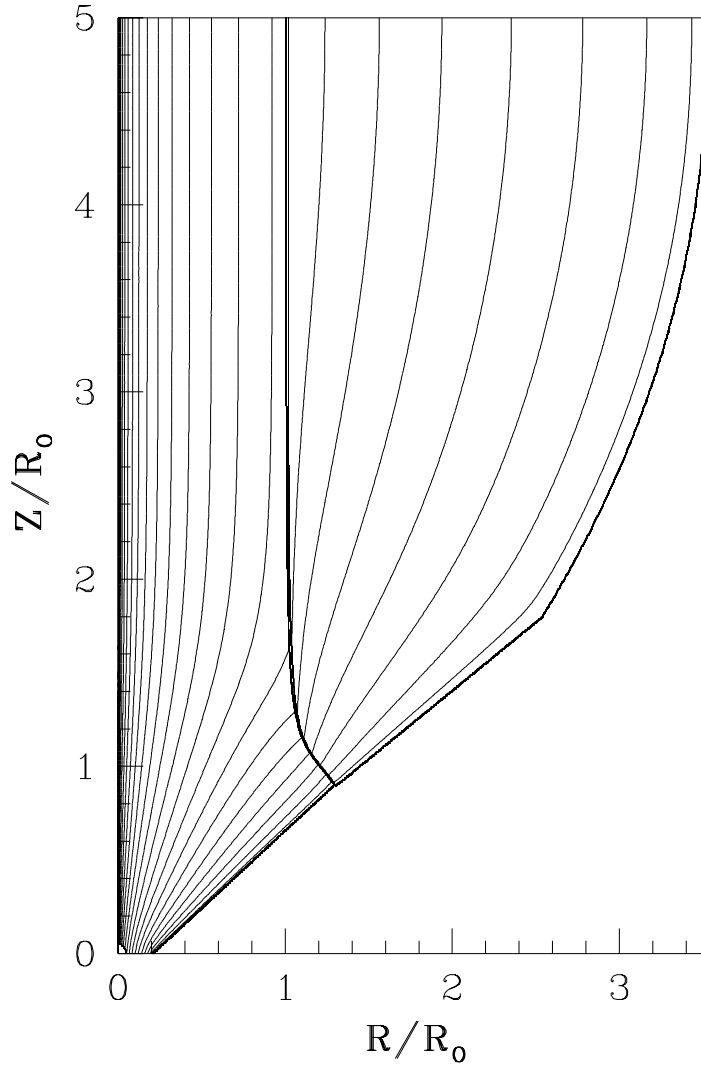


Figure 3.2: Two-dimensional magnetic flux distribution $\Psi(x, z)$: non-regular global jet solution for $h = 0.2$, $g = 1.0$ (see Table 3.1, solution NR1). The iso-contours of $\Psi(x, z)$, equivalent to poloidal field lines, have contour levels $\Psi_n = 10^{-(0.1n)^2}$, $n = 0, \dots, 25$. Note that due to the choice of contour levels the iso-contour density does not mirror the field strength.

seen in Fig. 3.5 and Fig. 3.8. A $h = 0.2$ solution with $g = 2.0$ would have a jet radius of 2.4. The second solution with the steeper profile of the rotation law $\Omega_{\text{F}}(\Psi)$ would better fit to a Keplerian disk rotation. A perfect match would require an even steeper $\Omega_{\text{F}}(\Psi)$ -profile, unfortunately it was not possible to reach convergency for $h = 0.9$.

Note that the mean half opening angle of the jet magnetospheres is about 60° , which satisfies the Blandford & Payne (1982) condition to obtain a centrifugally driven outflow from the disk (see §1.2).

As already discussed, the shape of the outermost flux surface ($\Psi = 1$) is not prescribed

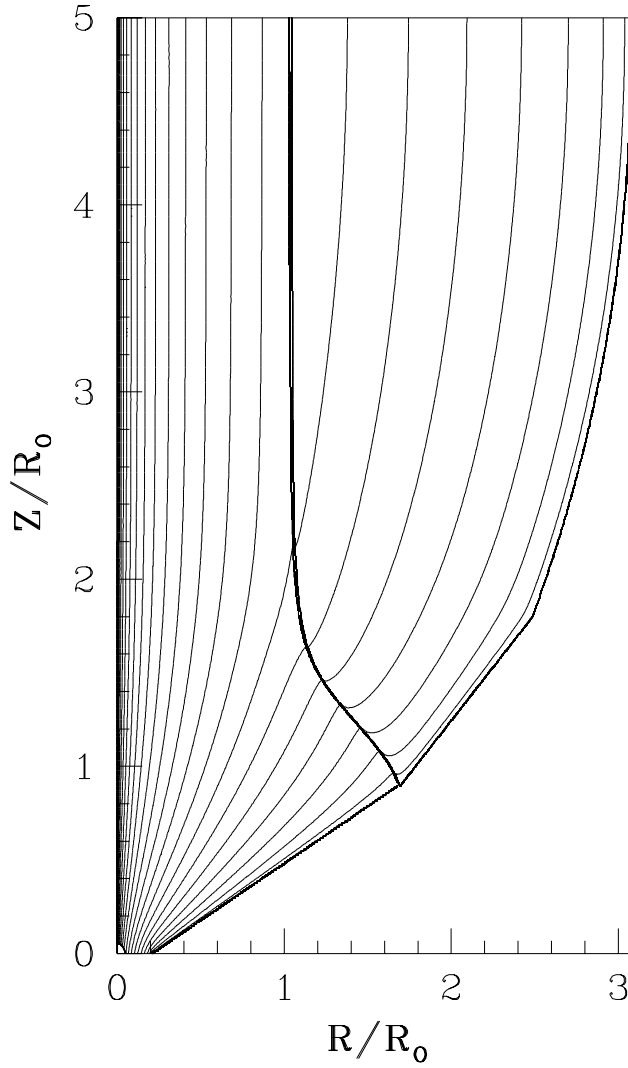


Figure 3.3: Two-dimensional magnetic flux distribution $\Psi(x, z)$: non-regular global jet solution for $h = 0.5$, $g = 1.0$ (see Table 3.1, solution NR2). The iso-contours of $\Psi(x, z)$, equivalent to poloidal field lines, have contour levels $\Psi_n = 10^{-(0.1n)^2}$, $n = 0, \dots, 25$. Note that due to the choice of contour levels the iso-contour density does not mirror the field strength.

but is a result of our calculation eventually determined by the regularity condition. After crossing the light surface the jets collimate to their asymptotic radius within a distance from the source of about $1 - 2 R_0$ along the jet-axis. The opening angle of the second solution is smaller, however, the jet collimation is achieved only at a larger distance from the central source. In our examples, the *jet expansion rate*, which we define as the ratio of the asymptotic jet radius to the foot point jet radius (the *disk radius*), is about 10. The true scaling of the jet magnetosphere in terms of the size of the central object can be determined by connecting the jet iso-rotation parameter $\Omega_F(\Psi)$ to the disk rotation (see §3.5).

RS	h	g	x_{disk}	x_{max}	$z(x_{\text{max}})$	x_{jet}
R1	0.2	2.5	0.2	1.12	0.40	2.14
R2	0.5	2.0	0.2	1.36	0.55	2.23

Table 3.2: Parameters used for the calculation of the regular global solutions (RS): R1 (see Fig. 3.5) and NR2 (see Figs. 3.8 and 3.9). Note that h is the steepness parameter of the iso-rotation Ω_{F} ; g is the coupling constant, that describes the strength of the current term in the GS equation (2.21); x_{disk} is the outer disk (normalized) radius; x_{max} is the maximum light surface (normalized) radius; $z(x_{\text{max}})$ is the height of x_{max} ; x_{jet} is the asymptotic jet (normalized) radius.

The calculated jet magnetosphere is self-collimated in the sense that its structure has been determined only by the internal properties. We do not prove the magnetohydrodynamic *self-collimation process* of the jet flow (see §3.1).

In all calculations the regime of the central source is more or less circular and its (normalized) radius is $x_{\star} = 0.05$, that means 5% of the asymptotic light cylinder radius value. In Fig. 3.6 we present an enlargement of the inner region for the case $h = 0.2$. We assume that the central black hole is somewhere inside the region of radius 0.05.

Finally we show the whole bipolar outflow two-dimensional magnetic structure, originating from the accretion disk surrounding the central object, by mirroring the axisymmetric, two-dimensional, regular, global solution obtained for $h = 0.5$ (see Fig. 3.8) respect to the jet-axis and to the equatorial plane and rotating it by 90° (see Fig. 3.9).

3.5 Scaling of the jet-disk system

Having obtained a global two-dimensional magnetic field structure of the collimating region of the jet from the disk to the asymptotic regime, we are now able to achieve a direct scaling of the jet magnetosphere in terms of the size of the central object. This idea is simply based on the assumption that the foot points of the field lines are rotating with Keplerian speed, $\Omega_{\text{F}}(x(\Psi)) = \Omega_{\text{K}}(x)$ and to the fact that in ideal MHD the iso-rotation parameter $\Omega_{\text{F}}(\Psi)$ is conserved along the field lines. It is therefore possible to construct a self-consistent model of the whole *star-disk-jet* system with only a small

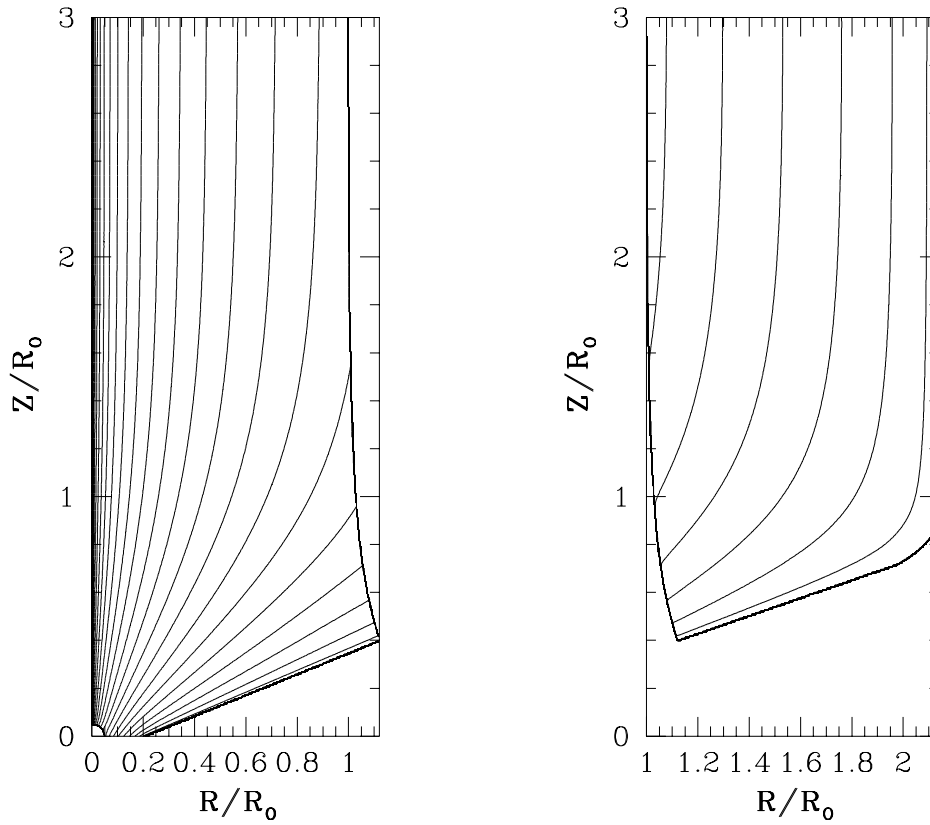


Figure 3.4: Two-dimensional magnetic flux distribution $\Psi(x, z)$ for $h = 0.2$, $g = 2.5$. *Left:* Inner solution. *Right:* Outer solution. Attaching these inner and outer solutions along the light surface we obtain Fig. 3.5. The iso-contours of $\Psi(x, z)$, equivalent to poloidal field lines, have contour levels $\Psi_n = 10^{-(0.1n)^2}$, $n = 0, \dots, 25$. Note that due to the choice of contour levels the iso-contour density does not mirror the field strength.

set of free parameters. In the following we will motivate such a model.

First, we demonstrate how the connection between the asymptotic jet and the disk, applied for our very special model assumption, provides a specific estimate for the asymptotic light cylinder radius R_0 . Normalizing the Keplerian velocity Ω_K in the same way as Ω_F (see §2.4), we obtain the expression:

$$R_0 = \frac{GM}{c^2 \Omega_K^2} \frac{1}{x^3} = \frac{GM/c^2}{\Omega_F^2(\Psi = 1) x_{\text{disk}}^3} = \frac{0.5 R_S}{\Omega_F^2(\Psi = 1) x_{\text{disk}}^3}. \quad (3.2)$$

If we then fix the iso-rotation parameter $\Omega_F(\Psi)$ and the disk radius x_{disk} by our model, we see that the asymptotic light cylinder is proportional to the mass of the central object! For $\Omega_F^2(1) = 0.54$ (which refers to the $h = 0.5$ model) and $x_{\text{disk}} = 0.2$ the asymptotic light cylinder is $R_0 = 116 R_S$, which is about 2 times larger compared to the jet solution with a rigid rotation $\Omega_F \equiv 1$ and will increase for larger values of h .

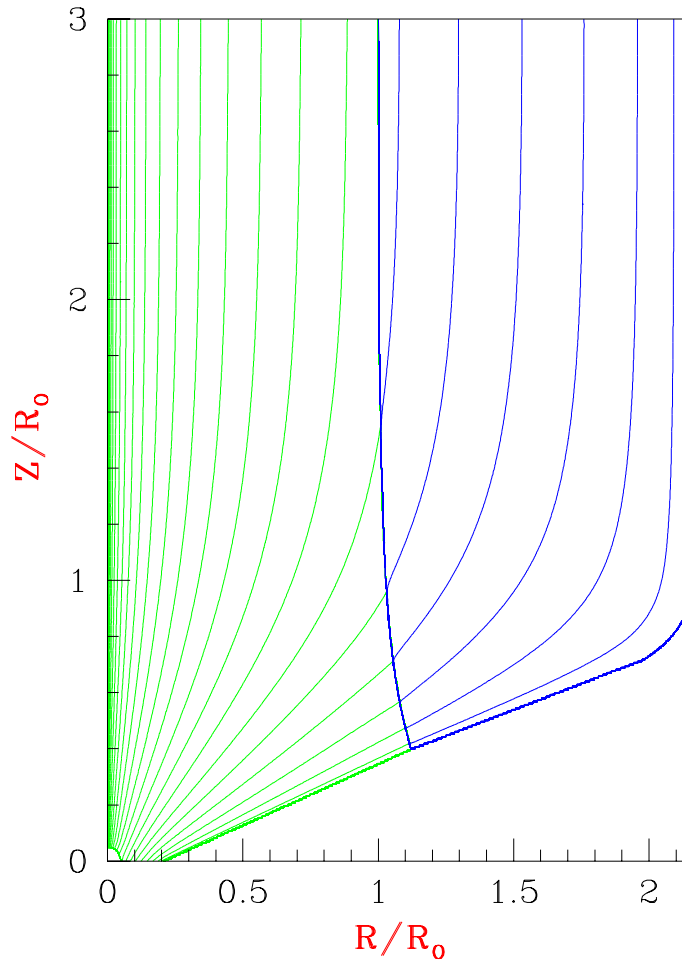


Figure 3.5: Two-dimensional magnetic flux distribution $\Psi(x, z)$: regular global jet solution for $h = 0.2$, $g = 2.5$ (see Table 3.2, solution R1; Fendt & Memola 2001a). *Green*: inner solution. *Blue*: outer solution. The iso-contours of $\Psi(x, z)$, equivalent to poloidal field lines, have contour levels $\Psi_n = 10^{-(0.1n)^2}$, $n = 0, \dots, 25$. Note that due to the choice of contour levels the iso-contour density does not mirror the field strength.

With the choice of g , the value of R_0 constrains the maximum poloidal magnetic flux and electric current. Here, no assumption is made about the flux distribution along the disk.

At this point, we are able to determine the disk magnetic flux distribution $\Psi(x)$ combining the asymptotic jet rotation law $\Omega_F(\Psi)$ with a Keplerian disk rotation $\Omega_K(x)$. From Eq. (3.2) it follows that $\Omega_F(\Psi)/\Omega_F(1) = \Omega_K(x)/\Omega_F(\Psi = 1) = (x/x_{\text{disk}})^{-3/2}$. In combination with the numerically derived $\Omega_F(\Psi)$ this gives the magnetic flux distribution $\Psi(x)$ along the disk (Fig. 3.10). The figure shows that the disk flux distribution derived from the asymptotic jet is distributed only over the outer part of the disk. This can be interpreted in two ways. First, it may imply a relatively large inner disk radius and, thus, an asymptotic jet radius small in terms of radii of the central object. Sec-

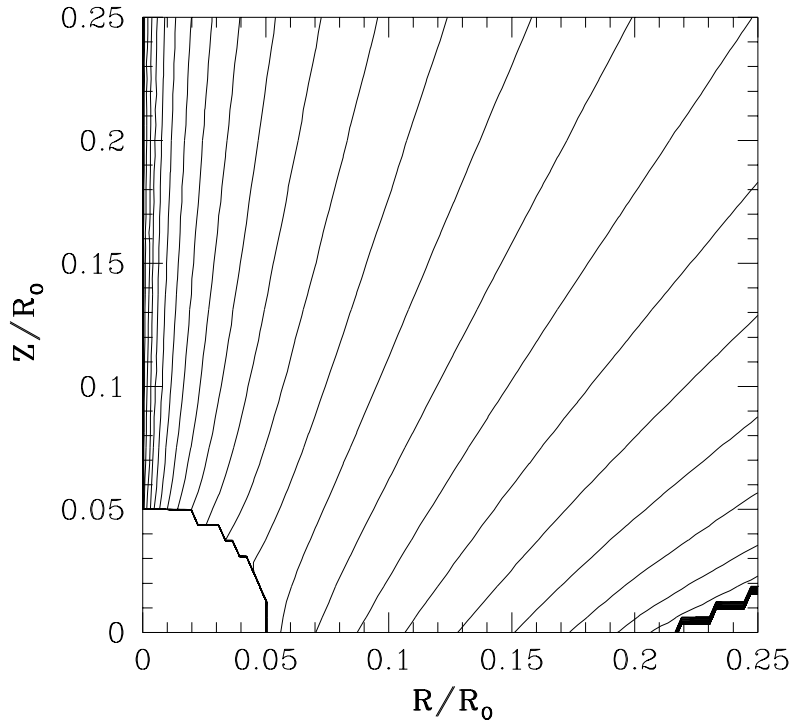


Figure 3.6: Two-dimensional magnetic flux distribution $\Psi(x, z)$: enlargement of the inner region for the case $h = 0.2$, $g = 2.5$. The iso-contours of $\Psi(x, z)$, equivalent to poloidal field lines, have contour levels $\Psi_n = 10^{-(0.1n)^2}$, $n = 0, \dots, 25$. Note that due to the choice of contour levels the iso-contour density does not mirror the field strength.

only, it just underlines the fact that in our model the distribution of the asymptotic jet iso-rotation parameter is too flat in order to be truly connected to a disk magnetic flux with an extended radial distribution. For a model taking into account the disk Keplerian rotation in a fully self-consistent way, the magnetic flux distribution which has to be used as disk boundary condition for the GS solution is the one shown in Fig. 3.10.

On the other hand, the assumption of a Keplerian disk rotation together with a certain disk magnetic flux distribution provides an expression for the iso-rotation parameter $\Omega_F(\Psi) = \Omega_K(x(\Psi)) = \Omega_K(\Psi)$. In fact, from the disk magnetic flux distribution (2.23) we derive $x(\Psi) = a(e^{b\Psi} - 1)^{1/2}$, then, from Eq. (3.2) it follows:

$$\Omega_K^2(\Psi) = \frac{GM}{R_0 c^2} \frac{1}{a^3 (e^{b\Psi} - 1)^{3/2}} = \frac{x_{\text{disk}}^3 \Omega_F^2(\Psi = 1)}{a^3 (e^{b\Psi} - 1)^{3/2}}. \quad (3.3)$$

From Eq. (3.3) and $b = \ln(1 + (x_{\text{disk}}/a)^2)$ (see § 2.5.2) one finds:

$$\frac{\Omega_K(\Psi)}{\Omega_F(1)} = \left(\frac{x_{\text{disk}}}{a}\right)^{3/2} \left(\left(1 + \left(\frac{x_{\text{disk}}}{a}\right)^2\right)^\Psi - 1 \right)^{-3/4}. \quad (3.4)$$

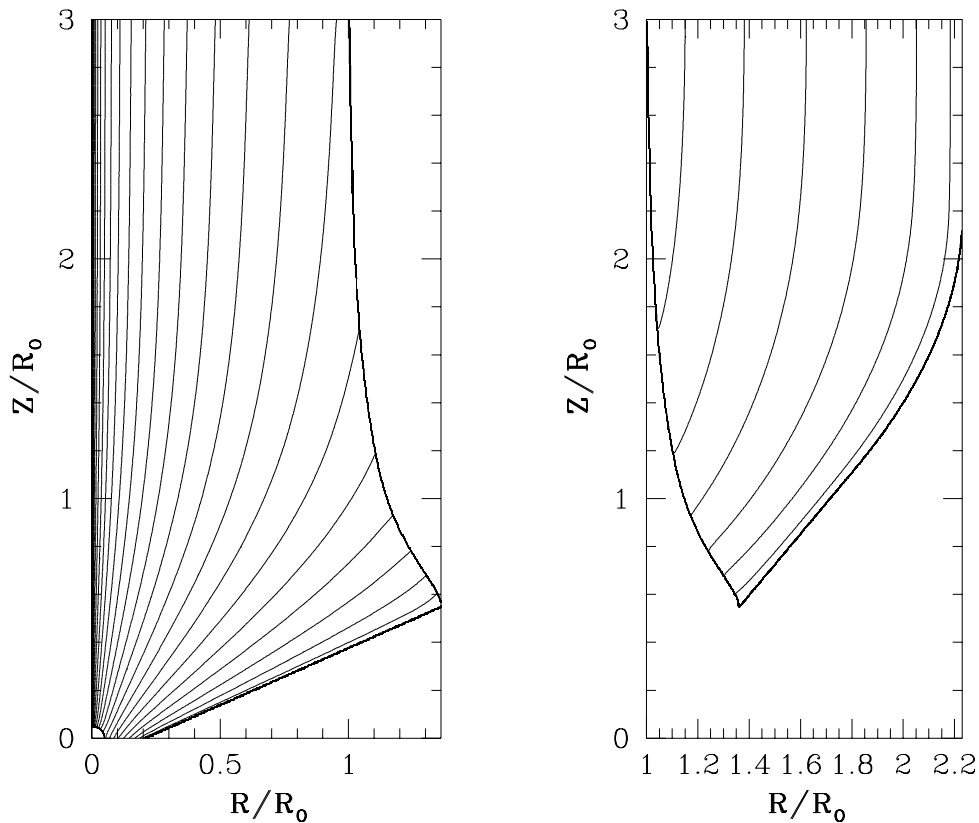


Figure 3.7: Two-dimensional magnetic flux distribution $\Psi(x, z)$ for $h = 0.5$, $g = 2.0$ (Memola & Fendt 2001). *Left*: Inner solution. *Right*: Outer solution. Attaching these inner and outer solutions along the light surface we obtain Fig. 3.8. The iso-contours of $\Psi(x, z)$, equivalent to poloidal field lines, have contour levels $\Psi_n = 10^{-(0.1n)^2}$, $n = 0, \dots, 25$. Note that due to the choice of contour levels the iso-contour density does not mirror the field strength.

This function is definitely steeper compared to the $\Omega_F(\Psi)$ -distributions that have been derived in Fendt (1997b) and are used here. This is a limitation of our ansatz. A steeper profile for the rotation law is not yet possible to treat with our code due to the lack of numerical resolution. The non-linear character of the GS equation becomes stronger due to the gradients in the Ω_F -source term.

In summary, only a model including *differential rotation* $\Omega_F(\Psi)$ may provide a connection between the asymptotic jet, the disk magnetic flux distribution and also the size of the central object. With our model we have presented a reasonable first solution for a self-consistent treatment.

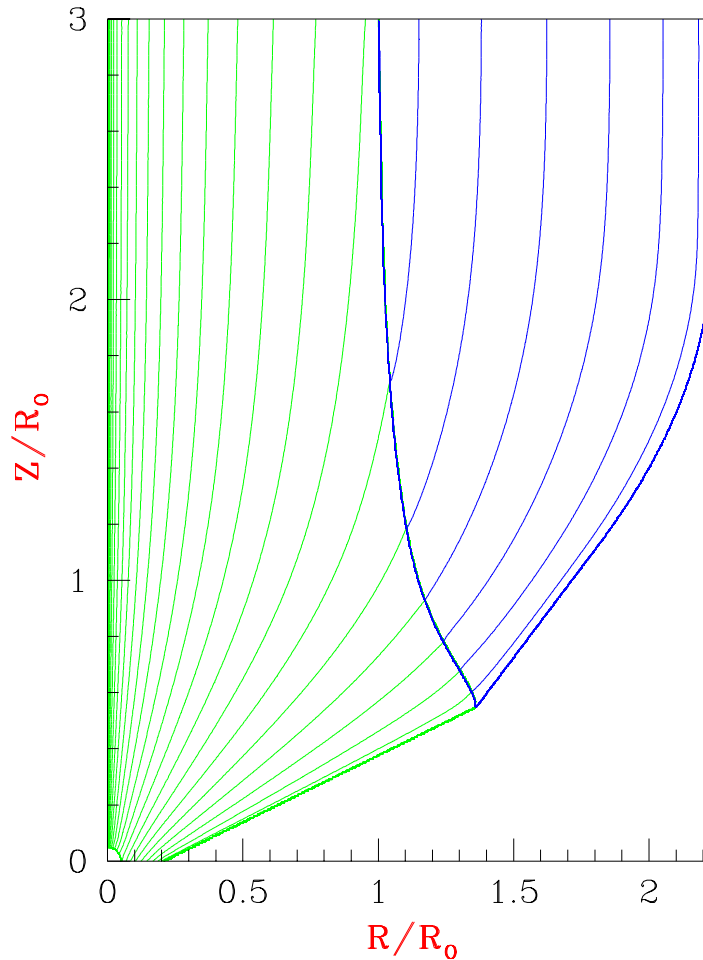


Figure 3.8: Two-dimensional magnetic flux distribution $\Psi(x, z)$: regular global jet solution for $h = 0.5$ (see Table 3.2, solution R2; Fendt & Memola 2001a). *Green*: inner solution. *Blue*: outer solution. The iso-contours of $\Psi(x, z)$, equivalent to poloidal field lines, have contour levels $\Psi_n = 10^{-(0.1n)^2}$, $n = 0, \dots, 25$. Note that due to the choice of contour levels the iso-contour density does not mirror the field strength.

3.6 Magnetic angular momentum loss and disk toroidal field

Jets can efficiently remove angular momentum. The magnetic angular momentum loss in the disk due to the jet drives the accretion process beside turbulence.

The jet magnetic field structure is governed by the choice of the functions $I(\Psi)$ and $\Omega_F(\Psi)$, here taken from an asymptotic solution. In combination with the disk magnetic flux distribution in Eq. (2.23) we can determine two parameters interesting for the jet-disk interaction. These are: 1) the magnetic angular momentum loss per unit time and unit radius from the disk into the jet, which gives us the magnetic angular momentum flow from each surface element along the disk, that shows where from the

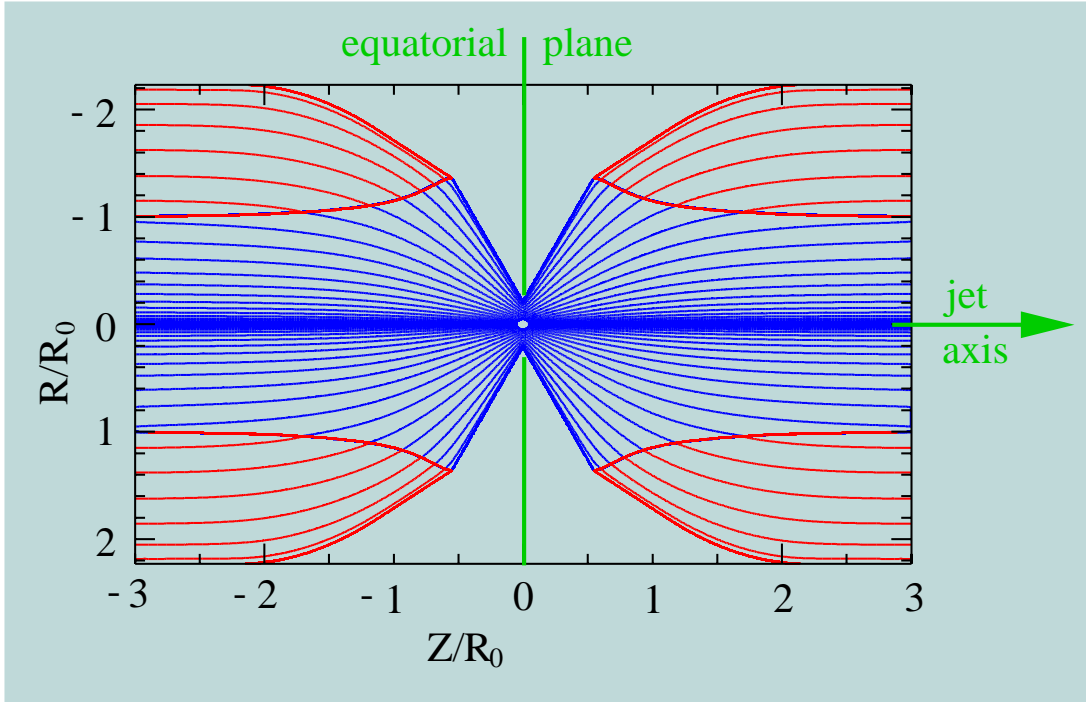


Figure 3.9: Two-dimensional magnetic flux distribution $\Psi(x, z)$: whole jet magnetic structure for $h = 0.5$, $g = 2.0$. *Blue*: inner solution. *Red*: outer solution. This figure has been obtained by mirroring the axisymmetric two-dimensional solution in Fig. 3.8 respect to the jet-axis and to the equatorial plane and then rotating it by 90° . Note that due to the choice of contour levels the iso-contour density does not mirror the field strength.

disk the magnetic angular momentum is extracted, and 2) the toroidal magnetic field distribution along the disk. With $I(\Psi)$ as the angular momentum flux per unit time per unit flux tube, the (normalized) angular momentum flux per unit time per unit radius is $d\dot{J}/dx = -xB_z I(x)$ along the disk. Figures 3.11 and 3.13 show the behaviour of both quantities for our jet model with the steeper profile of the rotation law, $h = 0.5$. Most of the magnetic angular momentum is lost in the outer parts of the disk (Fig. 3.11). The toroidal field distribution, $B_\phi(x) = -\frac{2I(x)}{cR}$ along the disk has a maximum at about half the disk radius (Fig. 3.13). This may have interesting applications for accretion disk models taking into account a magnetized wind as a boundary condition. The magnetic angular momentum loss is determined by the normalization,

$$\dot{J} = -(I_{\max}\Psi_{\max}/c) \int I(\Psi)d\Psi \quad \text{or} \quad \dot{J} = -(\sqrt{g}\Psi_{\max}/2R_0) \int I(\Psi)d\Psi, \quad (3.5)$$

where \dot{J} is the integrated angular momentum flow in the jet at the disk surface, whose dependency from $x(\Psi)$ is shown in Fig. 3.12.

Clearly, the exact distribution of these quantities is biased by the magnetic flux disk

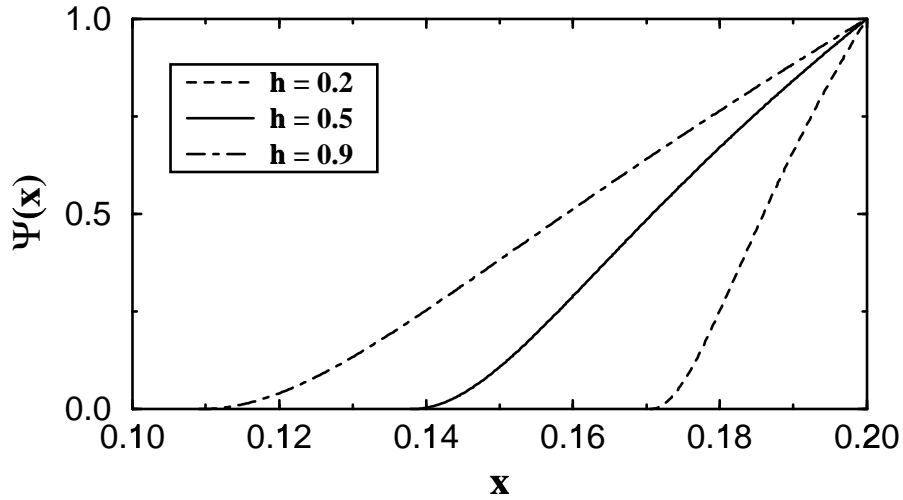


Figure 3.10: Magnetic flux distribution $\Psi(x)$ along the disk surface as determined from the asymptotic jet properties and the Keplerian rotation of the disk (Fendt & Memola 2001a). In a model that takes into account the disk Keplerian rotation in a fully self-consistent way, such a magnetic flux distribution should be used as disk boundary condition in order to solve the GS equation (2.20).

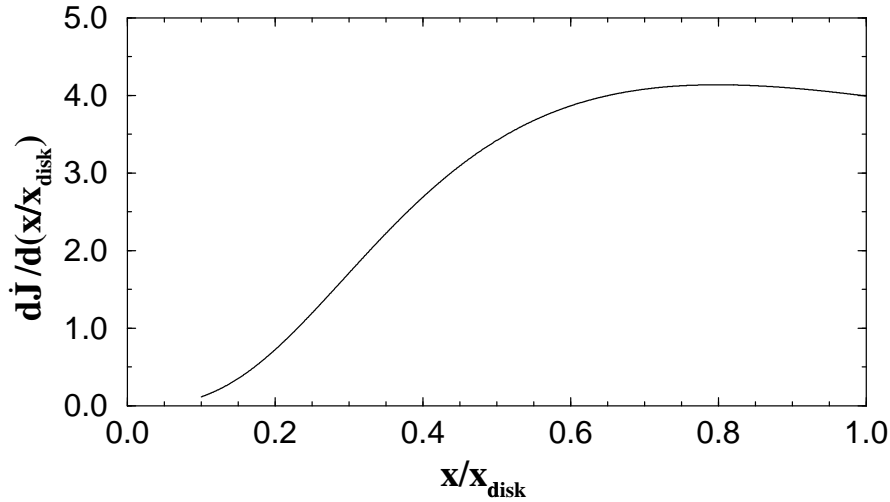


Figure 3.11: Magnetic angular momentum loss per unit time per unit radius $d\dot{J}/dx$ at radius x for the jet solution with $h = 0.5$, shown in Fig. 3.8.

boundary condition of our model in Eq. (2.23). However, we believe that the main features are rather general and valid for any poloidal current and magnetic flux distribution with the typical core-envelope structure.

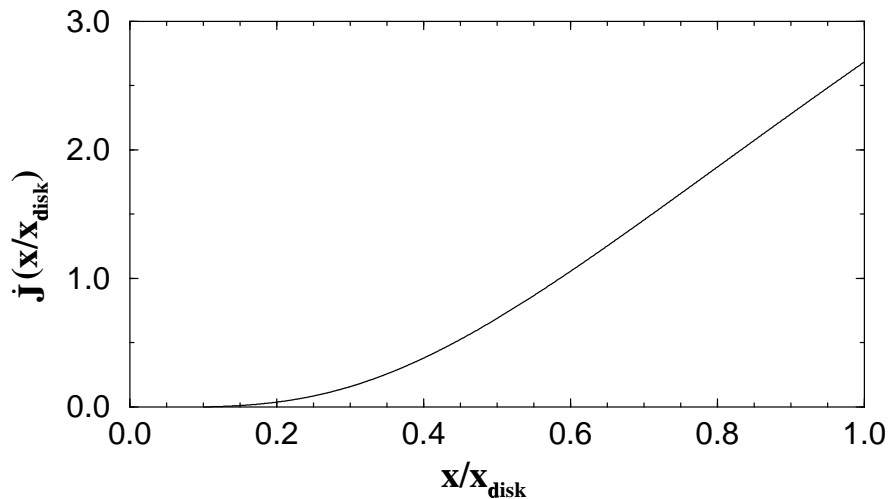


Figure 3.12: Integrated angular momentum flow in the jet at the disk surface, $\dot{J}(x)$, for the jet solution with $h = 0.5$, shown in Fig. 3.8.

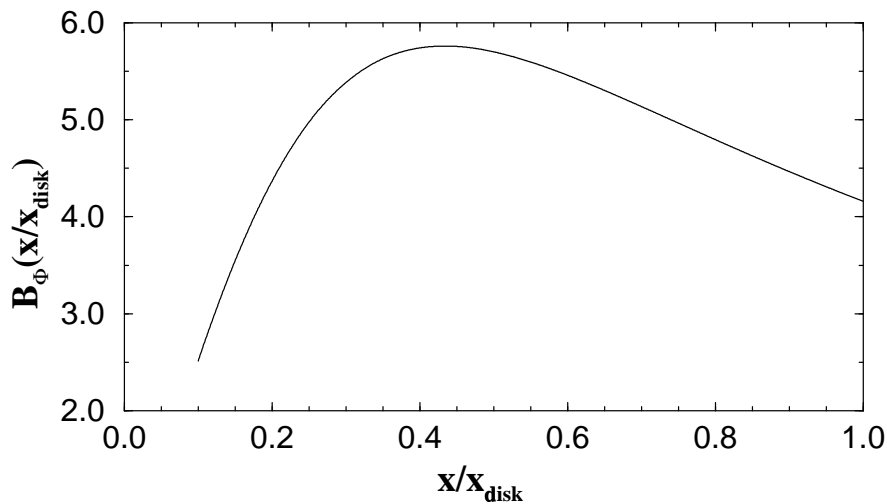


Figure 3.13: Toroidal field distribution $B_\phi(x)$ for the jet solution with $h = 0.5$, shown in Fig. 3.8.

3.7 Comparison with observations

The jet of M87 shows superluminal motion clearly indicating a highly relativistic jet velocity (Biretta, Sparks & Macchetto 1999). Recent radio observations have been able to resolve the innermost part of the M87 jet formation region with 0.33×0.12 mas beam resolution (Junor, Biretta & Livio 1999), corresponding to $2.5 - 7.0 \times 10^{16}$ cm. Assuming a central supermassive black hole of $3 \times 10^9 M_\odot$ (Ford et al. 1994), this is equivalent to about $30 R_S$.

Junor, Biretta & Livio (1999) derived that the jet full opening angle is 60° up to a distance of 0.04 pc from the source with a *strong collimation* occurring afterwards.

We now apply our two-dimensional jet model to these observations and compare the geometrical scales. Such a comparison is not possible for e.g. self-similar models. From the observed radio profile resolving the inner M87 jet (see Fig. 1 in Junor, Biretta & Livio 1999), we deduce a jet radius of about 120 Schwarzschild radii. With this, the first important conclusion is that the ratio of jet radius to light cylinder radius must be definitely less than the value of 100 which is usually assumed in the literature. A number value of 3–10 seems to be much more likely. Numerical models of two-dimensional general relativistic magnetic jets fitting in this picture were calculated by Fendt (1997a). These solutions, however, do not take into account the differential rotation $\Omega_F(\Psi)$.

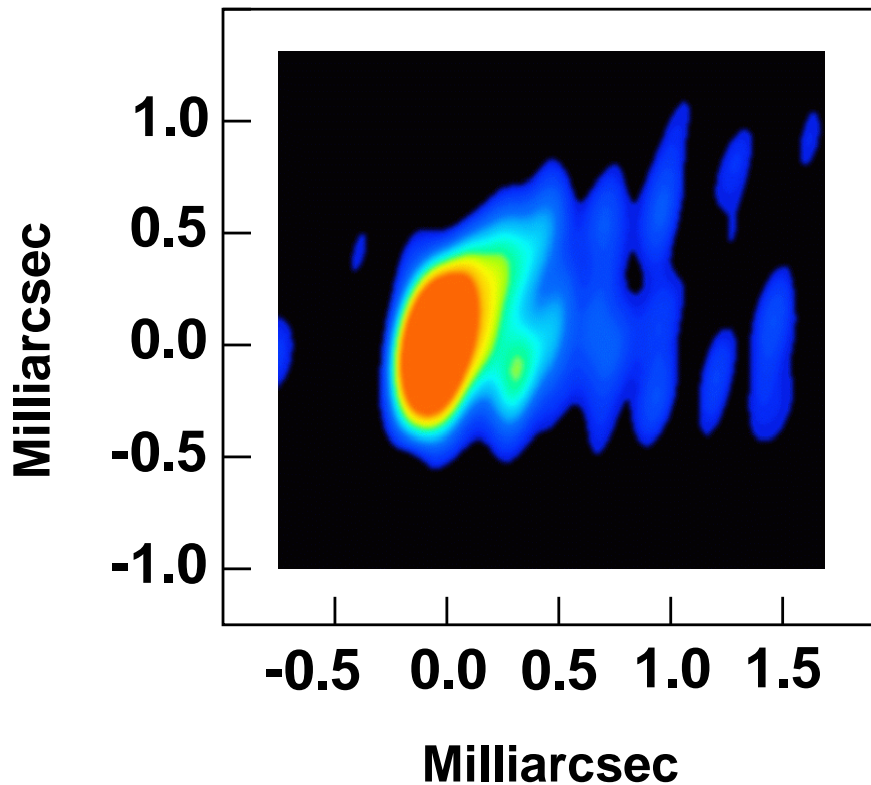


Figure 3.14: Nucleus of M87 at 43 GHz (Junor, Biretta & Livio 1999).

Junor, Biretta & Livio (1999) claim that the M87 jet radius in the region where the jet is first formed cannot be larger than their resolution of $30 R_S$. Our conclusion is that the expansion rate is limited in both directions. The new radio observations give a minimum value of 3. Since the jet mass flow must originate outside the marginally stable orbit which is located at $3 - 6 R_S$, theoretical arguments limit the expansion rate to the value of about 20. Clearly, if the jet radius is really as small as observed in M87, general relativistic effects may vary the field structure in the jet formation region.

By comparing the M87 jet radius deduced above ($\sim 120 R_S$) with our model solutions

(see Table 3.2), we derive an asymptotic light cylinder radius of the M87 jet of about $50 R_S$. The value obtained from Eq. 3.2 differs from that by a factor of two, but is biased by the unknown size of the disk radius x_{disk} . This parameter, however, does not affect the global solution. Note that in relativistic MHD theory, nothing special is happening at the light cylinder. For a highly magnetized plasma wind the light surface corresponds to the usual Alfvén surface which itself does not affect the flow of matter. Ergo, the light cylinder is un-observable.

Also the opening angle in our numerical solution is larger than the observed value by a factor of two. This cannot be due to projection effects since any inclination between jet-axis and the line-of-sight will increase the observed opening angle. We hypothesize that a numerical model with a steeper profile for the iso-rotation parameter would give a smaller jet opening angle comparable to the observed data. This is not surprising, since the jet footpoint anchored in a Keplerian disk rotates faster than in our model. Nevertheless, comparing the collimation distance observed in the M87 jet and assuming a similar ratio of jet radius to light cylinder radius as in our model with $h = 0.5$, we find good agreement. The collimation distance is $2R_0$.

In summary, we conclude that the example of the M87 jet gives clear indication that the light cylinder of AGN jets might not be as large as previously thought. Although our model does not fit the observed geometrical properties of the inner M87 jet perfectly, we find in general a close compatibility.

The importance of the theoretical investigation of the jet collimation region lies also into the fact that this is the only way to get information about the region very close to the central object. In fact, the M87 example is unique for the combination of a *close* object and a supermassive black hole of $3 \times 10^9 M_\odot$. Considering the quasar 3C 273 at a distance of about 600 Mpc we calculate an angular size of the jet collimation region around 10^{-6} arcsec, which is still un-resolvable. In fact, the space VLBI-VSOP has a spatial resolution of tens of microarcseconds. In order to reach a resolution of 10^{-6} arcsec we need an antenna on the Moon!

Chapter 4

X-ray emission of MHD jets from stellar mass black holes

4.1 The model

X-rays from jets probe the sites of the most energetic particles and the most dramatic acceleration mechanisms. The jet provides the energetical link between the disk and the hard X-ray source.

Under the assumptions of axisymmetry, stationarity and infinite conductivity, the MHD equations reduce to the *Grad-Shafranov equation*, which determines the field structure as discussed in Chapter 2 and Chapter 3 and to the *wind (or Bernoulli) equation* which describes the flow dynamics along the field (e.g. Camenzind 1986, 1987; see also § 4.2). The solution of the MHD wind equation allows for the calculation of the physical parameters of the flow (densities, velocities, temperatures of *each* volume element), which can be used to investigate its spectral properties.

Here, we calculate the thermal spectrum of an optically thin jet flow taking into account one of the solutions of Fendt & Greiner (2001) and considering relativistic Doppler shifting and boosting as well as different inclinations of the jet-axis to the line-of-sight. A similar approach was undertaken by Brinkmann & Kawai (2000) who have been modeling the two dimensional hydrodynamic outflow of SS 433 applying various initial conditions. However, they do not consider relativistic effects such as Doppler boosting in their spectra.

The model geometry consists of nested collimating magnetic surfaces. We have, then, for every magnetic surface a sheet of matter accelerating along a collimating cone. The cross section of each sheet becomes larger for larger distances from the origin of the jet. Our approach is the following:

- **The MHD wind solution**

The numerical calculation of the magnetohydrodynamic parameters of a collimating accelerating wind from the close environment of a rotating black hole, as presented by Fendt & Greiner (2001), is the starting point to obtain the X-ray spectra of the inner jet of stellar mass black holes. Prescribing the mass flow rate \dot{M}_{jet} together with the shape of the collimating field lines $z(x)$, these solutions give a unique set of parameters of the flow defined by the regularity condition across the magnetosonic points¹. We choose a solution (noted as S3 in Fendt & Greiner 2001), where $\dot{M}_{\text{jet}} = 10^{-10} M_{\odot}/\text{yr}$ and $z(x) = 0.1(x - x_0)^{6/5}$, x being the normalized cylindrical radius, x_0 the foot point of the field line at the equatorial plane, and z the height above the disk.

The length scales are normalized to the gravitational radius, $r_g = 7.4 \times 10^5 \text{ cm}$ ($M/5 M_{\odot}$). A temperature range $T = 10^{6.62} - 10^9 \text{ K}$ defines the inner part of the wind solution (from $12.7r_g$ till $500r_g$). Our volume distribution involves 5000 volume elements along the jet and 63 in ϕ direction defining an axisymmetric torus (i.e. 5000 tori along the magnetic surface), all together forming a conical sheet.

- **Calculation of the innermost jet rest-frame X-ray emission**

Assuming an optically thin plasma, the calculation of thermal X-ray spectra of the volume elements (in their rest frame) of the innermost jet, defined by the wind solution, has been performed (Brinkmann 2001). Fendt & Greiner (2001) obtained temperatures up to 10^{12} K and mentioned the possibility of X-ray emission. The higher temperatures refer to the intermediate region between disk and jet. Such high temperatures are to a certain degree caused by the use of a non-relativistic equation of state. Employing a relativistically correct equation of state (Synge 1957) one would expect gas temperatures an order of magnitude lower (Brinkmann 1980).

The injection radius, R_i , which is, in fact, the boundary condition for the jet flow, is located at a height above the disk of $0.74r_g$. It is $R_i = 8.3r_g \simeq 6 \times 10^6 \text{ cm}$ ($M/5 M_{\odot}$), where, for the chosen MHD solution, the injection temperature is $T_i = 10^{10.2} \text{ K}$. The inner jet half opening angle at the injection radius is of 80.4 degrees, which respects the Blandford & Payne (1982) condition for allowing a centrifugally driven outflow of matter from the disk (see § 1.2).

We (again) are interested in a tiny region, due to the X-ray temperatures, of diameter $2.5 \times 10^{-5} \text{ AU}$, which extends till 85 Schwarzschild radii in z direction ($R_S = 2GM_{\text{BH}}/c^2 = 1.48 \times 10^6 \text{ cm}$), that means $8.4 \times 10^{-6} \text{ AU}$. Microquasar jets extend up to a few $6 \times 10^4 \text{ AU}$ in z , therefore we are investigating the innermost region of a stellar mass black hole/neutron star jet. Assuming a microquasar at a distance of 10 kpc, the inner region of the jet has an angular size of $0.82 \times$

¹The wind equation has three singular points (the slow magnetosonic point, the fast magnetosonic point, the Alfvén point), where the velocity of the wind flow equals the speed of the magnetosonic waves.

10^{-9} arcsec, while the maximum radius of this region is 3.70×10^8 cm, which corresponds to an angular size of about 2.06×10^{-9} arcsec.

- **Doppler shifting and boosting of the rest-frame X-ray emission**

Considering the relativistic Doppler shifting and boosting of the emission from each single volume of the proceeding jet, we achieve spectra for different angles between the line-of-sight and the jet-axis. Free parameters are the black hole/accretor mass $M = 5M_\odot$, the jet mass flow rate $\dot{M}_{\text{jet}} = 10^{-10}M_\odot/\text{yr}$, the shape of the magnetic field lines determined by $z(x)$ and the choice of the angle between the line-of-sight and the jet-axis. Conserved quantities along the surfaces of constant magnetic flux are: total energy density, total angular momentum, mass flow rate per flux surface and iso-rotation parameter.

The thermal spectra of the optically thin jet flow are here calculated starting from the MHD equations. In turn, from the comparison of the theoretical spectra with observations we might get information about the structure of the jet very close to the black hole. We emphasize that our approach is not (yet) a *fit* to certain observed spectra. In contrary, for the first time, for a jet flow with characteristics defined by the solution of the MHD wind equation, we derive its X-ray spectrum.

4.2 The MHD wind solution from a rotating black hole

The solutions of the magnetic wind equation in Kerr metric were presented by Fendt & Greiner (2001) with particular application to microquasars. Here, some major points are briefly discussed.

A stationary, polytropic, general relativistic MHD flow along an axisymmetric flux surface can be described by the following wind equation for the relativistic poloidal velocity $u_p \equiv \gamma \tilde{u}_p/c$, \tilde{u}_p is the Newtonian poloidal velocity:

$$u_p^2 + 1 = -\sigma_m \left(\frac{E}{\mu} \right)^2 \frac{k_0 k_2 + \sigma_m 2k_2 M^2 - k_4 M^4}{(k_0 + \sigma_m M^2)^2}, \quad (4.1)$$

where

$$\begin{aligned} k_0 &= g_{33}\Omega_F^2 + 2g_{03}\Omega_F + g_{00}, \\ k_2 &= 1 - \Omega_F \frac{L}{E}, \\ k_4 &= - \left(g_{33} + 2g_{03} \frac{L}{E} + g_{00} \frac{L^2}{E^2} \right) / \left(g_{03}^2 - g_{00}g_{33} \right) \end{aligned}$$

(Camenzind 1986; Takahashi et al. 1990).²

$\sigma_m = -1$ stands for the sign of the metric. E is the total specific energy density of the flow, $M^2 = 4\mu n' u_p^2 / \tilde{B}_p^2$ the Alfvén Mach number, n' the proper particle density, μ the specific enthalpy and $\tilde{B}_p = B_p / (g_{00} + g_{03}\Omega_F)$ the poloidal magnetic field rescaled for mathematical convenience. $\Omega_F = \Omega_F(\Psi)$ is the iso-rotation parameter and L the specific angular momentum for the jet, while a is the black hole angular momentum parameter.

For a polytropic gas law, $P \propto \rho^\Gamma$ ($\Gamma = 5/3$), the wind equation (4.1) can be converted into a polynomial equation, whose coefficients are functions of the normalized cylindrical radius $x = R/r_g$, where R is the cylindrical radius and $R_S = 2r_g$ (depending on a) is the gravitational radius.

Usually the general relativistic equations are normalized to the gravitational radius, whereas the special relativistic equations are normalized to the asymptotic light cylinder radius (as seen in Chapter 2).

For each volume element along the magnetic flux surface, values of velocity, density and temperature are obtained (see Fig. 4.1). This allows for the calculation of an optically thin X-ray spectrum defined by this wind solution. The wind solution can be calculated to arbitrary radii, here, a subset of the whole solution will be considered, till $x \leq 500$. Each volume element is defined as $\Delta s \Delta n (x \Delta \phi)$, where Δs is the line element along the poloidal field line, Δn is the one across the flux surface and $\Delta l_\phi = x \Delta \phi$ is the line element in ϕ direction. Due to the choice of $\Delta \phi = 0.1$, a horizontal jet-torus of rectangular cross section (hereafter only jet-torus) contains 63 volume elements. The choice of the length of Δs takes into account that gradients of velocities, densities and temperatures should be small within the volume ($\leq 1\%$). $\Phi(x)$ is the flux tube function, that express the opening of the flux surfaces. For the wind solution, it is $\Phi(x) = 1$, that implies $\Delta n = \Delta l_\phi$. $\Phi(x) = |\frac{\partial \psi}{\partial n}| x = B_P x^2$. Chosen the shape of the flux surface, determined by $z(x)$, $\Phi(x)$ defines the position of the other flux surfaces. Note that in a fully self-consistent approach the field structure could be determined by the solution of the GS equation, but such self-consistent solutions are not yet available. In the innermost part of the jet the flow is not yet collimated, therefore it is basically moving in radial direction, this is the reason of the linear volume dependence visible in Fig. 4.1. For radii $x > 500$, that means temperatures $T < 10^{6.62}$ K, the flow collimates. The poloidal velocity u_p (see Fig. 4.1)³ saturates at $u_{p\infty} = 2.58$ for $x_\infty = 10^8$, $\gamma = 2.8$. It reaches the slow magnetosonic speed at $x = 9$, the fast magnetosonic speed at $x = 136$ and the Alfvén speed at $x = 23$. The asymptotic light cylinder radius is located at $x = 28$.

²In Kerr geometry, for Boyer-Lindquist coordinates, the components of the metric tensor are defined as: $g_{00} = \sigma_m(2r/\rho(r, \theta)^2 - 1)$, $g_{03} = -\sigma_m 2ra \sin(\theta)^2 / \rho(r, \theta)^2$, $g_{33} = \sigma_m \Sigma(r, \theta)^2 \sin(\theta)^2 / \rho(r, \theta)^2$, with $\rho^2 \equiv r^2 + a^2 \cos^2 \theta$, where r and θ are similar to their flat space counterpart spherical coordinates.

³Note that in Fendt & Greiner (2001) αu_p is plotted, where α is the lapse function describing the lapse of the proper time τ to the global time t .

4.3 Thermal emission

We distinguish two parts of the inner jet flow. One is for a temperature range $T = 10^{6.6}-10^9$ K, where we calculate the optically thin continuum and the emission lines. The other is for $T = 10^9-10^{12}$ K, where only bremsstrahlung is important.

In the hypothesis of optically thin plasma, for temperature range $T = 10^{6.2}-10^9$ K we got the emissivities (erg/cm³/sec/0.1 keV) in the energy band 0.2–10.1 keV, having a bin size of 0.1 keV (Brinkmann 2001) for our wind solution. Taking into account the size and the density for a certain volume, the luminosity (erg/sec/0.1 keV) of a jet-torus of 63 volume elements has been calculated. Examples of four different temperatures are shown in Fig. 4.2.

The computation of the continuum spectrum and the emission lines of an optically thin plasma takes into account free-free, free-bound and two-photon processes (Mewe, Gronenschild & van der Oord 1985; Kotani et al. 1996; Brinkmann & Kawai 2000). The cosmic abundances used are those given by Allen (1973) for a plasma in ionization equilibrium at a certain temperature T .

Figure 4.2 shows that, with the increase of the temperature, the luminosity range is compressed, therefore the spectra in Fig. 4.2 (*top*) look steeper and with a stronger cutoff than those in Fig. 4.2 (*bottom*) and the strong cutoff seen for lower temperatures disappears. The luminosity of hot gas volume elements ($T \simeq 10^9$ K), located above the injection point, is higher (factor 100) than the one of the cooler, but faster volume elements.

It is important to remark that the luminosities shown in Fig. 4.2 are calculated for a jet mass flow rate of $\dot{M}_{\text{jet}} = 10^{-10} M_{\odot}/\text{yr}$. This quantity is not known from observations, therefore the calculated luminosities provide an essential check for the jet mass flow rate choice. In fact, using a jet mass flow rate of $\dot{M}_{\text{jet}} = 10^{-8} M_{\odot}/\text{yr}$ the luminosity would increase of a factor 10^4 , for the same magnetic field geometry.

In the energy band 0.2–10.1 keV many emission lines are found for temperatures $T = 10^{6.2}-10^9$ K (Mewe, Gronenschild & van der Oord 1985; Brinkmann 2001). The energy band 0.5–0.9 keV contains O, N, Fe, Ne, S, Ca emission lines. The energy band 1.0–4.0 keV contains Ne, Fe, Mg, Ni, Si, S, Ar, Ca emission lines. The energy band 6.6–7.0 keV mostly contains FeXXV and FeXXVI emission lines. These lines are also temperature indicators (Brinkmann & Kawai 2000). FeXXV is the He-like iron and FeXXVI is the H-like iron. For temperatures higher than $T = 10^9$ the plasma is fully ionized, therefore Bremsstrahlung continuum emission is dominant.

In order to calculate the thermal continuum emission of an optically thin fully ionized plasma we use the formula of the Bremsstrahlung emission (erg/sec/cm³/Hz):

$$\varepsilon_{\nu} \equiv \frac{dW}{dV dt d\nu} = 6.8 \times 10^{-38} Z^2 n_e n_i T^{-1/2} e^{-h\nu/kT} \bar{g}, \quad (4.2)$$

where $\bar{g}(T, \nu)$ is the *velocity averaged Gaunt factor* (Rybicki & Lightman 1979), Z is the atomic number, n_e is the electrons density, n_i the ions density, h is the Planck's constant and k the Boltzmann's constant. A good estimate can be made by setting \bar{g} to unity. For the spectra shown this factor differs slightly from volume to volume.

Considering size and density of the volume element,⁴ for temperatures up to 10^9 K, we obtain values comparable with the luminosities in Fig. 4.2 as expected. In fact, Bremsstrahlung is included in that calculation. For temperature $T = 10^{10}$ K, the Bremsstrahlung luminosity is $L_{\text{br}} \sim 10^{25}$ erg/sec/0.1 keV with a Bremsstrahlung cutoff energy ($h\nu \sim kT$) at 827 keV. For temperature $T = 10^{11}$ K we obtain $L_{\text{br}} \sim 10^{27}$ erg/sec/0.1 keV with a cutoff energy at 8.27 MeV. For temperature $T = 10^{12}$ K is $L_{\text{br}} \sim 10^{30}$ erg/sec/0.1 keV and the cutoff energy is at 82.7 MeV. Therefore, we expect an increase of the X-ray luminosity due to the bremsstrahlung contribution of the hottest regions in the jet-disk system, if the optically thin condition is still satisfied there.

Gamma-ray emission can be expected by the hottest innermost part of the jet-disk system (Fendt & Memola 2001b). OSSE (Oriented Scintillation Spectrometer Experiment), one of the four instruments aboard the Compton Gamma Ray Observatory, has observed the microquasar GRS 1915+105 nine times in 1995–2000 and the data show a spectrum extending up to ≥ 600 keV without any break (Zdziarski et al. 2001).

⁴A factor 2.418×10^{16} converts the units to erg/sec/0.1 keV.

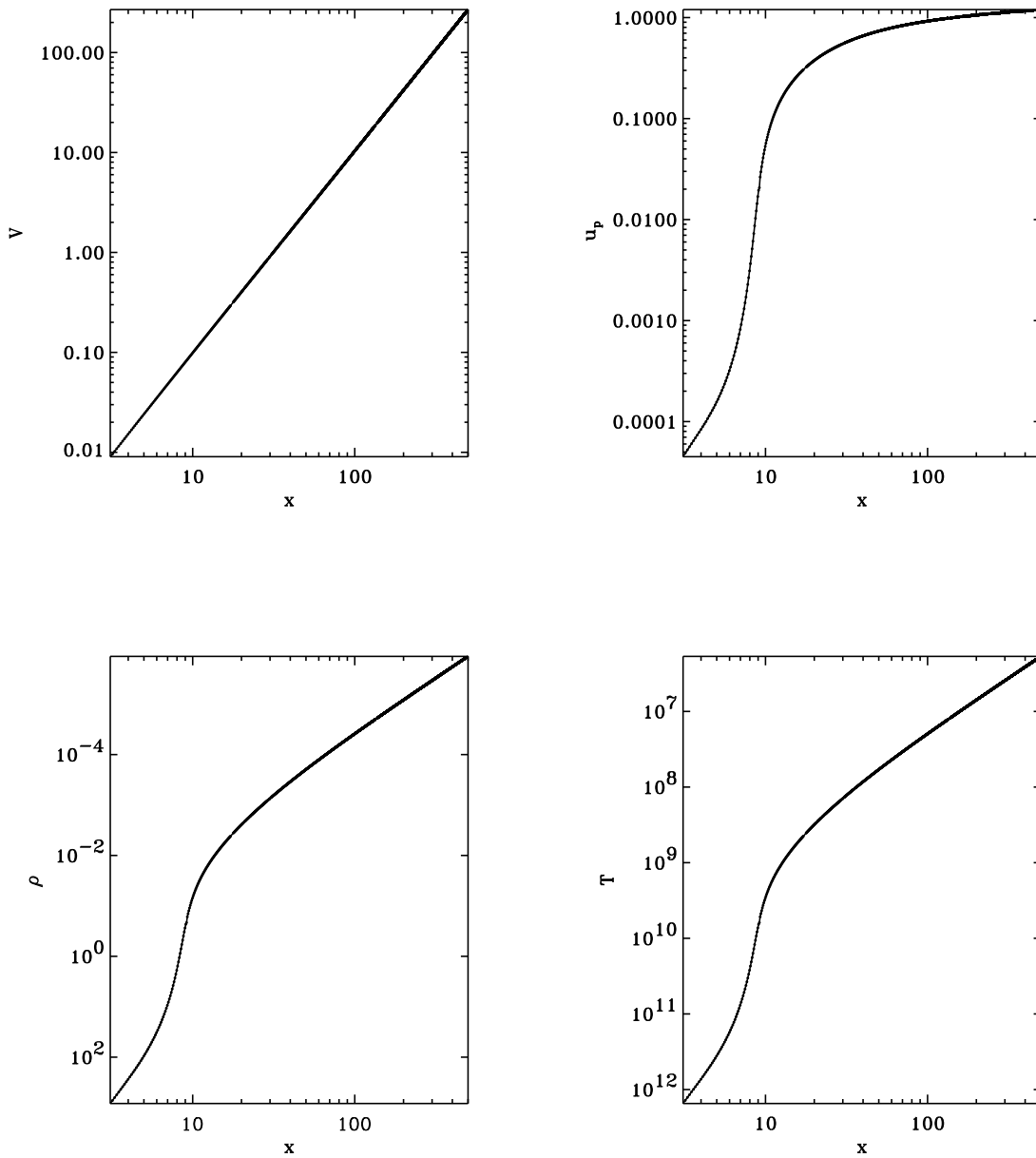


Figure 4.1: Inner part of the wind equation solution. For $M = 5M_{\odot}$ and $\dot{M}_{\text{jet}} = 10^{-10}M_{\odot}/\text{yr}$, the radii x are normalized to the gravitational radius $r_g = 7.4 \times 10^5$ cm, the volume elements, V , are normalized to 4.1×10^{17} cm³ and the particle density ρ is normalized to 4.31×10^{16} cm⁻³. $u_p \equiv \gamma \tilde{u}_p/c$ is the poloidal velocity. The plasma temperature T is in Kelvin. The flow is weakly collimated reaching an half opening angle of 70° at about $x = 250$.

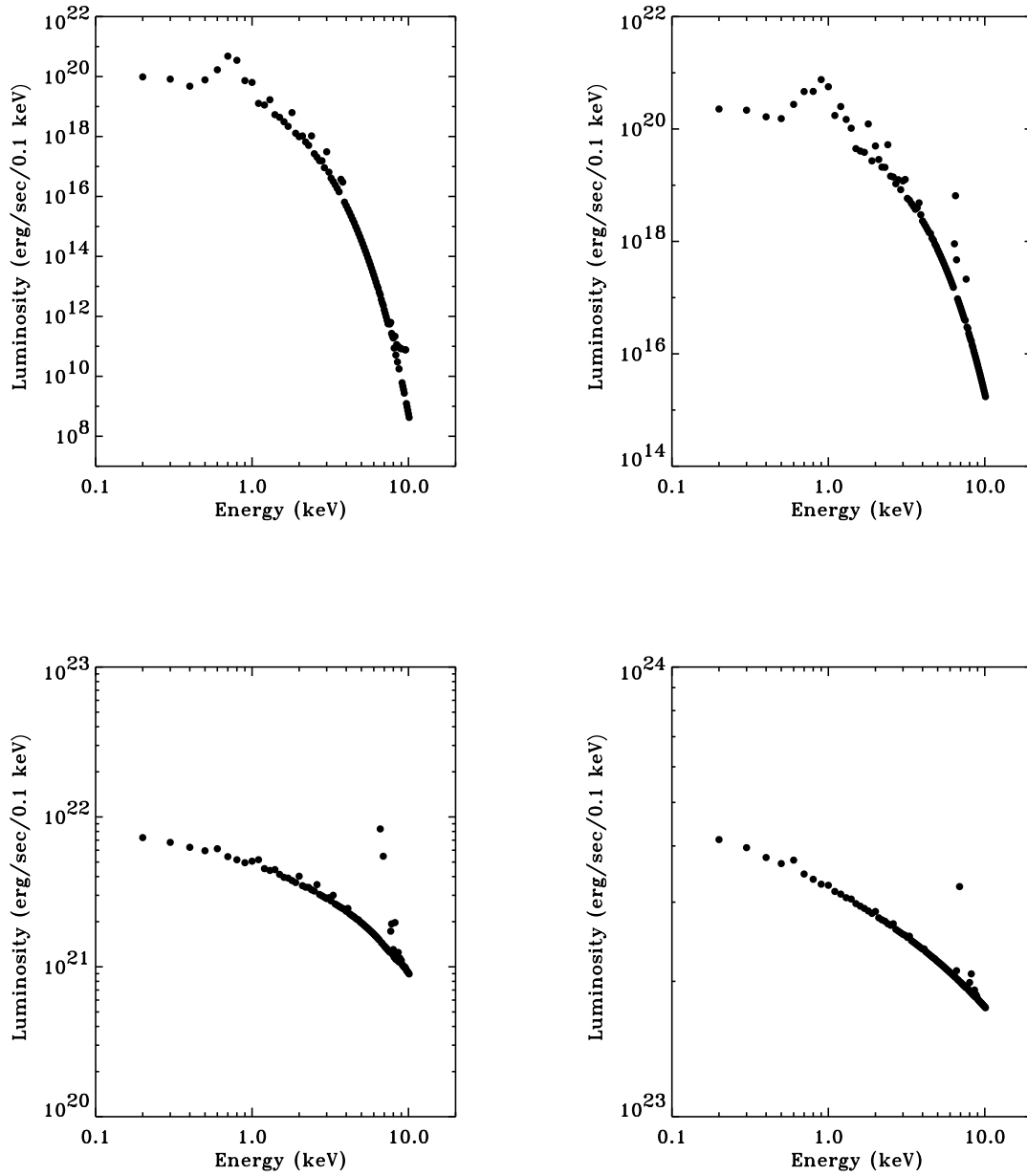


Figure 4.2: X-ray luminosities for a jet-torus of 63 volume elements ($\dot{M}_{\text{jet}} = 10^{-10} M_{\odot}/\text{yr}$). *Top:* $T = 10^{6.64}$ K and $T = 10^7$ K. *Bottom:* $T = 10^8$ K and $T = 10^9$ K.

Chapter 5

Theoretical thermal X-ray spectra

5.1 The rest frame spectrum

In order to calculate the X-ray spectra we sum up the luminosities of each volume in the same energy bin for the whole temperature distribution ($10^{6.2}$ – 10^9 K) along the jet, that corresponds to 5000 volume elements along a single field line. Taking also into account the 63 volume elements in ϕ direction we obtain the theoretical thermal rest frame spectrum of a conical sheet (formed by the 5000 jet-tori).

As a first step, the rest frame spectrum is calculated without taking into account relativistic effects of Doppler boosting and shifting. This spectrum is showed in Fig. 5.1. The lines at 6.6 keV and 6.9 keV may be identified as the $K\alpha$ lines from He-like and H-like irons, while the one at 8.2 keV could be the $K\beta$ from the He-like iron.

From a total jet mass flow rate along the whole jet $\dot{M}_{\text{jet}} = 10^{-10} M_{\odot}/\text{yr}$, we derive a mass flow rate through a jet-torus section perpendicular to the jet-axis of $2 \times 10^{-11} M_{\odot}/\text{yr}$.

The total rest-frame X-ray luminosity of the jet is $L_{\text{X,tot}} = 37.7 \times 10^{26}$ erg/sec.¹ The total kinetic luminosity of the jet is $L_{\text{k}} = \gamma \dot{M}_{\text{jet}} c^2 = 1.5 \times 10^{37}$ erg/sec. We see that $L_{\text{k}} \gg L_{\text{X,tot}}$. This proves, *a posteriori*, that the basic assumption of a polytropic gas law ($P \propto \rho^{\Gamma}$, $\Gamma = 5/3$) used to obtain the MHD wind solution is consistent with the amount of radiation losses. We now consider the relativistic effects for the jet moving toward the observer. We do not take into account the counter-jet, which would be treated in a similar way. However, due to the receding character of the counter-jet, the luminosities would be de-boosted.

¹It includes a factor 5 that comes from the ratio between the area of a surface perpendicular to the jet-axis and the area of a section (perpendicular to the jet-axis) of the 63 volume elements jet-torus. The factor remains constant along the jet.

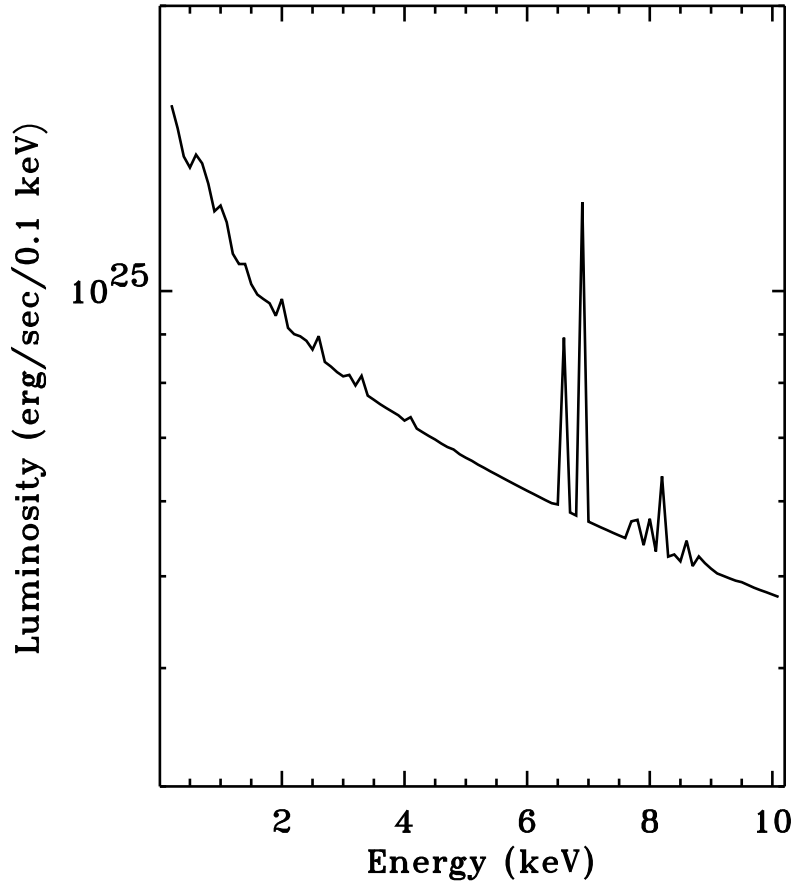


Figure 5.1: Rest frame spectrum for a jet conical sheet.

5.2 The Doppler shifted and Doppler boosted spectra

The relativistic Doppler factor is defined as:

$$D = \frac{1}{\gamma(1 - \beta \cos \theta)}, \quad (5.1)$$

where $\gamma = (1 - \beta^2)^{-1/2}$ is the Lorentz factor, $\beta = u/c$ is the plasma velocity in units of the speed of light (Rybicki & Lightman 1979) and θ is the angle between the velocity vector and the line-of-sight (in the rest frame). Due to the relativistic motion, the observed energies, E_o and corresponding luminosities, L_o of *each* volume element will be respectively shifted and boosted following Eq. (5.2) and (5.3), over the ones emitted (calculated) in the rest frame, E_e and L_e :

$$E_o = D E_e, \quad (5.2)$$

$$L_o(E_o) = D^3 L_e(E_e). \quad (5.3)$$

T (K)	M (gr)	ρ (cm $^{-3}$)	γ	θ_{\parallel} ($^{\circ}$)	D_{\parallel}	D_{-20}	D_{+20}	D_{-40}	D_{+40}
(1)	(2)	(3)	(4)	(5)	(6)	(7)	(8)	(9)	(10)
10^9	6.608×10^7	5.948×10^{14}	1.014	81.76	1.010	1.069	0.955	1.123	0.909
10^8	1.754×10^7	1.896×10^{13}	1.179	77.26	0.960	1.189	0.795	1.467	0.682
10^7	1.068×10^7	5.991×10^{11}	1.428	72.01	0.898	1.249	0.683	1.774	0.552
$10^{6.64}$	9.719×10^6	1.733×10^{11}	1.494	69.88	0.899	1.284	0.670	1.881	0.534

Table 5.1: Four example volume elements and their related parameters. The higher temperature refers to the jet region closer to the accretor. Quoted are the temperature T , the mass M , the particle density ρ and the Lorentz factor γ . The angle θ_{\parallel} is between the plasma velocity and the line-of-sight, if the line-of-sight is parallel to the jet-axis. The Doppler factor corresponding to this angle is D_{\parallel} . If the line-of-sight is inclined of 20° to the jet-axis, the minimum angle between the plasma velocity and the line-of-sight is $\theta_{\parallel} - 20^{\circ}$ and the corresponding Doppler factor is D_{-20} , while the maximum angle between the plasma velocity and the line-of-sight is $\theta_{\parallel} + 20^{\circ}$ and the corresponding Doppler factor is D_{+20} . In the same way, for an angle of 40° between the line-of-sight and the jet-axis we calculate D_{-40} and D_{+40} .

As an example, we provide the parameters for a sample of four volume elements (see Table 5.1). In column (1) is the temperature of a certain volume element. For that volume, its mass (column 2), particle density (column 3) and Lorentz factor (column 4) are quoted.

In column (5), $\theta = \theta_{\parallel}$ is the angle between the direction of the plasma velocity and the line-of-sight, if the line-of-sight is parallel to the jet-axis. We also consider other two cases: the line-of-sight inclined to the jet-axis of 20° and the line-of-sight inclined to the jet-axis of 40° . This means that the minimum angle between the plasma velocity and the line-of-sight will be $\theta = \theta_{\parallel} - 20^{\circ}$ in the first case and $\theta = \theta_{\parallel} - 40^{\circ}$ in the

second case whereas the maximum angle between the plasma velocity and the line-of-sight will be $\theta = \theta_{\parallel} + 20^\circ$ in the first case and $\theta = \theta_{\parallel} + 40^\circ$ in the second one.

In order to provide the boosted and shifted spectra, for each of the five θ (θ_{\parallel} , $\theta_{\parallel} - 20^\circ$, $\theta_{\parallel} + 20^\circ$, $\theta_{\parallel} - 40^\circ$, $\theta_{\parallel} + 40^\circ$), whose values change for each volume element, 5000 corresponding relativistic Doppler factors have been calculated (D_{\parallel} , D_{-20} , D_{+20} , D_{-40} , D_{+40}). Those values, for the 4 sample volume elements considered in Table 5.1, are in columns (6),(7),(8),(9) and (10).

Taking into account the change of the velocity direction (of the angle θ_{\parallel}) toward the line-of-sight along the jet-torus, it has been considered reasonable to divide the 2π jet-torus of 63 volume elements in two regions: 1) 1/3 of the size containing 21 volume elements, for them the Doppler effect has been calculated using the minimum angles between the plasma velocity and the line-of-sight ($\theta_{\parallel} - 20^\circ$ or $\theta_{\parallel} - 40^\circ$), 2) 2/3 of the size containing 42 volume elements, for them the Doppler effect has been calculated using the maximum angles between the plasma velocity and the line-of-sight ($\theta_{\parallel} + 20^\circ$ or $\theta_{\parallel} + 40^\circ$).

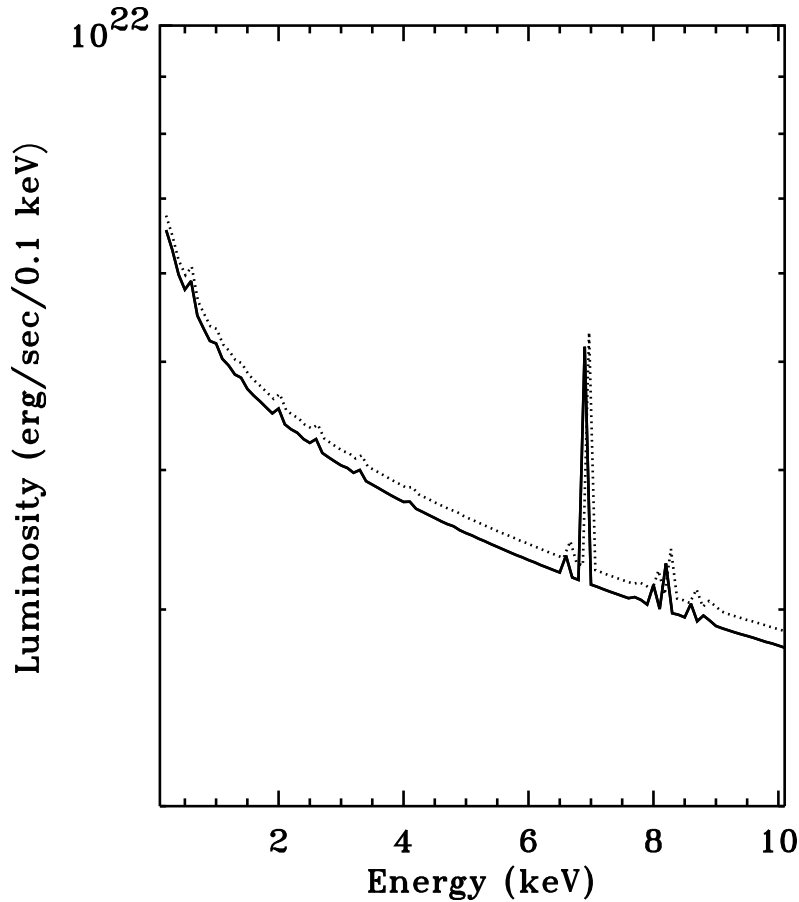


Figure 5.2: Doppler shifted and boosted spectrum by Doppler factor D_{\parallel} (dotted line) of a single volume element at $T = 10^9$ K and rest frame spectrum (solid line).

Figure 5.2 shows the shifted and boosted spectrum of the volume element at $T = 10^9$ K in Table 5.1 calculated using $D_{\parallel} = 1.010$ ($\theta_{\parallel} = 81.76^\circ$). In this case we have only a weak Doppler boosting and shifting effect, in fact, we are looking almost perpendicular to an uncollimated flow.

It is important to underline that the Doppler factor has a strong dependence on the viewing angle (Urry & Padovani 1995) which gets stronger for larger Lorentz factors. The Doppler factor D is unity for $\theta_D = \arccos\left(\sqrt{(\gamma - 1)/(\gamma + 1)}\right)$, for angles larger than θ_D relativistic *deamplification* takes place. This is the reason for Doppler factors smaller than unity in our jet (see Table 5.1). Also known as second order Doppler effect, it was first observed in SS 433 (Margon 1984). De-boosting is also present in the asymptotic radio jets (different from the collimation region investigated here) of GRS 1915+105 inclined by 70° to the line-of-sight, actually providing a distance indicator (Mirabel & Rodríguez 1994).

Looking at different inclinations to the jet the shifting and boosting effect becomes larger. Figure 5.3 ($T = 10^9$ K, $D_{-20} = 1.069$ (left), $D_{+20} = 0.955$ (right)) and Fig. 5.4 ($T = 10^9$ K, $D_{-40} = 1.123$ (left), $D_{+40} = 0.909$ (right)) illustrate these effects. In Fig. 5.3 (left) and Fig. 5.4 (left) boosting and blue-shifting (dotted, dotted-dashed, triple dotted-dashed line) of the rest frame spectra (solid line) are visible, whereas Fig. 5.3 (right) and Fig. 5.4 (right) show a de-boosting and red-shifting of the spectra. The maximum boosting is obtained via the Doppler factor $D_{-40}^3 = 6.65$ (for the temperature value $T = 10^{6.64}$ K) and the maximum de-boosting, for the volume at the opposite side of the cone, via the Doppler factor $D_{+40}^3 = 0.15$ for the same temperature. The line shifting is clearly visible.

In Fig. 5.5 all the shifted and boosted spectra calculated for $T = 10^9$ K (left) and $T = 10^7$ K (right) are plotted together. The spectra of the volume element at lower temperature are steeper than the higher temperature ones. The higher temperature plasma is moving with slower speed, therefore Doppler boosting and shifting are more visible in the lower temperature summarizing plot (Fig. 5.5, right). Note that, due to the value of the Doppler factor D_{\parallel} (see also Table 5.1), the corresponding spectrum is blue-shifted if the temperature value is $T = 10^9$ K (Fig. 5.5, left, blue dotted line) and red-shifted when $T = 10^7$ K (Fig. 5.5, right, red dotted line).

5.3 Total Doppler shifted and boosted spectra

We sum up the luminosities from each volume element (with a different temperature) along the jet. Since the volume elements have also different velocities, the single spectra are shifted and boosted. We need then to interpolate the single volume luminosity values, in order to obtain a total shifted and boosted spectrum.

In Fig. 5.6 (left), only a single volume element in ϕ direction has been considered, this plot can therefore be compared with the ones in Fig. 5.7. In Fig. 5.6 (right), the calculated spectra of the jet conical sheet are shown. When the Doppler factor is D_{\parallel}

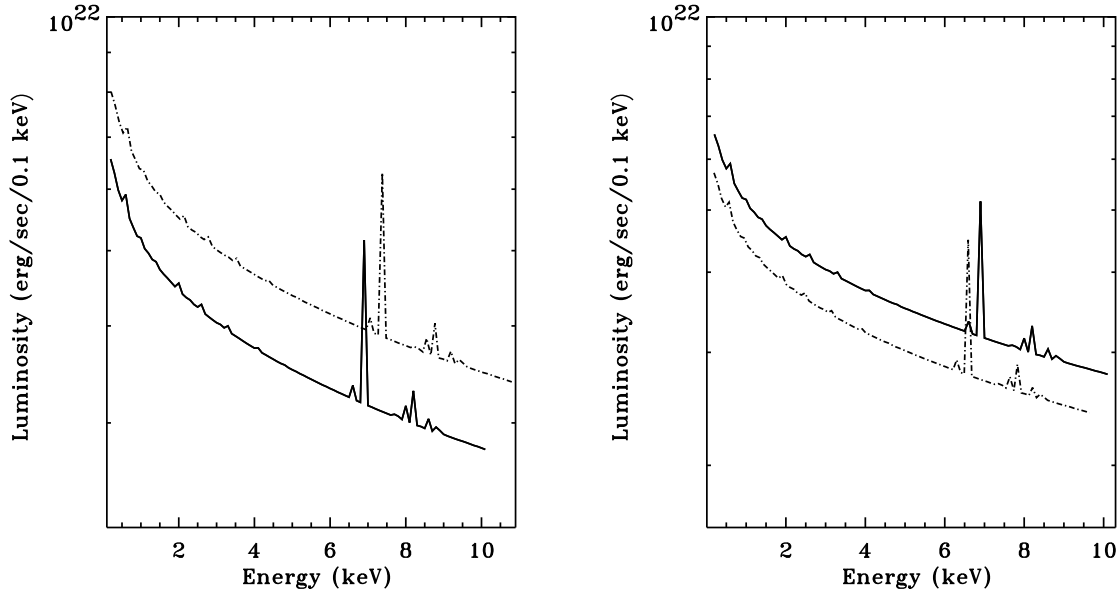


Figure 5.3: *Left*: Blue-shifted and boosted spectrum by Doppler factor D_{-20} (dotted-dashed line) of a single volume element at temperature $T = 10^9$ K and rest frame spectrum (solid line). *Right*: Red-shifted and de-boosted spectrum by Doppler factor D_{+20} (dotted-dashed line) of a single volume element at temperature $T = 10^9$ K and rest frame spectrum (solid line).

(the line-of-sight is parallel to the jet-axis), the difference between Fig. 5.6 (*left*) and Fig. 5.6 (*right*) is exactly of a factor 63 in luminosity. The iron lines appear to be de-boosted and slightly shifted.

The total X-ray luminosity of the jet considering the boosting due to D_{\parallel} is $L_{X_{\text{tot}}} = 6.4 \times 10^{28}$ ($\dot{M}_{\text{jet}} = 10^{-10} M_{\odot}/\text{yr}$) erg/sec and, for a different jet mass flow rate, $L_{X_{\text{tot}}} = 6.4 \times 10^{32}$ ($\dot{M}_{\text{jet}} = 10^{-8} M_{\odot}/\text{yr}$) erg/sec.

More complicated cases, when the line-of-sight is inclined to the jet-axis, are shown in Fig. 5.7. These are our tentatively combined spectra for a line-of-sight that forms an angle of 20° (*left*) and 40° (*right*) with the jet-axis. An interpolation process is necessary not only to calculate the blue-shifted (blue curves) and red-shifted (red curves) part of the spectra, but also to calculate their combined spectra (green curves). The total spectra have been calculated first weighing the blue-part for 21 volume elements and the red-part for 42 volume elements, then, summing up the values only where both data were available and renormalizing to 63, in order to plot all the contributions together.

An interesting consideration can be done about the iron line features in Fig. 5.7 for the curves representing the boosting and shifting due to the Doppler factors D_{-20} and

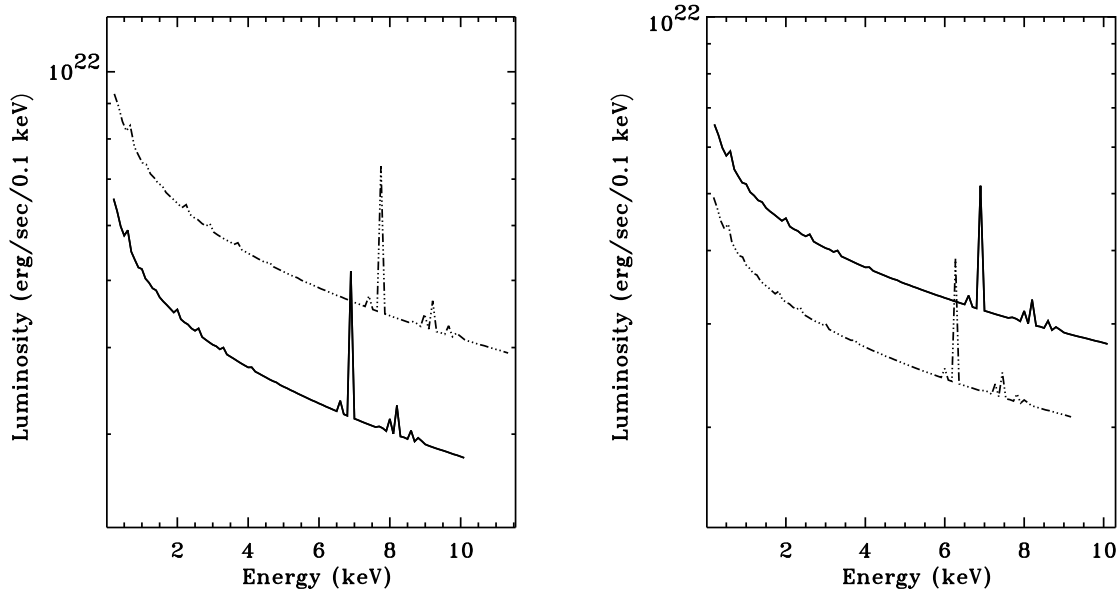


Figure 5.4: *Left*: Blue-shifted and boosted spectrum by Doppler factor D_{-40} (triple dotted-dashed line) of a single volume element at $T = 10^9$ K and rest frame spectrum (solid line). *Right*: Red-shifted and de-boosted spectrum by Doppler factor D_{+40} (triple dotted-dashed line) of a single volume element at $T = 10^9$ K and rest frame spectrum (solid line).

D_{-40} . In the first case the iron lines features are considerably shifted also after the interpolation. The change in the line shape is due to the fact that for each of the 5000 volumes along the jet a different Doppler factor must be considered. In the second case, for a larger jet inclination, the lines, shifted to higher energies, are widely spread out. The feature around 1.5 keV is probably due to a lack of resolution, the bin size is 0.1 keV. The cuspid might be only an artefact. The de-boosting contribution of the receding counter-jet has not been taken into account.

The total X-ray luminosity of the jet considering the boosting due to the combined effect of D_{-20} and D_{+20} is $L_{X_{\text{tot}}} = 1.4 \times 10^{29}$ ($\dot{M}_{\text{jet}} = 10^{-10} M_{\odot}/\text{yr}$) erg/sec and $L_{X_{\text{tot}}} = 1.4 \times 10^{33}$ ($\dot{M}_{\text{jet}} = 10^{-8} M_{\odot}/\text{yr}$) erg/sec, while for the case D_{-40} and D_{+40} we gain $L_{X_{\text{tot}}} = 1.1 \times 10^{29}$ ($\dot{M}_{\text{jet}} = 10^{-10} M_{\odot}/\text{yr}$) erg/sec and $L_{X_{\text{tot}}} = 1.1 \times 10^{33}$ ($\dot{M}_{\text{jet}} = 10^{-8} M_{\odot}/\text{yr}$) erg/sec. These values can be increased by the contribution of bremsstrahlung from the high temperature ($T \geq 10^9$ K) volumes till about $\approx 10^{34}$ erg/sec.

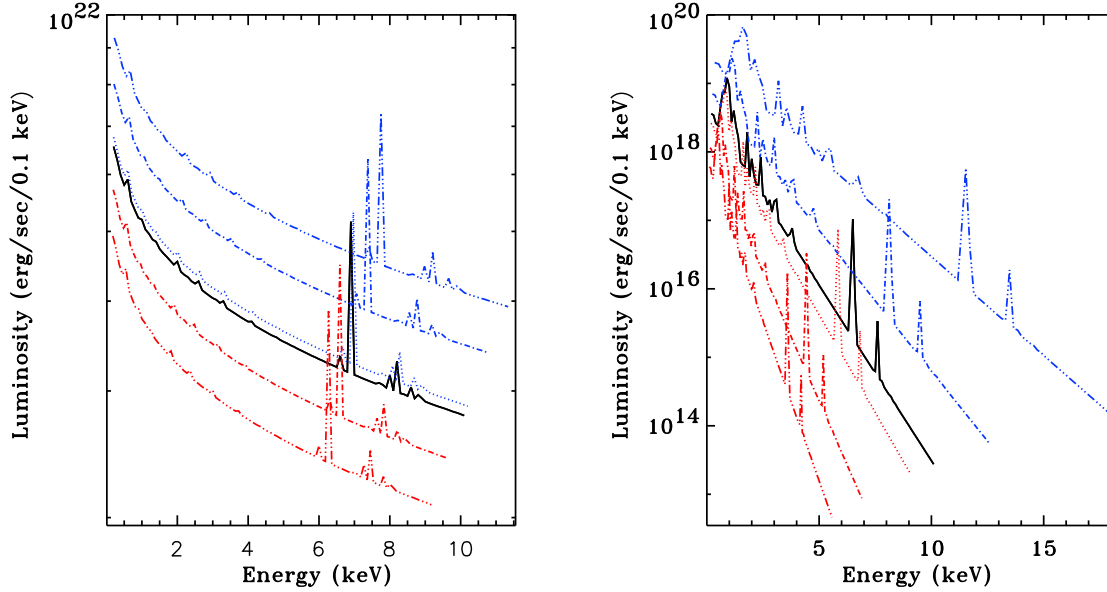


Figure 5.5: Doppler shifted and boosted spectra of a single volume element: summarizing plot. *Blue*: blue-shifted spectra. *Black*: rest frame spectrum. *Red*: red-shifted spectra. *Left*: $T = 10^9$ K. *Right*: $T = 10^7$ K. For comparison, see Figs. 5.2, 5.3, 5.4, Table 5.1.

5.4 Comparison with observations

We find X-ray emission from the hot part of the collimating, accelerated, galactic superluminal magnetic jet very close to its origin. The calculated spectra (Memola, Fendt & Brinkmann 2002) are the result of a truly MHD calculation, which describes the real flow characteristics. The $K\alpha$ He-like iron emission line of our theoretical thermal spectra is probably confirmed by ASCA (0.5–10 keV) observations of GRS 1915+105 (Ebisawa et al. 1998) and the $K\alpha$ H-like iron emission line might be present in ASCA observations of XTE J1748–288 (Kotani et al. 2000).

In GRS 1915+105 the ejecta move at an angle $\theta = 70^\circ$ with respect to the line-of-sight (Mirabel & Rodríguez 1994). It has to be clarified that this is the case of a large-scale asymptotic *collimated* jet, where the motion is always parallel to the jet-axis. In our small-scale *collimating* jet an angle of 70° between the motion and the line-of-sight is obtained for $\theta = \theta_{\parallel}$ if the temperature is $T = 10^{6.64}$ K. Note that in our case of uncollimated wind the velocity (the motion) is directed away from the jet-axis of an angle $\theta = \theta_{\parallel}$.

GRS 1915+105 X-ray luminosity is 10^{38} erg/sec in low-state and 10^{39} erg/sec in high-state (Greiner, Morgan & Remillard 1996), and larger than the luminosity we gain.

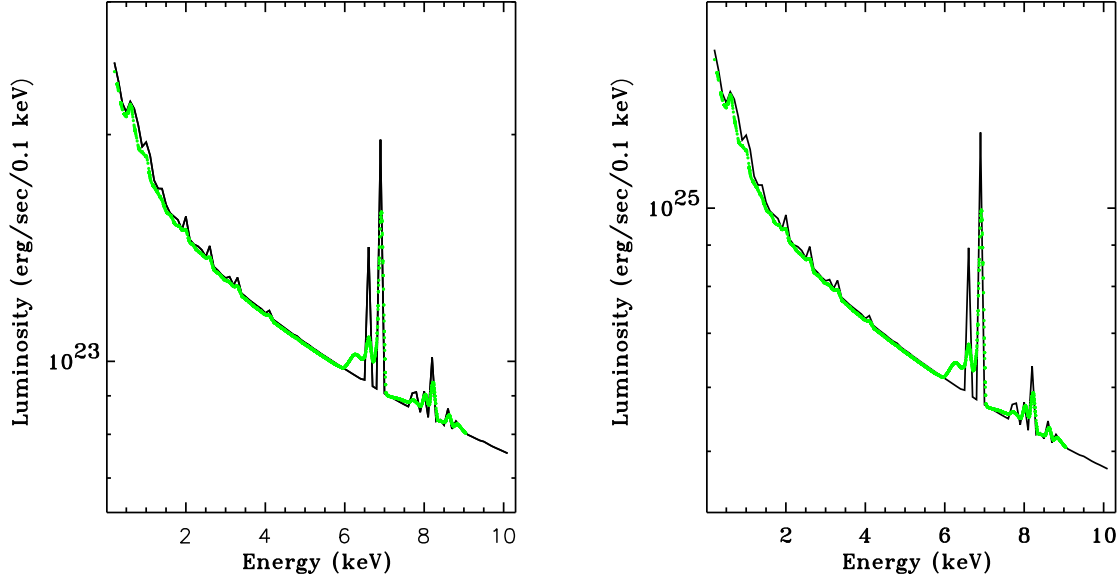


Figure 5.6: *Left*: Doppler shifted and boosted spectrum of the 5000 volumes elements along the jet (green) for Doppler factor D_{\parallel} and rest frame (black). *Right*: Doppler shifted and boosted spectrum of the jet conical sheet (green) for Doppler factor D_{\parallel} and rest frame (black).

The difference might be explained by several reasons:

- It is not yet clear how much of the X-ray luminosity comes from the disk and how much from the jet.
- The Bremsstrahlung contribution of the hottest inner volumes could increase the value of the total luminosity, if the condition of optically thin plasma would still be satisfied.
- A mass flow rate of $\dot{M}_{\text{jet}} = 10^{-8} M_{\odot}/\text{yr}$ contributes to increase the luminosity of a factor 10^4 .
- A more collimated field distribution would imply larger velocities and smaller angles between the plasma motion and the line-of-sight, this would lead to a larger Doppler shifting and boosting.
- Higher jet velocities ($\gamma > 2$) may increase the Doppler boosting. Such velocities can be easily obtained for a higher flow magnetization, i.e. for a stronger magnetic field strength or a lower jet mass flow rate (see e.g. Fendt & Camenzind 1996). However, for the same mass flow rate, a higher velocity implies a

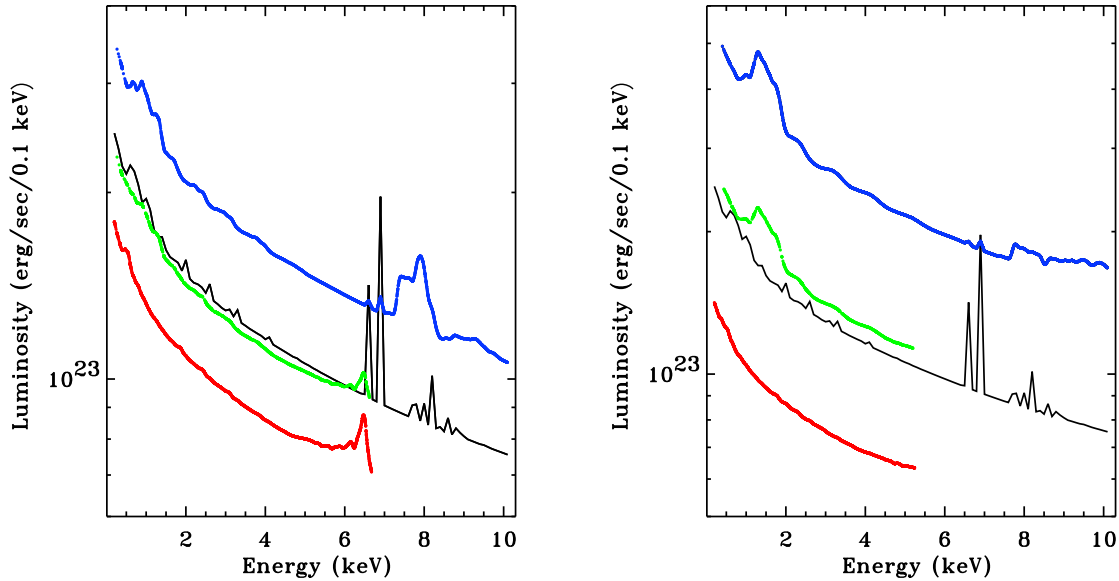


Figure 5.7: *Left*: Interpolated Doppler shifted and boosted spectrum along the jet for Doppler factors D_{-20} (blue) and D_{+20} (red). Total spectrum (green) and rest frame (black). *Right*: Interpolated Doppler shifted and boosted spectrum along the jet for Doppler factors D_{-40} (blue) and D_{+40} (red). Total spectrum (green) and rest frame (black).

lower gas density, which may lead, instead, to a decrease of the luminosity. The interaction of these effects is rather complex.

- Answering the question how these effects determine the observed X-ray luminosity, would require a detailed study of various MHD wind solutions and their derived spectra investigating different magnetic field geometries (degree of collimation), jet mass flow rates (the flow magnetization), and also possible masses of the central black hole.

Markoff, Falcke & Fender (2001) have recently shown (for XTE J1118+480) that synchrotron emission from the jet may play a role also in the X-ray band. Their model differs from ours in some respects, especially the initial jet acceleration is not treated and the jet nozzle geometry is more concentrated along the axis with a jet radius of only 10 Schwarzschild radii (in our model the jet is much wider and collimates later). As a consequence, the densities become higher and it is questionable whether a more reasonable jet geometry will deliver the same amount of X-ray flux.

The theoretical spectra derived provide an additional information needed in order to interpret the observed emission lines. A more detailed investigation might answer

the question whether the line emission, or at least part of it, comes from the highly relativistic jet motion or from a rapidly rotating (i.e. also relativistic) accretion disk. For example, we expect the emission lines of a collimated jet being narrower, and probably shifted by a larger Doppler factor, due to the strong beaming. One should also keep in mind that the direction of motion of the jet material is inclined (if not perpendicular) to the disk rotation.

If the observations would tell us that the Doppler shifted Fe lines which are visible in our theoretical spectra arise in the jet material, this would also prove the existence of a baryonic component in these jets. If jets from X-ray binaries indeed contain matter of baryonic composition, our model will have a broad application. Indication of that is probably given by the observation of iron emission lines in some sources (see above). Our calculated Fe emission lines may help to interpret the observed spectra and potentially give some clue on the plasma composition in relativistic jets. Investigating spectra of jets with different magnetic geometry, mass flow rates and central masses, in the end, might also allow to constrain the intrinsic parameters of jet formation itself (such as mass loading or opening angle) from the observation of the large-scale, asymptotic jet.

Summary

In this thesis the jet formation region of relativistic, magnetic jets using stationary, axisymmetric, magnetohydrodynamic models has been investigated. The advantage of a stationary approach is the possibility to treat the jet physics on a global scale. Our results are applicable to highly relativistic jets as observed in active galactic nuclei and microquasars. In particular, we numerically calculate the field structure of collimating jets, taking into account *differential rotation* of the foot points of the field lines (Fendt & Memola 2001a; Memola & Fendt 2001) and investigate the X-ray emission of the inner jet starting from the jet flow parameters (Fendt & Memola 2001b; Memola, Fendt & Brinkmann 2002).

We calculate the two-dimensional magnetic field distribution in collimating, relativistic jets. The structure of the axisymmetric magnetic flux surfaces is obtained by solving the *modified* relativistic force-free Grad-Shafranov equation numerically. In relativistic magnetohydrodynamics, *electric fields* become important in difference to Newtonian magnetohydrodynamics. The simplifying assumption of the force-free limit has been applied as relativistic jets must be highly magnetized. The accretion disk is in general an important feature in the jet formation process, thus having a differentially rotating disk as boundary condition was a fundamental issue.

Two main problems had to be solved in order to calculate a two-dimensional field distribution: 1) to determine the *a priori* unknown location of the light surface, 2) the proper treatment of the regularity condition along that light surface. The light surface is the force-free equivalent of the Alfvén surface and provides a singularity in the Grad-Shafranov equation.

We find numerical solutions for the two-dimensional magnetic flux distribution connecting the asymptotic cylindrical jet with a differentially rotating disk. In our example solutions the asymptotic jet radius is about 2.5 times the asymptotic light cylinder radii. This is the first truly two-dimensional relativistic solution for a jet magnetosphere including *differential rotation* of the iso-rotation parameter $\Omega_F(\Psi)$. The physical solution, being characterized by a smooth transition of the field lines across the light surface, is unique for a certain parameter choice of the rotation law Ω_F .

The half opening angle of the numerical jet solution is about 60 degrees. Cylindrical collimation is achieved already after a distance of 1–2 asymptotic light cylinder radii along the jet-axis. *Differential rotation* decreases the jet opening angle, but increases

the distance from the jet origin where collimation is achieved. The *jet expansion rate*, defined as the ratio of the asymptotic jet radius to the jet radius at the jet origin, is about 10.

Several interesting properties, which are important for the disk evolution, can be deduced from the asymptotic jet parameters. Examples are the disk toroidal magnetic field distribution, with a maximum at half of the disk radius and the angular momentum flux per unit time and unit radius. This is interesting as a boundary condition for accretion disk models. We find that most of the angular momentum is lost in the outer part of the disk.

Comparison of our model with radio observations at 43 GHz of the M87 jet (Junor, Biretta & Livio 1999), gives good agreement qualitatively. From our numerical solution we derive an asymptotic light cylinder radius of the M87 jet of about 50 Schwarzschild radii. Collimation of the jet would be achieved after a distance of two asymptotic light cylinder radii from the source. This value matches quite well the radio observations, however, the jet opening angle in our model is larger by a factor of two. M87 is a unique example for the combination of a *close* object and a supermassive black hole of $3 \times 10^9 M_{\odot}$. Considering the quasar 3C 273 at a distance of about 600 Mpc we calculate that the collimation region has an angular size of 10^{-6} arcsec, still un-resolvable. It is therefore clear that for most of the extragalactic jet sources theoretical investigations are the only possibility to gain information about the physical processes in the innermost jet region.

Applying the jet flow parameters (velocity, density, temperature) derived by Fendt & Greiner (2001) from the relativistic magnetohydrodynamic wind equation, theoretical thermal X-ray spectra were obtained. We calculate thermal X-ray luminosity along the magnetic flux surfaces in the energy range 0.2–10.1 keV. The total spectra were derived as composition of the spectral contributions of the single volume elements accelerating along the jet with relativistic speed. This is the first time that X-ray spectra have been calculated from the numerical solution of a magnetohydrodynamic jet.

We find X-ray emission from the hot inner part of the jet originating in a region of 2.5×10^{-5} AU diameter close to the center of a $5 M_{\odot}$ jet source. The jet X-ray luminosity is $L_{X_{\text{tot}}} \sim 10^{33} (\dot{M}_j / 10^{-8} M_{\odot} / \text{yr}) \text{ erg/sec}$. Emission lines of Fe XXV and Fe XXVI are clearly visible in our spectra. Interestingly, the $K\alpha$ iron emission line has been probably observed in GRS 1915+105 (Ebisawa et al. 1998) and XTE J1748–288 (Kotani et al. 2000).

Since relativistic effects as Doppler shift and Doppler boosting should be important for these jets, we investigate how the spectra are affected by them considering different inclinations of the line-of-sight to the jet-axis. Since we know the velocity of the jet from the magnetohydrodynamic solution, we find a maximum Doppler boosting of about 7. Minimum boosting is present along the opposite side of the jet cone (Doppler factor 0.53). The shift of the emission lines is always visible. The boosting, however, does not play a major role in the total spectra, because of the uncollimated geometry of the innermost part of the jet emitting the X-rays and the combined effect of boosting

and de-boosting around the jet cone.

Finally, we like to emphasize that our approach is not (yet) a *fit* to certain observed spectra. In contrary, for the first time, for a jet flow with characteristics defined by the solution of the MHD wind equation, we derive its X-ray spectrum. Thus, our free parameters are the mass of the central object M defining the length scales, the jet mass flow rate \dot{M}_{jet} defining the densities and the shape of the poloidal field lines $z(x)$. Comparison of our calculated emission lines to observed ones may also give some hints on the plasma composition in relativistic jets.

“The greater the sphere of our knowledge, the larger the surface of its contact with the infinity or our ignorance”. *Anonymous (surely a scientist!)*

Appendix

A.1 Numerical details

The numerical solution of the *modified* relativistic GS equation (2.21) is obtained using the method of finite elements as developed by Camenzind (1987); Fendt, Camenzind & Appl (1995); Fendt & Memola (2001a); Memola & Fendt (2001). In order to provide the two-dimensional magnetosphere global solution, the inner solution (the field distribution calculated from the jet-axis till the light surface) and the outer solution (the field distribution calculated from the light surface till the jet boundary) are run separately using the Finite Element Code.

The *modified* relativistic GS equation (2.21) contains three non linear terms: the poloidal current, $I(\Psi)$, the angular velocity, $\Omega_{\text{F}}(\Psi)$ and the gradients of the magnetic flux function, $\nabla\Psi$. To deal with those non linearities (in particular the gradients are highly non linear) different iteration loops are necessary. The asymptotic spline functions are used to obtain poloidal current and angular velocity of the asymptotic cylindrically collimated jet. The source term is the right hand side of the *modified* GS equation (2.21).

Differential rotation also implies another complication: position and shape of the light surface are not known *a priori*. The problem of handling the light surface boundary lies in the *zero* present in the left hand side of the *modified* GS equation (2.21), when the condition $R\Omega_{\text{F}}(\Psi) = c$ is fulfilled. Along the light surface the *modified* GS equation reduces to the regularity condition (see Fendt, Camenzind & Appl 1995), the boundary condition along the light surface, that depends on the two-dimensional solution $\Psi(x, z)$. The light surface iteration loop determines a boundary for the grid that allows for the definition of a new grid that is slowly moved to a larger radius. As a consequence of the different numerical grid, the field distribution will change. Plotting the results is possible only after creating an equidistant grid from the non equidistant grid of finite elements.

The calculation of the inner solution takes a couple of weeks (with an HPC 100 – 99 MHz workstation), because of the combination of non linear terms, *differential rotation* and light surface iteration loop. The outer solution is, on the other hand, usually obtained within one hour. In order to save computational time a restart procedure allows to stop the solution to verify the result and restart it from the last light surface

iteration step.

A fragile numerical convergency process can be expected. Appropriate numerical parameters as grid size, element size and iteration step size are necessary. In particular, our grid of finite elements of second order may be inadequate for a calculation of monotonous gradients between the elements if the numerical resolution is too low.

Each of the isoparametric curvilinear finite elements of the serendipity class (Schwarz 1984; Cesari 1994) is formed by 8 nodes (grid points). The numerical grid used to compute both the inner and outer solution of the *modified* relativistic GS equation (2.21) is discretized in a set of 128 finite elements along the x axis and 128 along the z axis, for a total number of 49665 grid points, a good compromise between computational time, disk space and grid resolution. In the example of Fig. A.1 only half of the grid points have been plotted in order to make the grid more visible. The equidistant grid refer to the inner solution of the GS equation (2.21) shown in Fig. 3.7. Note how the grid elements follow the light surface and the star surface shape.

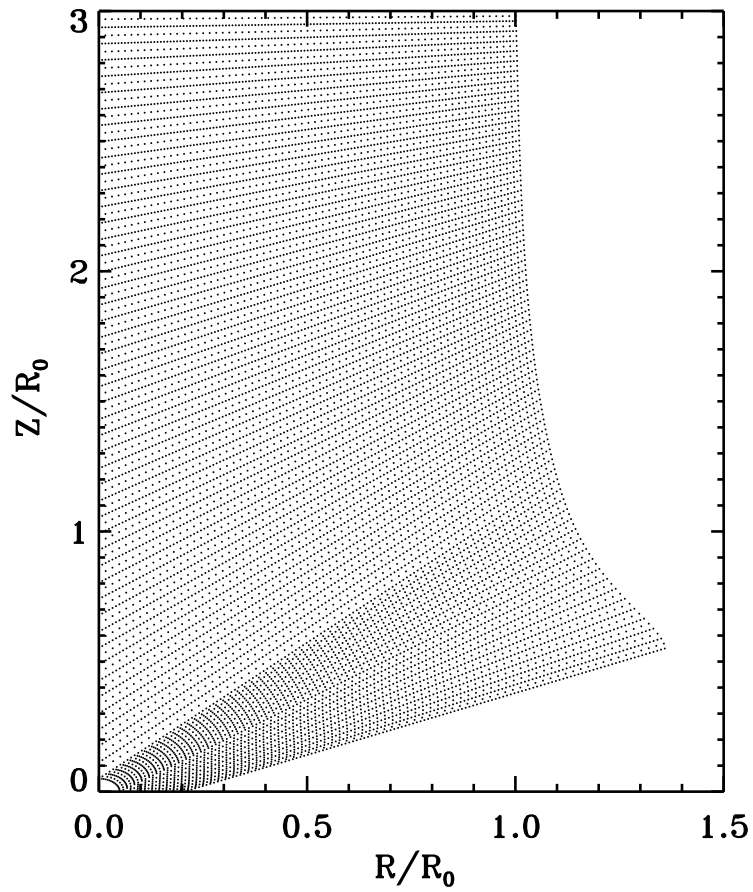


Figure A.1: Equidistant grid example of the inner solution of the GS equation (2.21) shown in Fig. 3.7.

Bibliography

- Allen C.W., 1973, *Astrophysical Quantities*, The Athlone Press, 3rd Ed., London
- André P., Phillips R.B., Lestrade J.F., Klein K.L., 1991, *Direct VLBI detection of the magnetosphere surrounding the young star S1 in Rho Ophiuchi*, ApJ **376**, 630
- Appl S., Camenzind M., 1993a, *Self-collimated jets beyond the light cylinder*, A&A **270**, 71
- Appl S., Camenzind M., 1993b, *The structure of relativistic MHD jets: a solution to the non-linear Grad-Shafranov equation*, A&A **274**, 699
- Begelman M.C., Blandford R.D., Rees M.J., 1984, *Theory of extragalactic radio sources*, Rev.Mod.Phys. **56**, 255
- Begelman M.C., Li Z.Y., 1994, *Asymptotic domination of cold relativistic MHD winds by kinetic energy flux*, ApJ **426**, 269
- Biretta J.A., Sparks W.B., Macchetto F., 1999, *Hubble Space Telescope observations of superluminal motion in the M87 jet*, ApJ **520**, 621
- Biretta J.A., 1999, *Observations of jets in galactic and extragalactic sources*, in *American Astronomical Society Meeting 195*, AAS **195**, 54.01
- Blandford R.D., Payne D.G., 1982, *Hydromagnetic flows from accretion discs and the production of radio jets*, MNRAS **199**, 883
- Blandford R.D., Netzer H., Woltjer L., 1990, *Active Galactic Nuclei*, Saas-Fee Advanced Course 20, Lecture Notes 1990, Swiss Society for Astrophysics and Astronomy, T.J.-L. Courvoisier & M. Major ed., Springer-Verlag
- Bloom S.D., Marscher A.P., 1996, *An analysis of the synchrotron self-Compton model for the multi-wave band spectra of blazars*, ApJ **461**, 657
- Brinkmann W., 1980, *Adiabatic accretion onto a Schwarzschild black hole*, A&A **85**, 146
- Brinkmann W., Kawai N., 2000, *The jets of SS 433: second order effects*, A&A **363**, 640
- Brinkmann W., 2001, MPE, *priv. comm.*
- Burbidge G.R., 1956, *On synchrotron radiation from Messier 87*, ApJ **124**, 416
- Camenzind M., 1986, *Hydromagnetic flows from rapidly rotating compact objects. I - Cold relativistic flows from rapid rotators*, A&A **162**, 32
- Camenzind M., 1987, *Hydromagnetic flows from rapidly rotating compact objects. II - The*

- relativistic axisymmetric jet equilibrium*, A&A **184**, 341
- Camenzind M., 1990, *Magnetized disk-winds and the origin of bipolar outflows*, RvMA **3**, 234
- Celotti A., Fabian A.C., 1993, *The kinetic power and luminosity of parsec-scale radio jets - an argument for heavy jets*, MNRAS **264**, 228
- Cesari F., 1994, *Introduzione al Metodo degli Elementi Finiti*, Pitagora Editrice Bologna
- Chiueh T., Li Z.Y., Begelman M.C., 1991, *Asymptotic structure of hydromagnetically driven relativistic winds*, ApJ **377**, 462
- Contopoulos J., 1994, *Magnetically driven relativistic jets and winds: exact solutions*, ApJ **432**, 508
- Contopoulos J., 1995, *Force-free self-similar magnetically driven relativistic jets*, ApJ **446**, 67
- Corbel S., Kaaret P., Jain R.K., Bailyn C.D., Fender R.P., Tomsick J.A., Kalemci E., McIntyre V., Campbell-Wilson D., Miller J.M., McCollough M.L., 2001, *X-Ray States and Radio Emission in the Black Hole Candidate XTE J1550–564*, ApJ **554**, 43
- Costa E., et al., 1997, *Discovery of an X-ray afterglow associated with the gamma-ray burst of 28 February 1997*, Nature **387**, 783
- Döbereiner S., Junkes N., Wagner S.J., Zinnecker H., Fosbury R., Fabbiano G., Schreier E. J., 1996, *ROSAT HRI Observations of Centaurus A*, ApJ **470**, L15
- Ebisawa K., Takeshima T., White N.E., Kotani T., Ueda Y., Dotani T., Robinson C.R., Harmon B.A., Zhang S.N., Tavani M., Foster R., 1998, *ASCA Observations of the Superluminal Jet Source GRS1915+105*, in *The Hot Universe*, IAU 188 General Assembly, Kyoto, Japan, August 1997, K. Koyama, S. Kitamoto, M. Itoh, Kluwer ed., **p.392**
<ftp://lheafpt.gsfc.nasa.gov/pub/ebisawa/kyoto.ps.gz>
- Fabian A.C., Rees M.J., 1979, *SS 433 - A double jet in action*, MNRAS **187**, 13
- Fender R.P., Garrington S.T., McKay D.J., Muxlow T.W.B., Pooley G.G., Spencer R.E., Stirling A.M., Waltman E.B., 1999, *MERLIN observations of relativistic ejections from GRS 1915+105*, MNRAS **304**, 865
- Fender R.P., Rayner D., Norris R., Sault R.J., Pooley G., 2000, *Discovery of circularly polarized radio emission from SS 433*, ApJ **530**, L29
- Fendt C., Camenzind M., Appl S., 1995, *On the collimation of stellar magnetospheres to jets. I. Relativistic force-free 2D equilibrium*, A&A **300**, 791
- Fendt C., Camenzind M., 1996, *On collimated stellar jet magnetospheres. II. Dynamical structure of collimating wind flows*, A&A **313**, 591
- Fendt C., 1997a, *Collimated jet magnetospheres around rotating black holes. General relativistic force-free 2D equilibrium*, A&A **319**, 1025
- Fendt C., 1997b, *Differentially rotating relativistic magnetic jets. Asymptotic trans-field force-balance including differential rotation*, A&A **323**, 999
- Fendt C., Memola E., 2001a, *Collimating, relativistic, magnetic jets from rotating disks. The*

- axisymmetric field structure of relativistic jets and the example of the M 87 jet*, A&A **365**, 631
- Fendt C., Memola E., 2001b, *Stationary relativistic magnetic jets from rotating black holes*, in *Microquasars*, Third Microquasar Workshop, Granada, Spain, September 2000, A.J. Castro-Tirado, J. Greiner, J.M. Paredes, Kluwer ed., Ap&SS **276**, 297
- Fendt C., Greiner J., 2001, *Magnetically driven superluminal motion from rotating black holes. Solution of the magnetic wind equation in Kerr metric*, A&A **369**, 308
- Ferrari A., Massaglia S., Bodo G., Rossi P., 1996, *Phenomenology and modelling of large-scale jets*, in *Solar and Astrophysical Magnetohydrodynamic Flows*, Heraklion, Crete, Greece, June 1995, K.C. Tsinganos ed., NATO ASI Series **C 481**, 607
- Ferraro V.C.A., 1937, *The non-uniform rotation of the sun and its magnetic field*, MNRAS **97**, 458
- Ferreira J., 1997, *Magnetically-driven jets from Keplerian accretion discs*, A&A **319**, 340
- Ford H.C., Harms R.J., Tsvetanov Z.I., Hartig G.F., Dressel L.L., Kriss G.A., Bohlin R.C., Davidsen A.F., Margon B., Kochhar A.K., 1994, *Narrowband HST images of M87: Evidence for a disk of ionized gas around a massive black hole*, ApJ **435**, L27
- Ghisellini G., Madau P., 1996, *On the origin of the gamma-ray emission in blazars*, MNRAS **280**, 67
- Greiner J., Morgan E.H., Remillard R.A., 1996, *Rossi X-ray Timing Explorer observations of GRS 1915+105*, ApJ **473**, L107
- Greiner J., 2000, *Microquasars*, in *Cosmic Explosions*, 10th Astrophysics Conference, College Park, Maryland, October 1999, S.S. Holt & W.W. Zhang ed., AIP **522**, 325
- Greiner J., Cuby J.G., McCaughrean M.J., 2001, *An unusually massive stellar black hole in the Galaxy*, Nature **414**, 522
- Jensen B.L., et al., 2001, *The afterglow of the short/intermediate-duration gamma-ray burst GRB 000301C: A jet at $z=2.04$* , A&A **370**, 909
- Junor W., Biretta J.A., Livio M., 1999, *Formation of the radio jet in M87 at 100 Schwarzschild radii from the central black hole*, Nature **401**, 891
- Khanna R., Camenzind M., 1992, *Magnetized thin accretion disks in active galactic nuclei - A quantitative analysis of field topologies and their dynamic importance*, A&A **263**, 401
- Kotani T., Kawai N., Matsuoka M., Brinkmann W., 1996, *Iron-line diagnostics of the jets of SS 433*, PASJ **48**, 619
- Kotani T., Kawai N., Nagase F., Namiki M., Sakano M., Takeshima T., Ueda Y., Yamaoka K., Hjellming R.M., 2000, *ASCA Observations of the jet source XTE J1748-288*, ApJ **543**, L133
- Li Z.Y., Chiueh T., Begelman M.C., 1992, *Electromagnetically driven relativistic jets - A class of self-similar solutions*, ApJ **394**, 459

- Li Z.Y., 1993, *Electromagnetically driven relativistic jets - A class of self-consistent numerical solutions*, ApJ **415**, 118
- Lovelace R.V.E., Berk H.L., Contopoulos J., 1991, *Magnetically driven jets and winds*, ApJ **379**, 696
- Mannheim K., Biermann P.L., 1989, *Photomeson production in active galactic nuclei*, A&A **221**, 211
- Margon B., Stone R.P.S., Klemola A., Ford H.C., Katz J.I., Kwitter K.B., Ulrich R.K., 1979, *The bizarre spectrum of SS 433*, ApJ **230**, L41
- Margon B., 1984, *Observations of SS 433*, ARA&A **22**, 507
- Markoff S., Falcke H., Fender R., 2001, *A jet model for the broadband spectrum of XTE J1118+480. Synchrotron emission from radio to X-rays in the Low/Hard spectral state*, A&A **372**, L25
- Memola E., Fendt C., 2001, *Two-dimensional magnetic field structure of relativistic jets in Active Galactic Nuclei*, in *AGN in 2000*, 4th National Meeting on Active Galactic Nuclei, Trieste, Italy, May 2000, A. Celotti ed., MmSAI **72**, 97
- Memola E., Fendt C., Brinkmann W., 2002, *Theoretical thermal X-ray spectra of relativistic MHD jets*, A&A **385**, 1089
- Mészáros P., 2001, *Gamma-Ray Bursts: accumulating afterglow implications, progenitor clues, and prospects*, Science **291**, 79
- Mewe R., Gronenschild E.H.B.M., van der Oord G.H.J., 1985, *Calculated X-radiation from optically thin plasmas. V.*, A&AS **62**, 197
- Michel F.C., 1969, *Relativistic stellar-wind torques*, ApJ **158**, 727
- Milgrom M., 1979, *SS 433 - The acceleration and collimation mechanisms*, A&A **78**, L9
- Miller J.M., Fox D.W., Di Matteo T., Wijnands R., Belloni T., Pooley D., Kouveliotou C., Lewin W.H.G., 2001, *Relativistic iron emission and disk reflection in galactic microquasar XTE J1748–288*, ApJ **546**, 1055
- Mirabel I.F., Rodríguez L.F., 1994, *A superluminal source in the Galaxy*, Nature **371**, 46
- Mirabel I.F., Rodríguez L.F., 1995, *Superluminal motions in our Galaxy*, in *17th Texas Symposium on Relativistic Astrophysics and Cosmology*, H. Böhringer, G.E. Morfill & J.E. Trümper ed., New York, Annals of the New York Academy of Science **759**, 21
- Mirabel I.F., Rodríguez L.F., 1998, *Microquasars in our Galaxy*, Nature **392**, 673
- Mirabel I.F., Rodríguez L.F., 1999, *Sources of relativistic jets in the Galaxy*, ARA&A **37**, 409
- Mundt R., Buehrke T., Solf J., Ray T.P., Raga A.C., 1990, *Optical jets and outflows in the HL Tauri region*, A&A **232**, 37
- Nitta S.-Y., 1994, *Asymptotically conical solution of magnetically driven relativistic winds*, PASJ **46**, 217
- Nitta S.-Y., 1995, *Current distribution in rotating magnetized winds across the light cylinder*,

- MNRAS **276**, 825
- Okamoto I., 1992, *The evolution of a black hole's force-free magnetosphere*, MNRAS **254**, 192
- Orosz J.A., Kuulkers E., van der Klis M., McClintock J.E., Garcia M.R., Callanan P.J., Bailyn C.D., Jain R.K., Remillard R.A., 2001, *A black hole in the superluminal source SAX J1819.3–2525 (V4641 SGR)*, ApJ **555**, 489
- Ouyed R., Pudritz R.E., 1997, *Numerical simulations of astrophysical jets from Keplerian disks. I. Stationary Models*, ApJ **482**, 712
- Owen F.N., Eilek J.A., Kassim N.E., 2000, *M87 at 90 centimeters: a different picture*, ApJ **543**, 611
- Pudritz R.E., Norman C.A., 1983, *Centrifugally driven winds from contracting molecular disks*, ApJ **274**, 677
- Ray T. P., Mundt R., Dyson J.E., Falle S.A.E.G., Raga A.C., 1996, *HST observations of jets from young stars*, ApJ **468**, L103
- Ray T.P., Muxlow T.W.B., Axon D.J., Brown A., Corcoran D., Dyson J., Mundt R., 1997, *Large-scale magnetic fields in the outflow from the young stellar object T Tauri S*, Nature **385**, 415
- Rees M.J., Mészáros P., 1992, *Relativistic fireballs - Energy conversion and time-scales*, MNRAS **258**, 41
- Rees M.J., Mészáros P., 1994, *Unsteady outflow models for cosmological gamma-ray bursts*, ApJ **430**, L93
- Reynolds C.S., Fabian A.C., Celotti A., Rees M.J., 1996, *The matter content of the jet in M87: evidence for an electron-positron jet*, MNRAS **283**, 873
- Rüdiger G., Elstner D., Stepinski T.F., 1995, *The standard-accretion disk dynamo*, A&A **298**, 934
- Rybicki G.B., Lightman A.P., 1979, *Radiative Processes in Astrophysics*, John Wiley & Sons, Inc., USA
- Sakurai T., 1985 *Magnetic stellar winds - A 2-D generalization of the Weber-Davis model*, A&A **152**, 121
- Sari R., Piran T., Halpern J., 1999, *Jets in Gamma-Ray Bursts*, ApJ **519**, L17
- Schwarz H.R., 1984, *Methode der finiten Elemente*, Teubner Studienbücher, Stuttgart
- Shemi A., Piran T., 1990, *The appearance of cosmic fireballs*, ApJ **365**, L55
- Sikora M., Madejski G., Moderski R., Poutanen J., 1997, *Learning about active galactic nucleus jets from spectral properties of blazars*, ApJ **484**, 108
- Synge J., 1957, *The Relativistic Gas*, North Holland, Amsterdam
- Spruit H.C., 1999, *Gamma-ray bursts from X-ray binaries*, A&A **341**, L1
- Takahashi M., Nitta S., Tatematsu Y., Tomimatsu A., 1990, *Magnetohydrodynamic flows in*

Kerr geometry - Energy extraction from black holes, ApJ **363**, 206

Urry C.M., Padovani P., 1995, *Unified schemes for radio-loud Active Galactic Nuclei*, PASP **107**, 803

Zdziarski A.A., Grove J.E., Poutanen J., Rao A.R., Vadawale S.V., 2001, *OSSE and RXTE observations of GRS 1915+105: evidence for non-thermal Comptonization*, ApJ **554**, L45

Zensus J.A., Cohen M.H., Unwin S.C., 1995, *The parsec-scale jet in quasar 3C 345*, ApJ **443**, 35

Zinnecker H., McCaughrean M.J., Rayner J.T., 1998, *A symmetrically pulsed jet of gas from an invisible protostar in Orion*, Nature **394**, 862

Acknowledgments

My PhD time in Potsdam: an unforgettable experience!

AIP was my second home, therefore I would like to thank some people that made it a comfortable place for me.

Choosing me for the PhD position on MHD jets, Prof. Günther Ruediger and Dr. Christian Fendt gave me a great chance to learn a lot of new and interesting things and I will always be grateful for that.

Prof. Rüdiger, with his assured leadership, strongly supported the jet-project and, at the same time, allowed me to work on the topic with absolute freedom.

Christian had always time for me. There was never a question he left unanswered, day by day patient, nice and friendly during our long and useful discussions. Chris has been for me also a good friend I could share my difficulties with. In one word, I think he is a wonderful person.

Prof. Günther Hasinger showed interest in the jet problematic and also supported me.

Dr. Jochen Greiner, since my first days at AIP, offered me the possibility of stimulating discussions about High Energy Astrophysics. With his smart student, Arne Rau, I had also useful talks about microquasars.

Dr. Wolfgang Brinkmann (MPE) has been kind and helpful for the successful development of the second part of the PhD work.

Prof. Giorgio Palumbo has followed from Italy the progress of my PhD at AIP, giving me the energy that for years has been nourishing my passion for Astrophysics. From him I learned not only about science, but also about life.

Prof. Rüdiger, Dr. Greiner and Prof. Palumbo, I also thank you for accepting to referee the thesis.

Mr. Manfred Schultz and Dr. Karl-Heinz Böning, our magicians of computers, found brilliant solutions in every panic situation.

Mrs. Andrea Trettin, our wonderful secretary, always caring for the necessities of the group, was very kind to me as well as all the people of the administration.

All members of the Magnetohydrodynamics group and of the whole Institute are ready to help each other for every sort of problem. I was always welcome!

Many colleagues were populating the rooms N.21 and N.11 in the B6 (Direktorenhaus), they

became friends for me. In our international PhD big room there was always a nice atmosphere of solidarity. With the Italian and international community of the AIP, the Uni-Potsdam and the GFZ I had a good time.

A big *Thank You* to my Friends who all around the world remained close to me, to my Family and to the Cremers, for 3 years in their happy house I felt at home.

Abstract

Jets are highly collimated flows of matter. They are present in a large variety of astrophysical sources: young stars, stellar mass black holes (microquasars), galaxies with an active nucleus (AGN) and *presumably* also intense flashes of gamma-rays. In particular, the jets of microquasars, powered by accretion disks, are probably small-scale versions of the outflows from AGN.

Beside observations of astrophysical jet sources, also theoretical considerations have shown that *magnetic fields* play an important role in jet formation, acceleration and collimation. Collimated jets seem to be systematically associated with the presence of an *accretion disk* around a star or a collapsed object. If the central object is a black hole, the surrounding accretion disk is the only possible location for a magnetic field *generation*.

We are interested in the formation process of highly relativistic jets as observed from microquasars and AGN. We theoretically investigate the jet collimation region, whose physical dimensions are extremely tiny even compared to radio telescopes spatial resolution. Thus, for most of the jet sources, *global* theoretical models are, at the moment, the only possibility to gain information about the physical processes in the innermost jet region.

For the first time, we determine the global two-dimensional field structure of stationary, axisymmetric, relativistic, strongly magnetized (force-free) jets collimating into an asymptotically cylindrical jet (taken as boundary condition) and anchored into a *differentially rotating* accretion disk. This approach allows for a direct connection between the accretion disk and the asymptotic collimated jet. Therefore, assuming that the foot points of the field lines are rotating with Keplerian speed, we are able to achieve a direct scaling of the jet magnetosphere in terms of the size of the central object. We find a close compatibility between the results of our model and radio observations of the M87 galaxy innermost jet.

We also calculate the X-ray emission in the energy range 0.2–10.1 keV from a microquasar relativistic jet close to its source of 5 solar masses. In order to do it, we apply the jet flow parameters (densities, velocities, temperatures of *each* volume element along the collimating jet) derived in the literature from the relativistic magnetohydrodynamic equations. We obtain theoretical thermal X-ray spectra of the innermost jet as composition of the spectral contributions of the single volume elements along the jet. Since relativistic effects as Doppler shift and Doppler boosting due to the motion of jets toward us might be important, we investigate how the spectra are affected by them considering different inclinations of the line of sight to the jet axis.

Emission lines of highly ionized iron are clearly visible in our spectra, probably also observed in the Galactic microquasars GRS 1915+105 and XTE J1748–288. The Doppler shift of the emission lines is always evident. Due to the chosen geometry of the magnetohydrodynamic jet, the inner X-ray emitting part is not yet collimated. Ergo, depending on the viewing angle, the Doppler boosting does not play a major role in the total spectra. This is the first time that X-ray spectra have been calculated from the numerical solution of a magnetohydrodynamic jet.

Abstract

Astrophysikalische Jets sind stark kollimierte Materieströmungen hoher Geschwindigkeit. Sie stehen im Zusammenhang mit einer Fülle verschiedener astrophysikalischer Objekte wie jungen Sternen, stellaren schwarzen Löchern ("Mikro-Quasare"), Galaxien mit aktivem Kern (AGN) und *wahrscheinlich* auch mit dem beobachteten intensiven Aufblitzen von Gamma-Strahlung (Gamma Ray Bursts). Insbesondere hat sich gezeigt, dass die Jets der "Mikro-Quasare" wahrscheinlich als kleinskalige Version der Jets der AGN anzusehen sind.

Neben den Beobachtungen haben vor allem auch theoretische Überlegungen gezeigt, dass *Magnetfelder* bei der Jetentstehung, -beschleunigung und -kollimation eine wichtige Rolle spielen. Weiterhin scheinen Jets systematisch verknüpft zu sein mit dem Vorhandensein einer *Akkretionsscheibe* um das zentrale Objekt. Insbesondere wenn ein schwarzes Loch den Zentralkörper darstellt, ist die umgebende Akkretionsscheibe der einzig mögliche Ort um Magnetfeld *erzeugen* zu können.

Wir sind speziell interessiert am Entstehungsprozess hoch relativistischer Jets wie sie bei Mikro-Quasaren und AGN beobachtet werden. Insbesondere untersuchen wir die Region, in der der Jet kollimiert, eine Region, deren räumliche Ausdehnung extrem klein ist selbst im Vergleich zur Auflösung der Radioteleskope. Dies ist ein Grund, wieso zum heutigen Zeitpunkt für die meisten Quellen die theoretische Modellierung die einzige Möglichkeit darstellt, um Information über die physikalischen Prozesse in der innersten Region der Jetentstehung zu erhalten.

Uns ist es zum ersten Mal gelungen, die *globale* zwei-dimensionale Magnetfeldstruktur stationärer, axialsymmetrischer, relativistischer und stark magnetisierter (kräfte-freier) Jets zu berechnen, die zum einen asymptotisch in einen zylindrischen Jet kollimieren, zum anderen aber in einer *differential rotierenden* Akkretionsscheibe verankert sind. Damit erlaubt dieser Ansatz eine physikalische Verknüpfung zwischen Akkretionsscheibe und dem asymptotischen Jet. Nimmt man also an, dass die Fußpunkte der Magnetfeldlinien mit Keplergeschwindigkeit rotieren, so kann man eine direkte Skalierung der Jetmagnetosphäre mit der Größe des Zentralobjektes erhalten. Unsere Resultate zeigen eine gute Übereinstimmung zwischen unserem Modell und Beobachtungen des Jets von M87.

Für das Beispiel eines relativistischen Mikroquasarjets haben wir die Röntgenemission im Bereich von 0.2–10.1 keV berechnet. Dafür haben wir in der Literatur aus den relativistischen magnetohydrodynamischen Gleichungen berechnete Jetgrößen (Dichte-, Geschwindigkeits-, und Temperaturprofil) verwendet und das Spektrum für *jeden* Punkt entlang der Jetströmung abgeleitet. Das theoretische thermische Röntgenspektrum des innersten, heißen Teils des Jets erhalten wir zusammengesetzt aus den spektralen Anteilen der einzelnen Volumenelemente entlang des Jets. Um relativistische Effekte wie Dopplerverschiebung und -verstärkung ("boosting") aufgrund der Jetbewegung zu untersuchen, haben wir für verschiedene Inklinationswinkel des Jets zur Sichtlinie berechnet, wie die erhaltenen Spektren davon beeinflusst werden.

Unsere Spektren zeigen deutlich die hochionisierten Eisen-Emissionslinien, die in den galaktischen Mikroquasaren GRS 1915+105 und XTE J1748–288 andeutungsweise beobachtet wurden. Eine Dopplerverschiebung dieser Linien ist in unseren Spektren deutlich zu sehen. Da die innerste, Röntgenstrahlung emittierende Region des magnetohydrodynamischen Jets allerdings noch unkollimiert ist, spielt Dopplerboosting in unseren Spektren, abhängig vom Sichtwinkel, keine große Rolle. Mit unseren Resultaten konnte zum ersten Mal ein Röntgenspektrum gewonnen werden, das auf der numerischen Lösung eines magnetohydrodynamischen Jets beruht.

Lebenslauf

Name und Familienname: **Elisabetta Memola**

Staatsangehörigkeit: Italienisch

Geburtsdatum und /-ort : 18. November 1971, Bari, Italien

Schulausbildung: 1985-1987 Naturwissenschaftliches Gymnasium in Bari
(Liceo G. Salvemini - Bari)

1987-1990 Naturwissenschaftliches Gymnasium in Bari
(Liceo E. Fermi - Bari)

6. July 1990, Abitur (Diploma di scuola media superiore)

Universität: 1990-1997 Studium der Astronomie, Universität Bologna

19. Dezember 1997, Diplom in Astronomie
(Laurea in Astronomia)

Promotionsstudium: 1998-2001 Wissenschaftliche Mitarbeiterin
am Astrophysikalischen Institut Potsdam,
Arbeitsgruppe Magnetohydrodynamik

20. Juni 2002, Tag der mündlichen Prüfung

Wissenschaftliche Tätigkeit: 2001-2002 Wissenschaftliche Mitarbeiterin
am Agenzia Spaziale Italiana Science Data Center, Rom,
Mission AGILE (Astrorivelatore Gamma ad Immagini LEggero)